공학박사 학위논문

Ionic Resistance Estimation and Electrochemical Analysis of Cathode Catalyst Layer for Polymer Electrolyte Membrane Fuel Cell

고분자 전해질막 연료전지 공기극 촉매층의

이온저항 측정 및 전기화학 분석

2012 년 8 월

서울대학교 대학원

화학생물공학부

임 주 완

Abstract

Ionic Resistance Estimation and Electrochemical Analysis of Cathode Catalyst Layer for Polymer Electrolyte Membrane Fuel Cell

Ju Wan Lim

School of Chemical and Biological Engineering

The Graduate School

Seoul National University

In this paper, electrochemical analysis of membrane-electrode assemblies (MEAs) was conducted in a single cell structure for polymer electrolyte membrane fuel cell (PEMFC). Transmission-line model (TLM) that is used for analyzing electrochemical impedance spectroscopy (EIS) results was modified and adopted to estimate electrochemical properties of cathode catalyst layer (CL) and polymer electrolyte membrane (PEM) in MEA. EIS for cathode CL was measured in non-faradaic condition, and the results were fitted by modified TLM. Finally ionic resistance of cathode CL ($R_{i,CCL}$), double layer capacitance (C_{dl}), and ionic resistance of PEM (R_{PEM}) could be estimated from the fitting results. Using this modified TLM, three different studies were carried out. (1) The relationship between electrochemical properties and

changing thickness, Pt loadings, and Pt/C ratio of cathode CL was analyzed, (2) variation of electrochemical properties before and after activation process was also measured and analyzed for MEAs those were made by catalyst-coated membrane (CCM) method, and (3) variation of electrochemical properties with changing interface states and conducting activation was analyzed for MEAs those were made by CCS method. (1) In thickness study, the catalyst with low Pt/C ratio and with high electrochemical surface area (ECSA) was advantageous for high performance when $\leq$ 0.2 mg$_{Pt}$ cm^{-2} of carbon-supported Pt catalyst was used as cathode catalyst. However thin cathode CL using high Pt/C ratio catalyst was advantageous for high performance when Pt loading in cathode CL was $\geq$ 0.3 mg$_{Pt}$ cm^{-2}. It would be due to the increased ionic resistance of CL and mass transfer resistance those were caused by thickness increase. Moreover effective thickness of cathode CL was estimated by comparing the fitting results of non-faradaic EIS with faradaic EIS measurements. (2) In activation study, I changed the perfluorosulfonic acid ionomer (PFSI) content in cathode CL, and the relationship between PFSI content and changes of electrochemical properties after activation was analyzed. Before activation, the interaction between Pt(111) and sulfonate anion of PFSI in cathode CL was strong for the MEAs those were made by CCM method. However the interaction was weakened after activation and it would cause activity improvement of oxygen reduction reaction (ORR). R_{PEM} and $R_{i,CCL}$ were decreased after activation because water content in MEA was increased. Therefore hydration of CL and PEM affect to enhancement of MEA performance after activation. (3) In interface study, MEAs with different interface between CL and PEM were

ii

prepared by using CCS method. Hot-pressed MEAs before activation showed weak interaction between Pt(111) and sulfonate anion of PFSI, and the activation ratios of hot-pressed MEAs were also lower than those of non hot-pressed MEAs. Hot-pressing would improve the interface stability between PEM and CL. And increase of PFSI film thickness on CL would extend the interface area. The improved interface stability after hot-pressing caused low R_{PEM}, and the increased interface area caused low $R_{i,CCL}$.

Keywords: Polymer electrolyte membrane fuel cell (PEMFC), membrane-electrode assembly (MEA), electrochemical impedance spectroscopy (EIS), cathode catalyst layer, perfluorosulfonic acid ionomer (PFSI)

Student Number: 2008-30895

Contents

List of Tables

List of Figures

Chapter 1. Introduction

1.1 Fuel Cells

For modern human races, electrical energy is the most useful energy for a living. Therefore many researchers have studied about efficient energy conversion method from obtainable energies such as solar, chemical, kinetic, and heat energy to electrical energy. Nowadays, the most widely used method to obtain electrical energy is combination of internal combustion and electricity generation. This method requires chemical energy sources such as coal, petroleum, natural gases. Therefore the consumption level of these underground resources is exponentially increasing, and the exhaustion of natural resources and environmental pollution by the generated byproducts during energy conversion have been a big problem. Low energy conversion efficiency of conventional method intensifies the exhaustion of natural resources and environmental pollution.

Fuel cell is an energy conversion device that can convert directly chemical energy of fuels to electrical energy without any mechanical moving part during conversion. The useable chemical fuel is various such as hydrogen, hydrocarbon, and carbon. It means that efficiency of energy conversion from chemical to electrical energy is very high. Therefore development of high performance fuel cell is helpful for saving natural resources and reducing environmental pollution.

1.1.1 Principle of Fuel Cell

A fuel cell is an electrochemical energy converter that converts chemical energy of fuel directly into DC electricity.[1] Hydrogen gas is the most common fuel for fuel cell although hydrocarbons such as methanol and natural gas are usable. In the case of hydrogen fuel cell, the reactions those occur in fuel cell are as the followings:

Anode:	$2H_2$	$\rightarrow \quad 4H^+ + 4e^-$	$E^0 = 0.000$ V
Cathode:	$O_2 + 4H^+ + 4e^-$	$\rightarrow \quad 2H_2O$	$E^0 = 1.229$ V
Overall:	$O_2 + 2H_2$	$\rightarrow \quad 2H_2O$	$E_{cell} = 1.229$ V
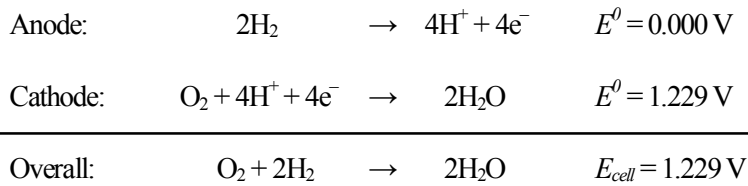
E^0 is standard electrode potential vs. normal hydrogen electrode (NHE). E^0 can be obtained thermodynamically from difference of Gibbs free energy. Therefore theoretical cell voltage of hydrogen fuel cell is 1.229 V. However in actual hydrogen fuel cell, sluggish cathode reaction kinetics and fuel crossover from anode to cathode cause low open circuit voltage about 1.0 V. Because some kinds of overpotentials such as activation, ohmic, and concentration overpotential are required for high power generation, normal cell voltage during operation is half of the thermodynamic cell voltage. Moreover cell voltage is decreased when current is increased to generate high power, and energy conversion efficiency is also decreased. Nevertheless, silent characteristics due to lack of moving parts and low emission of harmful byproducts for human and environment make fuel cell an attractive device.

However fuel cells have serious disadvantages such as high cost, low durability, and

low infrastructure for leading hydrogen economy. Fuel availability and storage are also problems. Although fuel cells work best when hydrogen is used as a fuel a fuel, alternative liquid fuels such as methanol, formic acid, and gasoline are tried to use directly or with reformer because hydrogen has a low volumetric energy density and a storage difficulty.[2]

1.1.2 History of Fuel Cell

In 1802, Humphry Davy demonstrated the concept of a fuel cell with the structure of $C/H_2O/HNO_3/O_2/C$.[3] Christian Friedrich Schonbein discovered the principle of the fuel cell in 1838 and published.[4] A Welsh judge and physical scientist, Sir William Robert Grove, conducted a series of experiments that electric current could be produced by the electrochemical reaction of hydrogen and oxygen on a Pt electrode, and named this cell as "gas voltaic battery" in1839.[5] Fig. 1.1 (a) shows the illustration of gas battery presented by Grove. The term fuel cell was first used by Ludwig Mond and Charles Langer in 1889. Francis Bacon developed the first successful application of alkaline fuel cell (AFC) in 1932, and demonstrated it in 1959 with 5 kW-fuel cell system for powering welding machinery. Willard Thomas Grubb and Leonard Niedrach at General Electric invented the first polymer electrolyte membrane fuel cell (PEMFC), and the cooperated with NASA. This PEMFC was used as a power source of the Gemini space program in 1960s, and Gemini VII is shown in Fig. 1.1 (b).[6] In the

Apollo space program, AFCs were used as an electric power source when the astronauts landed on the moon. Nowadays, comprehensive efforts are conducting to enable the widespread commercialization of fuel cells in diverse sectors.[7] Fuel cell car designed by GM is shown in Fig. 1.1 (c).[8]

1.1.3 Types of Fuel Cells

There are many kinds of fuel cells, and generally their names are related electrolyte or fuel of them. Popular fuel cell types are listed in Table 1. Working temperatures are determined by the electrolyte temperature for carrying the ion effectively. Applications of the fuel cells are related to the working temperature and fuel types. Low temperature fuel cells such as PEMFC, DMFC (direct methanol fuel cell), and PAFC (phosphoric acid fuel cell) are usable for portable or vehicular applications, and high temperature fuel cells such as SOFC (solid oxide fuel cell) and MCFC (molten carbonate fuel cell) are usable for distributed generation.
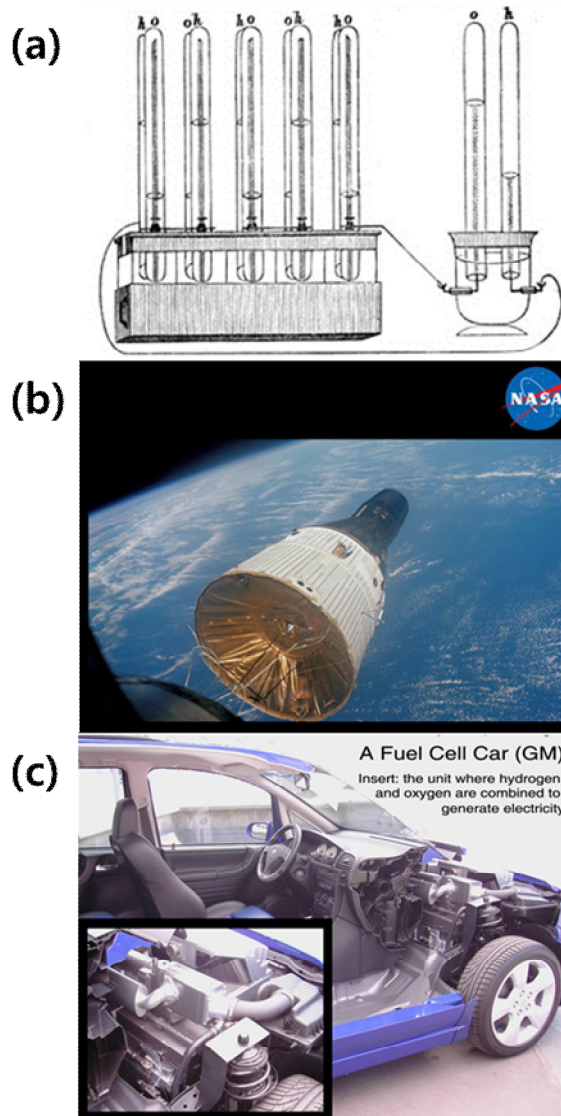
Figure 1.1. Images of (a) gas voltaic battery presented by Grove, (b) Gemini VII capsule, and (c) GM's fuel cell car.[5,6,8]

Table 1. Fuel cell types and features

Type	Electrolyte	Conductive ion	Working temperature (°C)	Applications
PEMFC	Polymer	H^+	50 − 200	Transportation Portable power Distributed generation
DMFC	Polymer	H^+	50 − 120	Portable power
PAFC	Phosphoric acid	H^+	150 − 250	Distributed generation
AFC	Alkaline solution	OH^-	150 − 200	Military Space
SOFC	Ceramic oxide	O^{2-}	500 − 1100	Auxiliary power Distributed generation
MCFC	Molten carbonate	CO_3^{2-}	600 − 650	Distributed generation

1.1.4 Polymer Electrolyte Membrane Fuel Cells (PEMFCs)

There are two expressions of PEMFC such as polymer electrolyte membrane fuel cell or proton exchange membrane fuel cell, and some other people say PEFC (polymer electrolyte fuel cell). Because the electrolyte of DMFC is also polymer, some people categorize DMFC as a kind of PEMFC using methanol fuel. However in general PEMFC is regarded hydrogen fuel cell. Illustration of general PEMFC structure and operation is shown in Fig. 1.2. PEMFCs use a quasi-solid electrolyte which is based on a polymer backbone with side-chains possessing acid-based groups.[9] Recently the PEMFC is vigorously research by automobile companies such as GM, Toyota, Nissan, and Hyundai-Kia motor company because PEMFC is the alternative power source of engine for vehicle.[10-13] PEMFC has many advantages for use in vehicles. They operate at relatively low temperature, and have short start-up and transient-response times compared to other types of fuel cells.[14] Moreover national research institutes such as Los Alamos, Argon, and Lawrence Berkeley National Laboratory, and chemical companies developing polymer membrane such as Gore and 3M are also trying to improve the PEMFC technology.[15-21] US Department of energy (DOE) that is a government organization invests to the PEMFC research groups by the hydrogen and fuel cells program.[7]

PEMFC
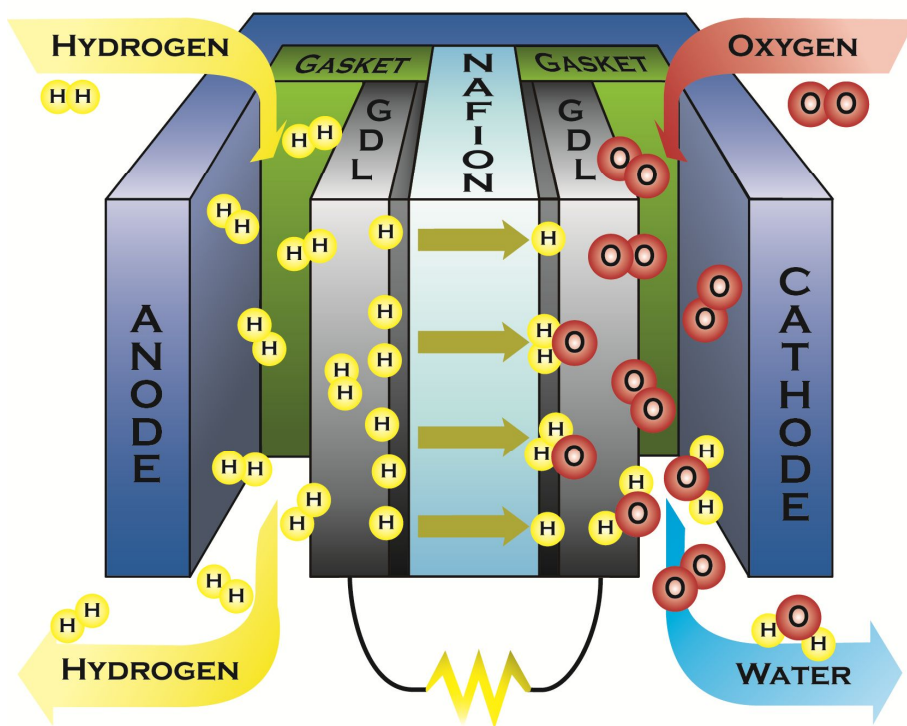
Figure 1.2. Illustration of PEMFC operation.

1.1.5 Components of PEMFC

The components and structure of PEMFC single cell is shown in Fig. 1.3. Solid state polymer electrolyte membrane (PEM) is located in the center of the cell. Each of the anode and cathode catalyst layer (CL) are deposited to the both sides of the PEM, and this three-layer component is called as catalyst-coated membrane (CCM). Two gas diffusion layers (GDLs) are located outside of anode and cathode CLs. This five-layer component is called as membrane-electrode assembly (MEA). MEA is the core component where the electrochemical reactions and energy conversion are occurred. MEA is sandwiched between two bipolar plates that has gas flow channel on the surface, and the arrangement of MEAs and bipolar plates are repeated. These are sandwiched between two end plates that tight the stack and make tightening forces uniform.

MEA preparation method means CL deposition method. There are diverse deposition methods of CL such as spraying, painting (brushing), doctor blade (bar coating), electrospraying, screen printing, inkjet printing.[22-31] These methods are possible if the catalyst is synthesized and dispersed in solvent. By those methods, CL can be deposited on PEM or GDL because CL is located between PEM and GDL. Therefore MEA preparation method can be classified as CCM and catalyst-coated substrate (CCS) method.[32-36] Among MEA preparation methods, decal transfer method is a special method because the CL is not deposited on PEM or GDL but deposited on

other substrate such as Teflon blank, Kapton film, and filter paper.[37-39] Decal transfer method is classified as CCM method because CL on substrate is transferred to PEM by hot-pressing.
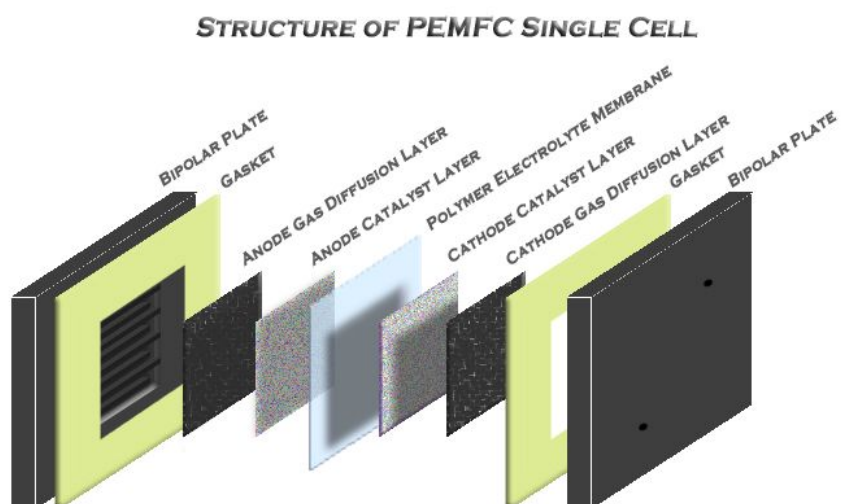
Figure 1.3. The components and structure of PEMFC single cell.

1.2 Electrochemical Analysis for PEMFC Analysis

Because PEMFC is an electrochemical device, electrochemical analysis is useful to characterize the CL and electrolyte. However it is hard to analyze the CL because the electrolyte of PEMFC is solid state, and three-electrode test and changing the salt of electrolyte is almost impossible. Therefore analyzing methods are limited to analyze one side of CL and PEM. For example, anode CL is connected with counter and reference electrode and regarded as a normal hydrogen electrode (NHE) by supplying humidified hydrogen gas, and cathode CL is connected to working electrode to analyze by supplying humidified nitrogen gas. The electrochemical analyzing methods for PEMFCs are such as IV polarization test, electrochemical impedance spectroscopy (EIS), cyclic voltammetry (CV), linear sweep voltammetry (LSV), chronopotentiometry, and chronoamperometry. In this thesis, polarization test, EIS in faradaic condition, EIS in non-faradaic condition, and CV is used for analyze cathode CL and PEM.

1.2.1 Polarization Test

Polarization test is general performance test of fuel cell. It can be conducted by current sweep or galvanostatic method. Because current sweep method is not steady-state measurement, EIS is necessary to compensate for steady-state result. During polarization test, hydrogen gas is supplied to anode, and O_2 or air gas is supplied to

cathode. The variables that affect to the cell performance are flow rates, partial pressures, humidity of reactant gases, and cell temperature. Flow rate of reactant is expressed as stoichiometry that is a reciprocal number of fuel utilization efficiency.[2] Partial pressure of reactant gases can be controlled by changing concentration of supplement gas or changing outlet pressure of the cell to increase the reactant gas pressure. Humidity of reactant gases can be changed by controlling the temperature of humidifier. High partial pressure and humidity of reactant gases increase the cell performance, and there are optimum values of flow rate and cell temperature to realize maximum performance.

1.2.2 Cyclic Voltammetry

As stated earlier, humidified hydrogen and nitrogen gases are supplied to anode and cathode, respectively, during CV measurement of cathode CL. Liquid water can substitute the humidified nitrogen gas. The supplied gases of each electrode can be changed to measure CV for anode CL. However if the catalyst of hydrogen electrode is not Pt, auxiliary electrode that is supplied hydrogen gas would not show the potential of NHE. CV is useful method to estimate the electrochemical surface area (ECSA) of Pt by using hydrogen adsorption or desorption charge. Cell temperature during CV measurement also affect to the ECSA, and hydrogen desorption charge is decreased with increase of cell temperature because high temperature causes high

kinetic energy of proton, and therefore hydrogen is not cover all of the platinum surfaces.[40] Therefore to estimate exact ECSA, CV should be measured under 50 °C.

1.2.3 Electrochemical Impedance Spectroscopy (EIS)

Applying DC plus AC voltage with a frequency to an electrochemical system can cause the DC plus AC current response with phase difference. The amplitude and phase difference of AC current can be changed with the variation of AC voltage frequency although the amplitude of AC voltage is fixed. It is due to the capacitor-like charge storing nature of the electrode-electrolyte interface in electrochemical system. The control factor, voltage, and response factor, current, can be showed at once as resistance term. Therefore the phase difference and amplitudes of AC voltage and current can be showed as complex resistance, impedance.

EIS is an effective technique to extract each component in an electric circuit.[41] Moreover EIS is *in-situ* measurement, and can be measured at faradaic condition with H_2/O_2 reactants and non-faradaic condition with H_2/N_2 feeds. However it takes relatively long time because EIS can be measured at stead-state, and the reliability of high current and low frequency data is low.

1.3 Subjects of this thesis

In this thesis, the main theme is electrochemical analysis of cathode CL, and methodologically, there are three different studies; (1) thickness study (changing cathode CL thickness by using various Pt/C ratio catalysts or changing catalyst loadings), (2) activation study (variation of electrochemical properties of cathode CL for PEMFC during activation process), and (3) interface study (the effect of interfacial resistance of CL and membrane prepared by CCS method).

1.3.1 Thickness study

MEA performance depends on many factors related with its components, ionic conductivity of the electrolyte, catalyst activity, gas and water permeability through the GDL and CL, interfacial resistance between the membrane and the CL, and the electronic and ionic resistance of the CL.[42-46] The ionic resistance of the CL is not a significant factor when the thickness of the CL is ≤ 0.3 μm.[20] However, the thickness of CL is several micrometers in most cases, so the ionic resistance has a decisive effect on performance. Therefore, estimating ionic resistance of the CL with diverse thicknesses is necessary to realize the effect of ionic resistance of the CL on MEA performance.

Ionic resistance of the CL is a property that is difficult to estimate independently in a fabricated system. Boyer et al. estimated the ionic resistance of the CL by EIS of an inactive CL that was inserted between two membranes.[47] While this eidetic system directly measures ionic conductivity of the CL, measuring ionic conductivity in a fabricated system is impossible. Lefebvre et al. reported a method for measuring the ionic resistance of the CL in a fabricated system using the EIS finite transmission-line model (TLM).[48] TLM has been suggested by de Levie as a useful element for estimating the resistance and capacitance of porous electrode.[49] Therefore TLM has been widely used by many research groups to analyze the CL.[48,50-54]

Estimating the ionic resistance of a CL with various thicknesses is necessary, so I indicate the resistance values through estimation. Some methods are available to change CL thickness: (1) change the catalyst loading, (2) change the Pt/C ratio, and (3) change CL porosity. In this study, the first and second methods were used to change CL thickness. Estimating the effect of CL thickness on ionic resistance without a structural change in the CL was the purpose in this study. Therefore I modified the TLM and used this model for estimating the ionic resistance of the CL by EIS under a non-faradaic condition. The faradaic condition means the operating condition with supplying humidified H_2 and air to the anode and cathode, respectively, and the non-faradaic condition means the condition supplying humidified H_2 and N_2 to the anode and cathode at room temperature, respectively. The modified TLM included cell

16

inductance, electrolyte resistance, and charge transfer resistance of crossovered H_2 for exact and easy fitting. The effect of increased ionic resistance with increased thickness of the cathode CL on MEA performance was evaluated. Since the thickness of the cathode CL also affects oxygen transportation, charge transfer resistance as well as ionic resistance should be evaluated with various CL thicknesses. These complicated correlations make analysis difficult. Therefore many research groups tried to evaluate the relationship between CL thickness and cell performance by numerical calculation and experimental method.[55,-57] These researches infer that existence of optimum or effective thickness of the cathode CL for maximum performance. Lee et al. changed the CL thickness by mixing the Pt/C catalyst with uncatalyzed carbon black, and showed that diluted Pt/C in the CL enhanced O_2 accessibility. It means that the density of active sites in the CL also can affect the mass transfer resistance. Therefore I changed the thickness of the cathode CL by changing the catalyst loading or changing the Pt/C ratio, and tried to estimate ionic resistance and mass transfer resistance in each case.

1.3.2 Activation study

For as-prepared MEA of PEMFC, activation process is necessary to show maximum performance.[58] The expression of activation is various such as activation, break-in, conditioning, incubation, and pretreatment.[59-61] Although most people insist

necessary of activation process, the clear reason of this phenomenon is not established yet. Many researchers showed that high temperature, high reactant partial pressure, and high humidity condition is preferable for activation. The activation mechanism is assumed that inactive sites before activation became active sites, dehydrated Nafion became hydrate, and electronic and ionic insulated region became conductive sites.[58] Therefore changes of electrochemical properties such as ECSA, double layer capacitance, and ionic resistance of PEM and CL would help to establish the activation mechanism, and I tried to estimate these electrochemical properties before and after activation.

1.3.3 Interface study

In MEA, there are many interfaces because more than five layers exist. Interface between CL and PEM is the most influential on MEA performance among the interfaces because electrochemical reaction occurs here most vigorously. Especially for the MEAs those are prepared by CCS method, hot-pressing is necessary to enhance adhesion force and interfacial stability. Moreover using perfluorosulfonic acid ionomer (PFSI), so-called Nafion solution, adhesion layer of PFSI film is deposited on the CL before hot-pressing to enhance the interface contact and area.[32,62] However addition of the PFSI film makes two interfaces between CL and PFSI film, and between PFSI film and PEM. The area and contact of the interface between CL and

PFSI film would be changed with the thickness of PFSI film as shown in Fig. 1.4. The stability of the interface between PFSI film and PEM would be improved by hot-pressing. In this study, I tried to separate and compare these two interfacial features by changing PFSI film thickness and hot-pressing, and estimated the electrochemical properties of cathode CL and PEM before and after activation.
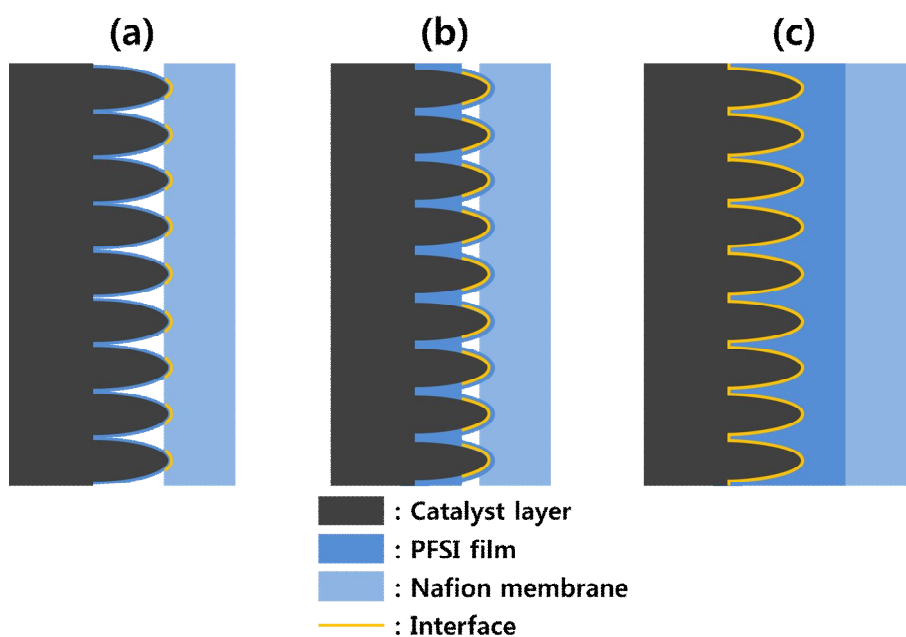
Figure 1.4. Interfaces between PEM and CL; (a) without PFSI film, (b) with thin PFSI film, and (c) with thick PFSI film on CL.

1.3.4 Transmission-Line Model

In this thesis, the TLM described in Fig. 1.5 (a) was used to analyze the CL. Because the CL of the MEA is a porous electrode, the TLM is appropriate to simulate and simplify the CL. In Lefebvre's study, ionic resistance and uniformity of resistance of the CL were shown by various plots.[48] Gazzarri et al. estimated the ionic resistance of the CL using the intersection of two straight lines in a Nyquist plot of EIS.[50] Gazzarri's method is very simple and easy to use to estimate the ionic resistance of the CL. However separating the high and low frequency region straight lines reduces the accuracy because the separation criterion is ambiguous. Jang et al. suggested a complex capacitance method to estimate ionic resistance of the CL.[51] Jang's method is also based on TLM, and ionic resistance was estimated by numerical integration of a complex capacitance plot without fitting. This method is logical and relatively accurate. However the process to obtain the ionic resistance value is complex, and some terms such as cell wire inductance, resistance of the PEM, and charge transfer resistance of crossovered H_2 gas must be removed from the measured data. These terms make it difficult to obtain accurate ionic resistance values for the CL. In other researches, various TLMs were used to analyze cathode CL not only in non-faradaic condition but also in faradaic condition. Nara et al. used TLM to analyze degradation of cathode CL in non-faradaic condition, and used TLM-based agglomerated model that considering primary and secondary pores to analyze the distribution of the oxygen reduction

reaction (ORR) in faradaic condition.[52] Y. Liu et al. also used TLMs for non-faradaic and faradaic conditions.[53] They quantified cathode proton resistance in a H_2/N_2 cell, and the measured data were applied to predict the performance of a H_2/O_2 cell. Lee et al. used TLM for analysis of the measured impedance spectra in faradaic condition, and the effect of annealing temperature of gas diffusion electrodes on proton transport resistance was shown.[54] In this thesis, I did not considered the faradaic reaction during the EIS measurement, and the intrinsic ionic resistance of CL was the interesting property. Therefore I used a modified TLM considering cell wire inductance (L_w), electrolyte resistance (R_{PEM}), and charge transfer resistance of the crossover H_2 (R_{X-over}), under a non-faradaic condition in this study (Fig. 1.5 (b)). Wire inductance is necessary to analyze the EIS data because a straight piece of wire has some self-inductance, and the effect of inductance is not negligible when the impedance is very low at high frequency region. Because one of the preconditions to use the TLM in Fig. 1.5 (a) is that the faradaic reactions never occur on active sites, the active sites can be regarded as capacitors. In the modified TLM, I assumed that the active sites where charge transfers occur would be a small part of the CL and would not affect most sites under non-faradaic charging in the CL. Therefore it was possible for the TLM to coexist with R_{X-over}. TLM was replaced by the generalized finite Warburg (open circuit terminus) element in the modified TLM to estimate $R_{i,CCL}$ and C_{dl} easily by fitting. The impedance of TLM (Z_{TLM}) and that of the Warburg element (Z_{Wo}) are described by:

$$Z_{TLM}(f) = \frac{R_{i,CCL}}{\sqrt{j\omega R_{i,CCL}C_{dl}}} \coth \sqrt{j\omega R_{i,CCL}C_{dl}}$$

$$Z_{W_o}(f) = \frac{R}{(j\omega T)^P} \coth (j\omega T)^P$$

where, $R_{i,CCL}$ is ionic resistance of the cathode CL, C_{dl} is double layer capacitance, ω is angular velocity, j is an imaginary unit, f is ac frequency, and R, T, and P are Warburg element fitting parameters.[49,63] Therefore I can fit the R and T values as $R_{i,CCL}$ and $R_{i,CCL} \cdot C_{dl}$ in the TLM, respectively. Moreover the variable P of Warburg element can compensate the difference of theoretical and real system. When the P value is smaller than 0.5, the Z_{Re}-axis of Nyquist plot is tilted below the x-axis. It is general phenomenon in real system due to the non-homogeneous nature or some distribution of the physical property of the system.
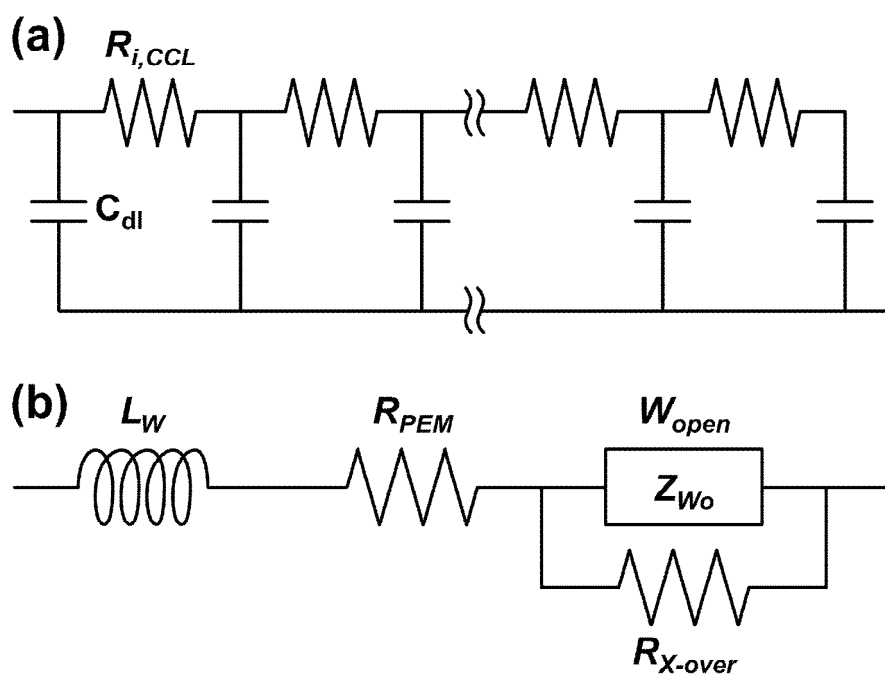
Figure 1.5. The equivalent circuits of (a) TLM and (b) modified TLM under the non-faradaic condition.

Chapter 2. Experimental

2.1 Preparation of Single Cell

2.1.1 Membrane Pretreatment

In this study, NR212 membrane (DuPont, Nafion 212) was used as the PEM. NR212, a kind of perfluorosulfonic acid membrane, has 50.8 μm thickness and 100 g m^{-2} weight.[64] NR212 sheet was cut down to 3.3 $\times$ 3.3 cm^2, and backing film and coversheet were peeled off. The bare membrane was immersed in 2.5% H_2O_2 solution of 80°C for 1 hr to remove organic contaminant, and then immersed in boiling de-ionized water for 1 hr. For protonation, membrane was immersed in boiling 0.5 M H_2SO_4 solution for 1 hr, and then rinsed in de-ionized water for purification. The membrane that was stored in de-ionized water was picked up and was taken between two drying templates. It was dehydrated at room temperature for over 12 hours.

2.1.2 Catalyst Ink Preparation and Spray Deposition

Pt loaded carbon black catalyst was used as electrocatalyst for anode and cathode of MEA. 20, 40, and 60 wt.% Pt/C (Johnson Matthey Co.) were used as electrocatalysts, and PFSI (5 wt.% Nafion solution, Aldrich) was used as ionomer in CL for proton conduction. PFSI content was optimized, and the optimum content is different with the Pt/C ratio of used catalyst. 40 wt.% of PFSI vs. catalyst was optimum content when 20

wt.% Pt/C was used, and 30 wt.% of PFSI vs. catalyst was optimum content for 40 and 60 wt.% Pt/C catalyst. These optimized PFSI content was used in each CL except for activation study. IPA (isopropyl alcohol) and DI water mixture was used as solvent for homogeneous dispersion of catalyst and ionomer in catalyst ink. This catalyst ink was ultrasonicated for 15 minutes. The prepared catalyst ink was sprayed on PEM or GDL. Spraying on both sides of PEM is called CCM method, and spraying on anode and cathode GDLs is called CCS method. SGL 35BC carbon paper that is consisted of 300 μm of hydrophobized (5 wt.% PTFE) carbon paper and 25 μm of standard microporous layer (MPL) was used in this thesis.[65] CL loading and thickness was controlled by changing deposition number. The weight of CL on GDL was estimated by weighting GDL before and after spray deposition, and CL weight on PEM was estimated indirectly by spraying same amount of catalyst ink on PET film and weighting PET film before and after spray deposition.

2.1.3 MEA Preparation

For thickness study, CCM method was used to prepare MEAs by spraying catalyst ink on both sides of dried PEM. The amount of platinum in anode CL for all of MEAs was fixed by 0.2 mg_{Pt} cm^{-2}. 40 or 60 wt.% Pt/C was used as anode catalyst and 20, 40, and 60 wt.% Pt/C was used as cathode catalyst. 40 wt.% Pt/C was used as anode catalyst when 20 or 40 wt.% Pt/C was used as cathode catalyst, and 60 wt..% Pt/C was

used as anode catalyst when 60 wt.% Pt/C was used as cathode catalyst. The amount of cathode catalyst was varied as $0.1 - 0.4$ mg$_{Pt}$ cm^{-2}. These prepared CCMs were sandwiched between two bare GDLs without hot-pressing, and MEA preparation was completed. For clear distinction, each MEA were named after the Pt/C ratio of cathode catalyst and Pt loading in cathode CL. For example, cathode CL of JM40-03 has 0.3 mg$_{Pt}$ cm^{-2} of 40 wt.% Pt/C. Therefore 12 MEAs were prepared with four different amounts of catalyst and with three different kinds of catalysts. MEAs for thickness study are listed in Table 2.

CCM method by spraying catalyst ink on both sides of dried PEM was also used to prepare MEAs for activation study. 0.2 mg$_{Pt}$ cm^{-2} of 40 wt.% Pt/C was deposited in anode and cathode CLs. The PFSI content in anode CL was the optimized content, 30 wt.%. The PFSI content in cathode CL was varied such as 10, 20, 30, and 40 wt.%. These prepared CCMs were sandwiched between two bare GDLs without hot-pressing, and MEA preparation was completed. These four MEAs were named after PFSI content in cathode CL such as PFSI10, PFSI20, PFSI30, and PFSI40.

For interface study, CCS method by spraying catalyst ink on anode and cathode GDLs was used. 0.21 ± 0.01 mg$_{Pt}$ cm^{-2} of 40 wt.% Pt/C and 30 wt.% of PFSI was used in anode and cathode CLs. After CL deposition on GDL, PFSI film was deposited on CLs by spraying PFSI solution. The amount of this PFSI film was varied such as 0.00, 0.10, and 0.35 mg cm^{-2}. Pretreated PEM was sandwiched between two

catalyst-coated GDLs and MEA preparation was completed by hot-pressing. The structures of MEAs those were prepared for interface study were shown in Fig. 2.1. Hot-pressing was carried out under 15.7 MPa at 130°C for 3 min. 130°C is slightly higher temperature than glass transition temperature of Nafion (ca. 120°C). This temperature would ensure that the membrane is soft enough to establish good contact with the electrocatalyst.[66] Spacer was used to prevent destruction of pore structure in GDL during hot-pressing. The thickness of spacer is 220 μm, and it is made on Teflon fiber.

2.1.4 Single Cell Fabrication

MEAs were applied in single cell for fuel cell test. Single cell that was used in this thesis is shown in Fig. 2.2. As shown in Fig. 2.2, gasket was used to prevent gas leakage and GDL over-compression, and it is same material with spacer. Two sheets of gasket and MEA were sandwiched between two bipolar plates. The bipolar plates with serpentine flow channel were made of graphite. For uniform pressure distribution in the single cell, alumina end plates were used on both sides of the single cell. The single cell module was assembled with eight screws with tightening torque of 7 N m through the end plates.

Table 2. Compositions of cathode catalyst layers for thickness study

Sample	Pt/C ratio	Pt loading ($mg_{Pt}\,cm^{-2}$)	PFSI content (wt.%)	N/C ratio
JM20-01	0.25	0.1	40	0.5
JM20-02	0.25	0.2	40	0.5
JM20-03	0.25	0.3	40	0.5
JM20-04	0.25	0.4	40	0.5
JM40-01	0.67	0.1	30	0.5
JM40-02	0.67	0.2	30	0.5
JM40-03	0.67	0.3	30	0.5
JM40-04	0.67	0.4	30	0.5
JM60-01	1.50	0.1	30	0.75
JM60-02	1.50	0.2	30	0.75
JM60-03	1.50	0.3	30	0.75
JM60-04	1.50	0.4	30	0.75

w/o hot press

w/ hot press

130°C
15.7 MPa
3 min.

IF00 PFSI film 0.00 mg cm^{-2} IF00HP

IF10 PFSI film 0.10 mg cm^{-2} IF10HP

IF35 PFSI film 0.35 mg cm^{-2} IF35HP

GDL   CL   PFSI film   Membrane
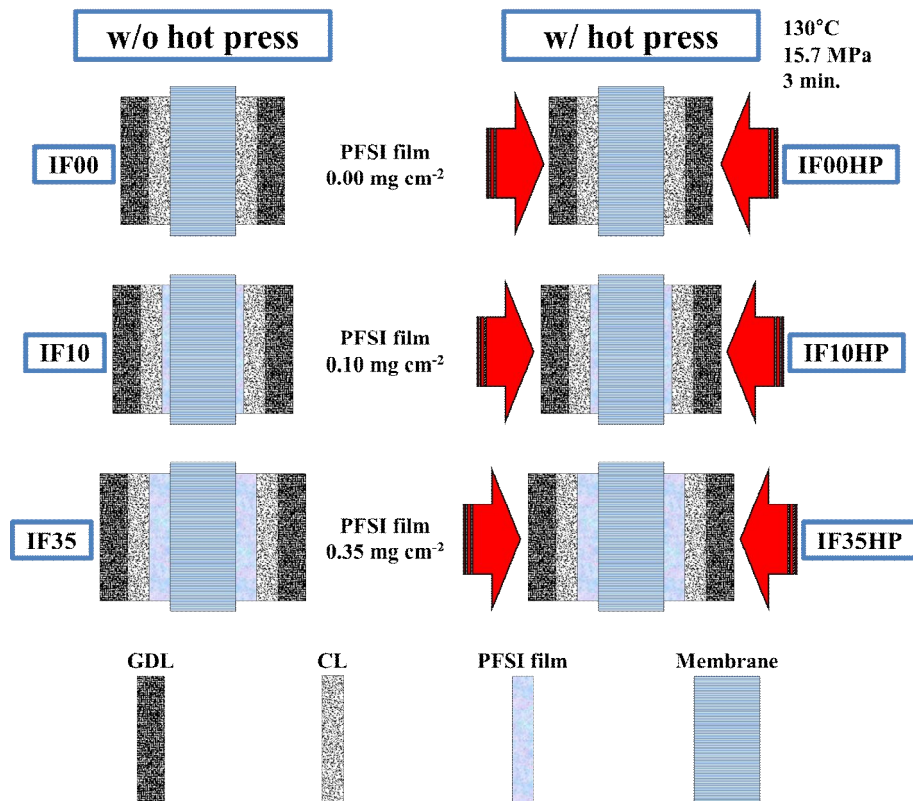
Figure 2.1. The structures of MEAs for interface study.
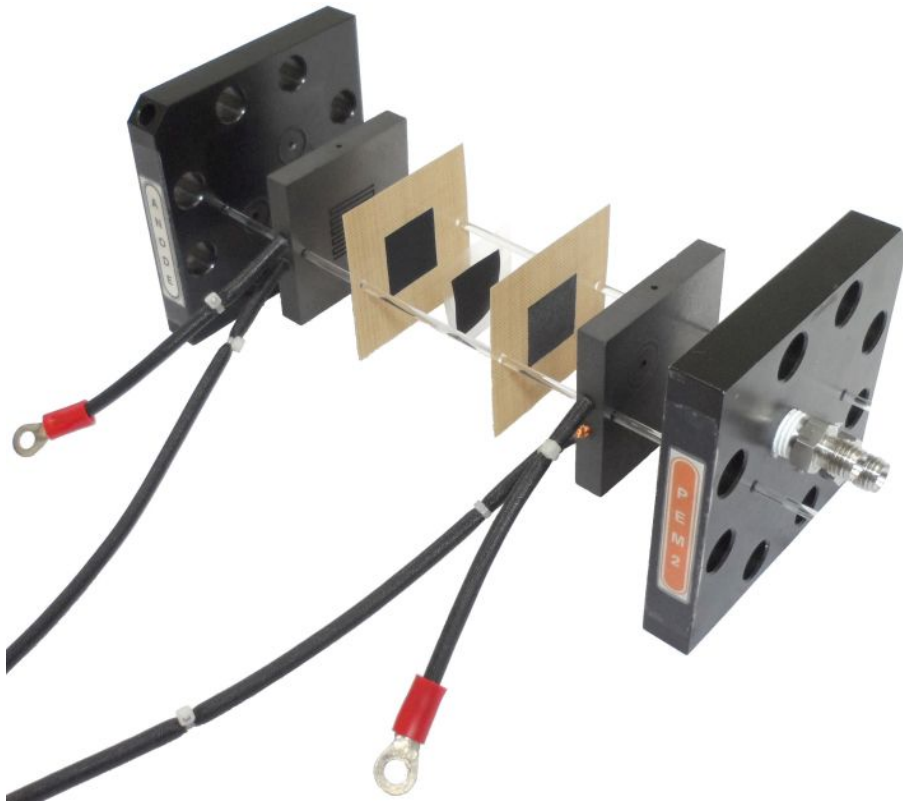
Figure 2.2. Image of single cell used in this thesis.

2.2 Single Cell Test and Analysis

2.2.1 Single Cell Activation and Polarization Test

Single cell activation was carried out by the current sweep-and-hold method with the Fuel Cell Test System (WonATech Co., Ltd., WFCTS 1.11). The current was maintained for 10 min when the current density was reached at each 1, 2, 3, 3.5, and 4 A cm^{-2} during a 10 mA cm^{-2} s^{-1} current sweep rate. During the activation process, current was reset to zero when the cell voltage reached 0.35 V. Humidified H$_2$ and O$_2$ were introduced to the anode and cathode sides, respectively, and cell temperature was maintained at 70°C. Flow rates of supplied H$_2$ (99%) and O$_2$ (99%) were fixed to 150 and 200 ccm, respectively.

Polarization curves were measured by the current sweep method at a 10 mA cm^{-2} s^{-1} rate using the Fuel Cell Test System. Cell temperature during polarization test was maintained at 70°C. Fully humidified H$_2$ was supplied to the anode, and fully humidified O$_2$ or air (99.9%) was supplied to the cathode. Flow rates of supplied H$_2$, O$_2$, and air during the polarization test were 150, 200, and 800 ccm, respectively.

2.2.2 Electrochemical Analysis

EIS (Zahner-elektrik, IM6ex combined with PP240) under the faradaic condition was measured for single cell analysis. The cell voltage of the EIS measurement was 0.4, 0.5, 0.6, 0.7, and 0.8 V with 10 mV amplitude, and the range of measured

32

frequencies was 100 kHz–100 mHz. During EIS measurement, fully humidified H_2 was supplied to the anode with 150 ccm of flow rate, and fully humidified air (99.9%) was supplied to the cathode with 800 ccm of flow rate. Cell temperature was maintained during polarization test at 70°C.

Single cell was purged with humidified N_2 gas on both sides for over 12 hr to remove reactive gases before CV (Zahner-elektrik, IM6ex combined with PP240) measurement. After N_2 purging, humidified H_2 was supplied to the anode side with 50 ccm of flow rate, and humidified N_2 gas (99.99%) was supplied to the cathode side with 200 ccm of flow rate. The working electrode was connected to cathode side to measure CV of cathode CL and reference electrode was connected to anode side. Cell temperature was maintained during CV measurement at 30°C. The voltage sweep range of CV was 0.05–1.20 V, and the scan rate was 100 mV s^{-2}. Number of CV cycles was 10 when CV was measured after activation and polarization test, and was 50 when CV was measured before activation. The ECSA of the cathode CL was estimated by hydrogen desorption charge of CV.

Non-faradaic EIS of a single cell was measured after the CV test to estimate ionic resistance and double layer capacitance of the cathode CL. Experimental conditions of non-faradaic EIS measurement such as electrode connection, cell temperature, and gas supplement were the same as those of CV measurement. DC voltage was 0.45 V with

10 mV amplitude, and the frequency range was 100 kHz–10 mHz. The ZView software (Scribner Associates Inc., v3.2c) was used to fit the EIS data.

2.2.3 Characterization of MEAs

The thickness and surface morphology of the CLs and CCMs were measured by field emission scanning electron microscopy (FE-SEM) (Carl Zeiss, SUPRA 55VP). Average crystallite size of the Pt in the Pt/C catalyst was estimated by X-ray diffraction (XRD) (Rigaku Corp., D-MAX2500-PC). The chemical surface area (CSA) was calculated by the estimated crystallite size and spherical assumption of Pt particle.

2.3 Experimental Procedures

For thickness study, assembled single cells of 12 MEAs from JM20-10 to JM60-40 were tested as shown in Fig. 2.3. All of MEAs were activated with H_2/O_2 reactants and polarization curves and faradaic EIS were measured with H_2/air reactants. Finally CV and non-faradaic EIS were measured after N_2 purging at 30°C.

Experimental procedure for activation study is shown in Fig. 2.4. In this study, four MEAs from PFSI10 to PFSI40 were tested, and CV, non-faradaic EIS, faradaic EIS, and polarization curves were measured before and after activation. Finally XRD of cathode CL was measured after activation. XRD of 40 wt.% Pt/C powder and as-deposited CL on NR212 were also measured.

Experimental procedure for interface study is shown in Fig. 2.5. Six MEMs from IF00 to IF35HP were tested in this study. CV and non-faradaic EIS were measured before and after activation, and the effects of their PFSI film thicknesses and hot-pressing process on performance were compared.
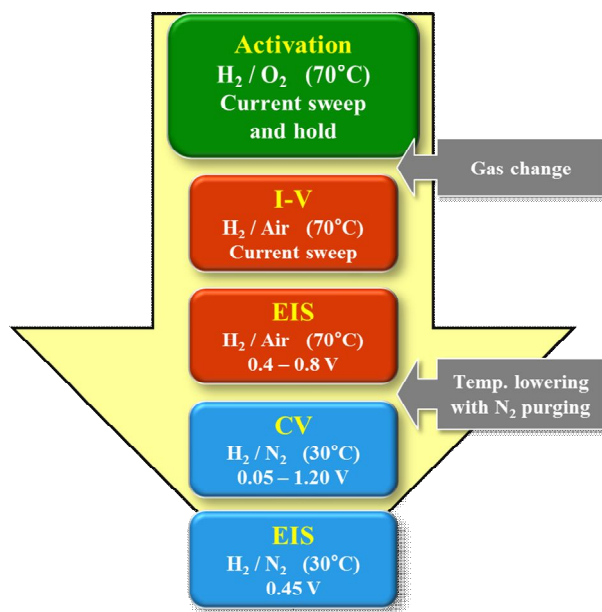
Figure 2.3. Experimental procedure for thickness study.
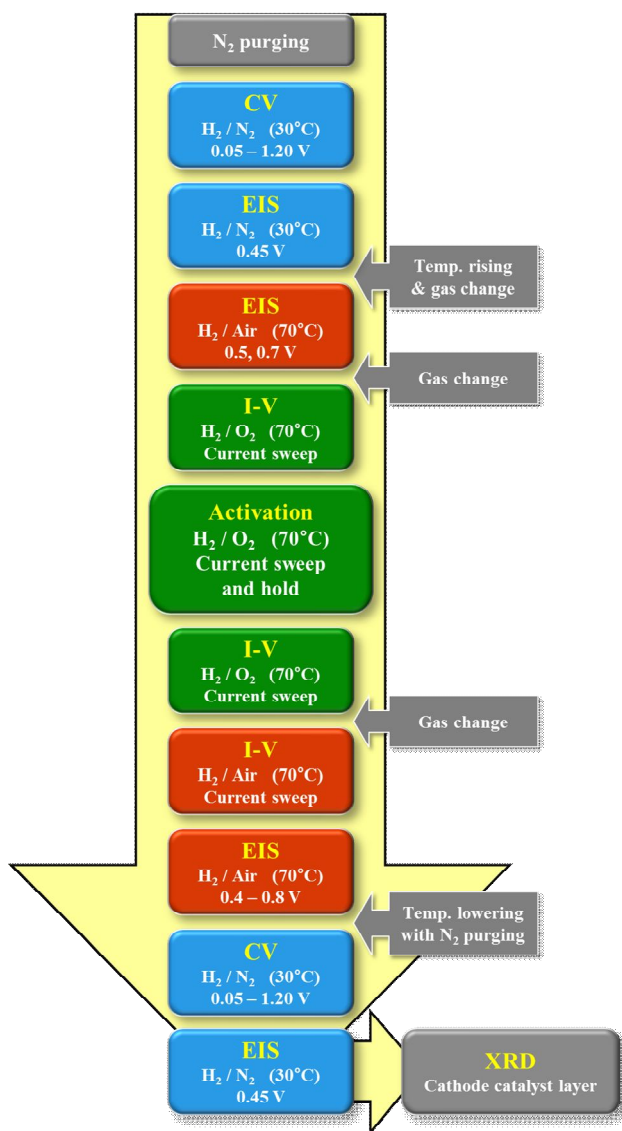
Figure 2.4. Experimental procedure for activation study.
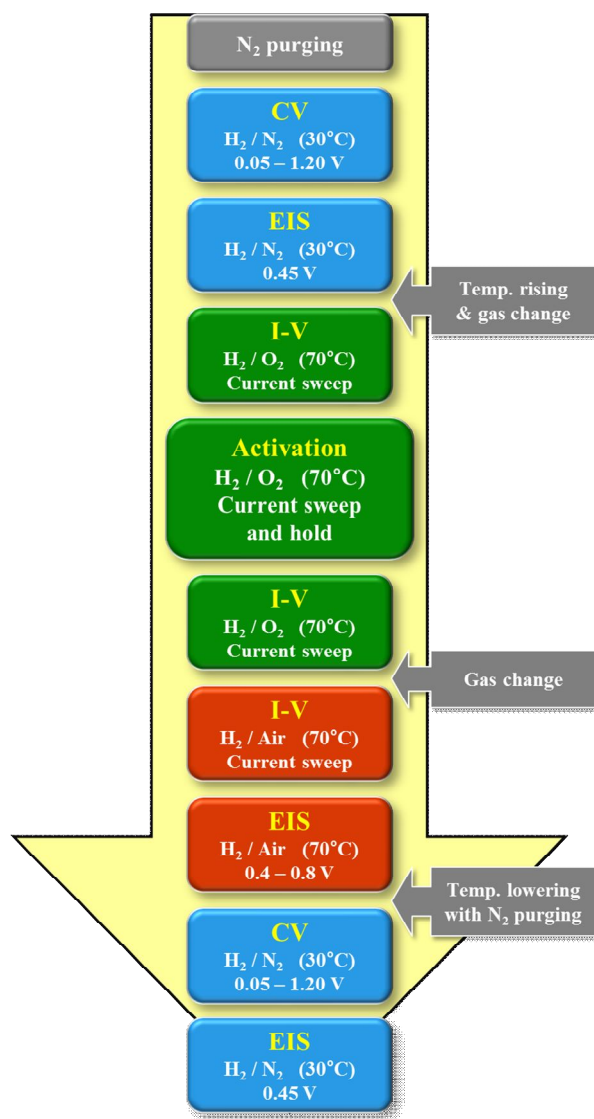
Figure 2.5. Experimental procedure for interface study.

Chapter 3. Results and Discussion

3.1 Thickness Study

3.1.1 Physical Characterization of Cathode Catalyst Layer

XRD of the 20, 40, and 60 wt.% Pt/C catalyst powders was measured and the patterns are shown in Fig. 3.1 (a). Crystallite sizes of the Pt nanoparticles were estimated by Gaussian fitting of the Pt (220) peak as shown in Fig. 3.1 (b) and using Debye-Scherrer equation:

$$t = \frac{K \times \lambda}{B \times \cos\theta_B} \tag{1}$$

where, t is thickness of the crystallite, shape factor K is a constant that depends on shape (0.89 for spherical crystallites), λ is wavelength of X-rays (1.54056 Å for CuKα), B is FWHM of the peak, and θ_B is the Bragg angle. The Pt crystallite sizes of 20, 40, and 60 wt.% Pt/C catalysts were 2.4, 3.0, and 4.6 nm, respectively. Because the Pt/C catalyst with a high Pt/C ratio is large, the peak shapes sharpened (4.00, 3.18, and 2.04 of FWHM) and the peak positions shifted to a high angle (67.07°, 67.34°, and 67.40° of 2θ). The CSA of Pt in the 20, 40, and 60 wt.% Pt/C, with the assumption of a spherical Pt particle, were estimated to 119, 94, and 60 m^2 g^{-1}, respectively.

Cross-section and surface FE-SEM images of the JM20-01, JM40-02, and JM60-04 cathode CLs are shown in Fig. 3.2. In Fig. 3.2 (a)–(c), the thicknesses of the JM20-

01, JM40-02, and JM60-04 cathode CL were similar approximately 8.4 ± 0.6 μm. Additionally, the surface structures of the CLs were so similar that these images could not be used to distinguish them, although the types were different. It is reasonable to assume that the CL structures were the same because the CL deposition method was the same.
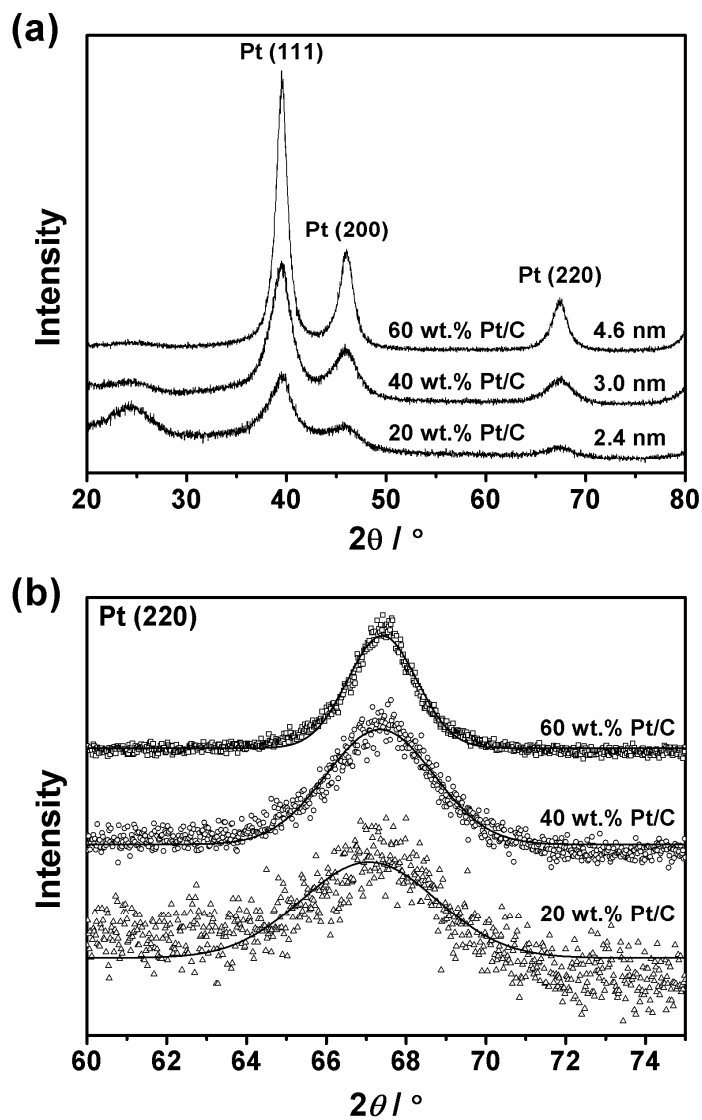
Figure 3.1. (a) XRD patterns of the 20, 40, and 60 wt.% Pt/C, and (b) those of magnified Pt(220) peaks (symbols) and Gaussian fitting results (lines).
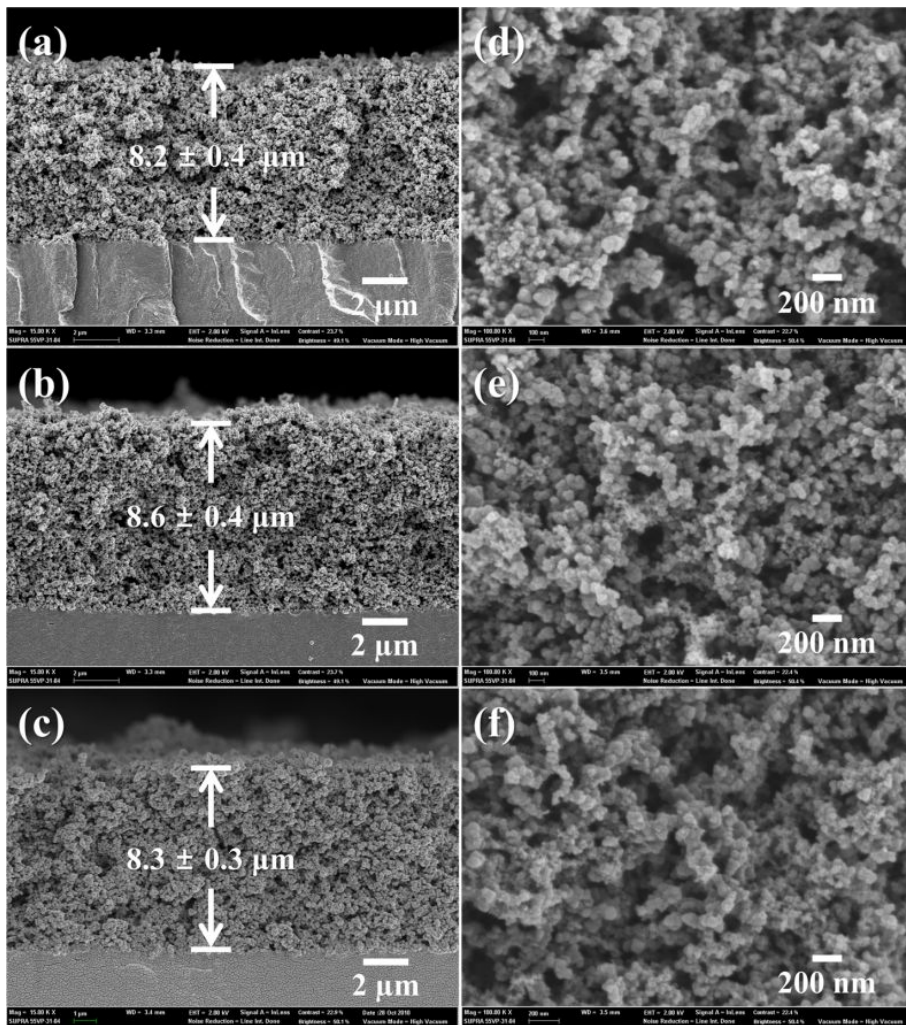
Figure 3.2. FE-SEM images of the cathode CL; cross-sectional images of (a) JM20-01, (b) JM40-02, and (c) JM60-04, and surface images of (d) JM20-01, (e) JM40-02, and (f) JM60-04.

3.1.2 Analysis of Polarization Curves

The MEA polarization curves are plotted in Fig. 3.3. In all MEAs, high loading of catalyst enhanced the performance in the high voltage region >0.6 V. This was a reasonable result caused by the increased Pt active site. Performance in the low voltage region, such as maximum power and current densities, were also enhanced until Pt loading reached particular values. The Pt loading for maximum performance in the low voltage region differed with the Pt/C ratio. Maximum power densities of the JM20, JM40, and JM60 MEAs occurred using 0.2, 0.3, and 0.3 mg_{Pt} cm^{-2} catalyst loading, respectively. This result was due to the increased concentration loss caused by increased cathode CL thickness. A thick cathode CL would interrupt oxygen penetration, proton transport, and the emission of generated water through the CL.

Current densities at 0.7 and 0.5 V during the polarization test ($i_{0.7V}$ and $i_{0.5V}$) are shown in Fig. 3.4. The $i_{0.7V}$ was proportional to the Pt loadings in Fig. 3.4 (a). The $i_{0.7V}$ values of 40 and 60 wt.% Pt/C were similar for each Pt loading, whereas those of 20 wt.% Pt/C were lower than others. This result was due to the low density of active sites in the CL near the membrane. Although the ECSAs of 20 and 40 wt.% Pt/C were similar and that of 60 wt.% Pt/C was much smaller than others, low volumetric surface area of Pt in the CL would decrease the $i_{0.7V}$ of the 20 wt.% Pt/C. In Fig. 3.4 (b), the Pt/C catalyst with a low Pt/C ratio was advantageous in the low voltage region when the catalyst amount was ≤ 0.2 mg_{Pt} cm^{-2}. When the catalyst amount was ≥ 0.3 mg_{Pt} cm^{-2},

the order of high performance for the catalyst was reversed, and the catalyst with a

high Pt/C ratio became advantageous.
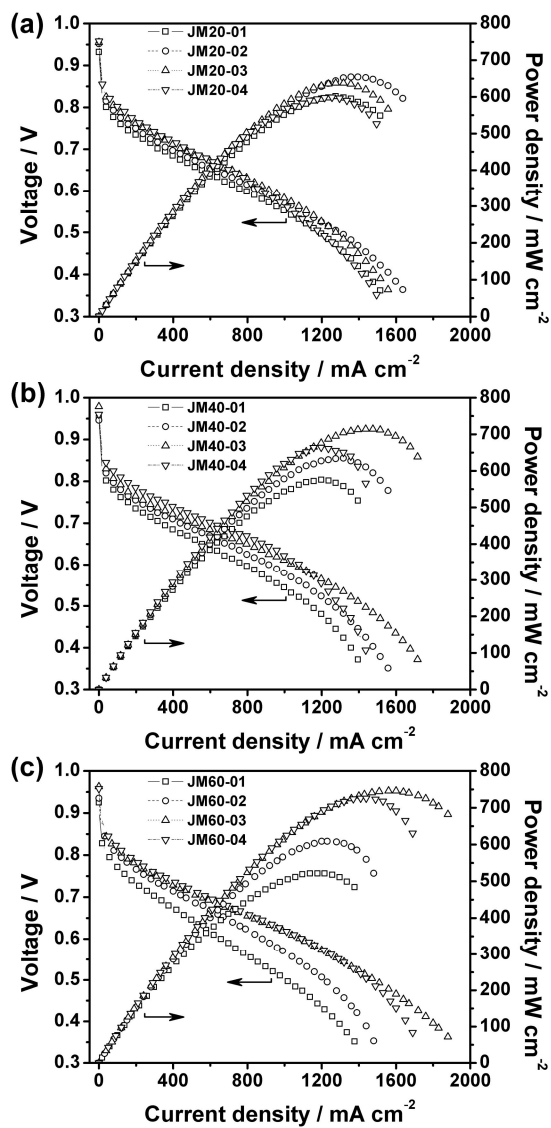
Figure 3.3. Polarization curves of (a) JM20, (b) JM40, and (c) JM60 MEAs under operating conditions with fully humidified H₂/air reactants.
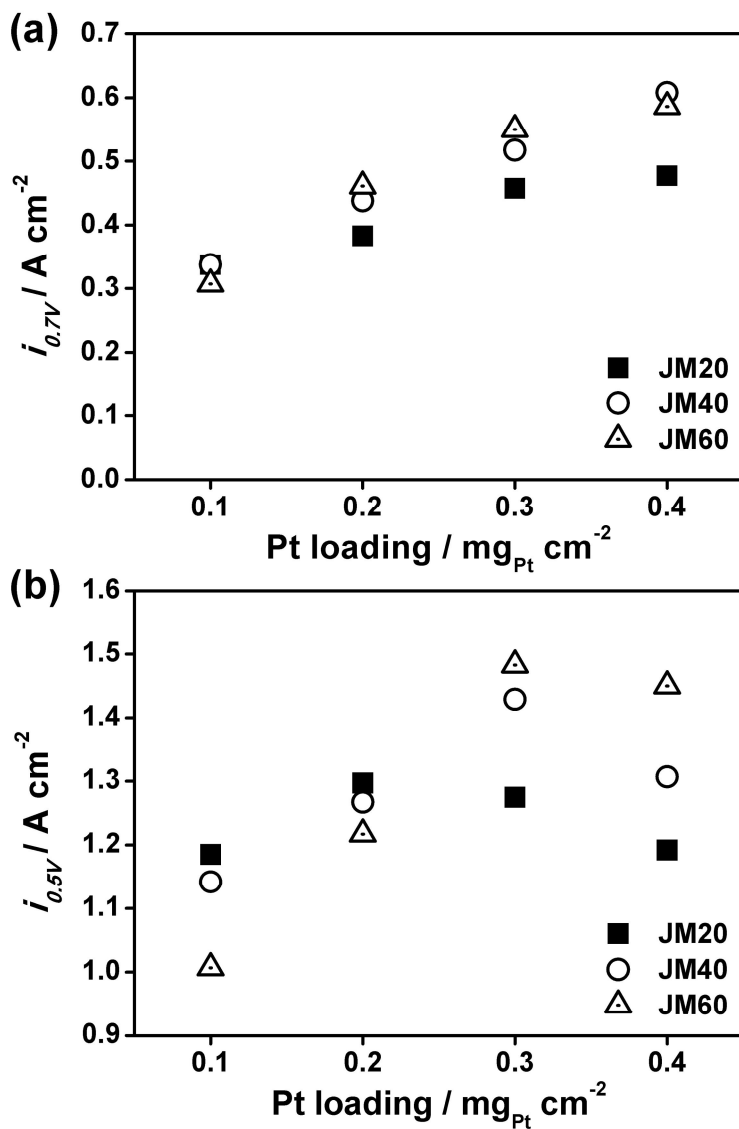
Figure 3.4. Current densities at (a) 0.7 ($i_{0.7V}$) and (b) 0.5 V ($i_{0.5V}$) from the polarization results.

3.1.3 Analysis of Faradaic EIS

The EIS results of operating with H_2/air reactants are shown in Fig. 3.5. The overall diameters of the impedance loops at 0.7 V in Fig. 3.5 (a) decreased with the increase in catalyst loading. This result was consistent with the polarization test results in Fig. 3.3, because the impedance diameters are proportional to the polarization curve slopes at the measuring cell voltage. From this point of view, the EIS results at 0.5 V in Fig. 3.5 (b) were also consistent with the polarization curves because the impedance diameters are proportional to the polarization curves at 0.5 V. However there is no relationship between the impedance diameter and catalyst loading because the concentration overpotential that is caused by mass transfer resistance has a large influence on the overall impedance at 0.5 V. Moreover, the semicircles were distorted, and the slope of the high frequency region became gentle when the Pt/C ratio was low. The shape of the slanting branches in the high frequency region in Fig. 3.5 (a) and (b) was due to high ionic resistance within the CL.[67,68] Ionic resistance within the CL seriously affected performance when the catalyst had a low Pt/C ratio, because cathode CL thickness with 20 wt.% Pt/C was four times thicker than that with 60 wt.% Pt/C.
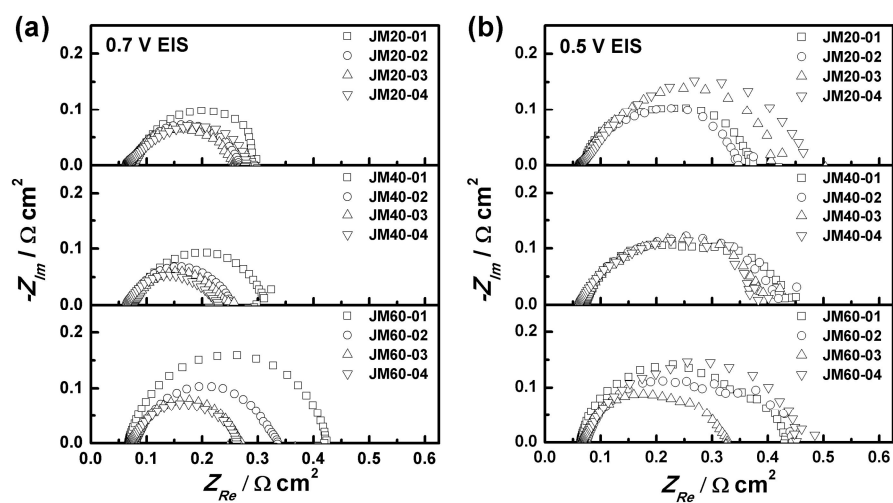
Figure 3.5. EIS Nyquist plots at (a) 0.7 and (b) 0.5 V under the operating condition with fully humidified H₂/air reactants.

3.1.4 Cyclic Voltammetry and ECSA

Cyclic voltammograms of the cathode CLs are shown in Fig. 3.6. Increasing the amount of Pt induced an increase in current density throughout the entire range. Catalysts with a low Pt/C ratio showed a thick double layer near the 0.4 V region, and remarkable redox peaks appeared at 0.6 V. This result would be due to the high ratio of exposed carbon surface, and these 0.6 V peaks are hydroquinine-quinone (HQ-Q) redox peaks caused by carbon oxidation.[20,69-72] ECSAs of cathode catalysts that were estimated by the CV are shown in Fig. 3.6 (d). ECSA was estimated by using Eq. (2):

$$ECSA = \frac{Q_H}{v \times W_{Pt} \times Q_{H,Pt(110)}} \tag{2}$$

where Q_H is hydrogen desorption charge [C], v is scan rate of CV measurement [V s^{-1}], W_{Pt} is weight of Pt in cathode CL [g], and $Q_{H,Pt(110)}$ is H$_2$ adsorption charge on Pt (110) surface, 2.1 C m^{-2}. The average hydrogen adsorption and desorption charge density on polycrystalline Pt is the same with that on Pt (111) 210 μC cm^{-2} for estimating ECSA.[73] The average ECSAs of the 20, 40, and 60 wt.% Pt/C catalysts were 67, 61, and 36 m^2 g^{-1}, respectively. Pt utilization efficiencies (U_{Pt}) of the 20, 40, and 60 wt.% Pt/C defined as the ECSA/CSA were 0.56, 0.65, and 0.59, respectively.[74,75] Low U_{Pt} is related to the anchoring of the recast PFSI on the Pt surface and to the inaccessibility of the protons to the Pt surface which are present in between the Pt crystallites and the carbon support.[76] Because the support material (Cabot Corp., Vulcan XC) structures and the CLs were the same, the U_{Pt} values were similar.
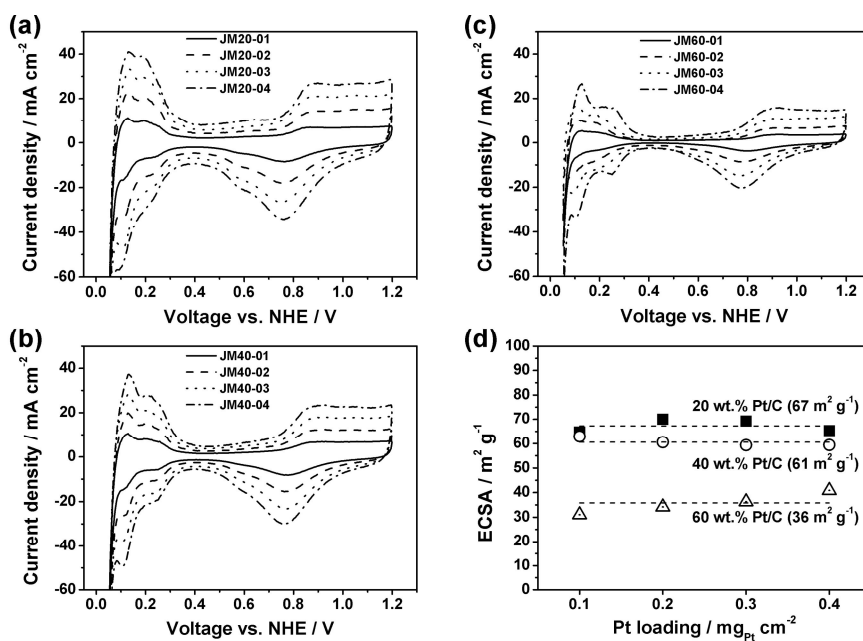
Figure 3.6. CVs of cathode CLs of (a) JM20, (b) JM40, and (c) JM60 under the non-faradaic condition with fully humidified H$_2$/N$_2$ feeds. (d) ECSAs of the Pt/C catalysts were estimated by the hydrogen desorption area in CVs.

3.1.5 Analysis of Non-Faradaic EIS with Modified TLM

The compositions of the cathode CLs and analyzed Warburg element fitting parameters with the modified TLM in Fig. 1.5 are listed in Table 3. The imaginary (C_{Im}) and real (C_{Re}) part of the complex capacitance of the measured results and fitted curves are shown in Fig. 3.7. The fitted curves (lines) were matched well with the measured results (symbols) even the resistive tails that were associated with the faradaic reaction at low frequency region. $C_{Im}(f)$ peak area A increased with catalyst loading. A is proportional to C_{dl} with the proportional factor of $\pi/(2 \ln 10)$, and C_{dl} is proportional to catalyst surface area.[74] The position of the $C_{Im}(f)$ peak shifted to low frequency with the increase in catalyst loading. The peak frequency was related to the C_{dl} and ionic resistance of the cathode CL ($R_{i,CCL}$). A negative shift in the peak frequency would imply an increase in C_{dl} and $R_{i,CCL}$.[77]

The estimated C_{dl} and $R_{i,CCL}$ by fitting the EIS data as shown in Fig. 3.7 are plotted in Fig. 3.8 with the thickness of the cathode CL. C_{dl} increased linearly with the thickness of the cathode CL regardless of the Pt/C ratio. The volumetric C_{dl} of the CL was estimated as 18 F cm^3 from the slope of Fig. 3.8 (a). Plot linearity implied that the C_{dl} was similar when CL thickness was the same, although the double layer capacitance of Pt is higher than that of C.[69,78] Moreover CL thickness could be estimated by measuring double layer capacitance. However these results are limited to the CLs that consisted of the Pt/Vulcan XC catalyst, which had a similar structure and

porosity produced by spray deposition. In Fig. 3.8 (b), the $R_{i,CCL}$ values also increased linearly with CL thickness, because resistance is proportional to length. The ionic resistivity of the CL, which was estimated with the slope was 50 Ω cm, and conductivity that is defined as a reciprocal number of resistivity was 0.020 S cm^{-1}. This CL ionic conductivity is similar to the state of a Nafion membrane at 30°C with 4.5 water content in Nafion (λ) and 0.64 water vapor activity, i.e., 64% of relative humidity.[79] These electrochemical properties would be hard to represent the characteristics under operating condition because of different temperature condition. In Fig. 3.8 (b), the intercepts of the 40 wt.% Pt/C and others were not zero; moreover, the values were not the same, but I'm unclear of the reason. One of the doubtful points is the interfacial resistance of the MEA between membrane and both sides of the CLs. Therefore further study is necessary to establishing the cause. The important thing is that high ionic resistance could be an important factor of the limitation of performance enhancement.

Table 3. Physical and electrochemical properties of cathode catalyst layers for thickness study

Sample	Thickness (μm)	ECSA (m^2 g^{-1})	$Z_{W\dot{o}\text{-}R}$ (Ω cm^2)	$Z_{W\dot{o}\text{-}T}$ (s)	$Z_{W\dot{o}\text{-}P}$
JM20-01	8.2	65	0.0721	0.000951	0.4879
JM20-02	16.4	70	0.1187	0.003431	0.4887
JM20-03	24.6	69	0.1595	0.006514	0.4874
JM20-04	32.8	65	0.1880	0.012023	0.4913
JM40-01	4.3	63	0.0697	0.000604	0.4899
JM40-02	8.6	61	0.1013	0.001606	0.4903
JM40-03	12.9	59	0.1147	0.002886	0.4888
JM40-04	17.2	59	0.1388	0.004120	0.4888
JM60-01	2.1	31	0.0420	0.000158	0.4906
JM60-02	4.2	34	0.0556	0.000374	0.4889
JM60-03	6.2	36	0.0520	0.000625	0.4860
JM60-04	8.3	41	0.0719	0.001080	0.4901
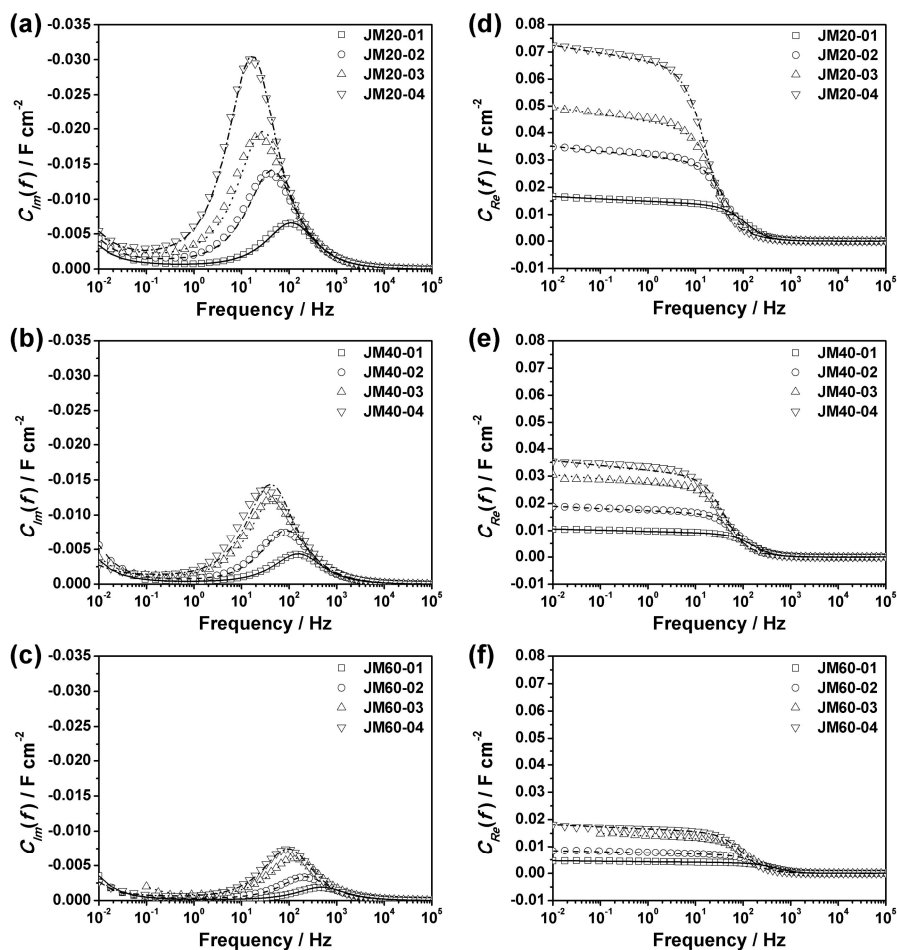
**Figure 3.7. EIS imaginary capacitance plots of the cathode CLs of (a) JM20, (b) JM40, and (c) JM60 under a non-faradaic condition with fully humidified H$_2$/N$_2$ feeds. Experimental data (symbols) and fitted results using the modified TLM (lines).**

54
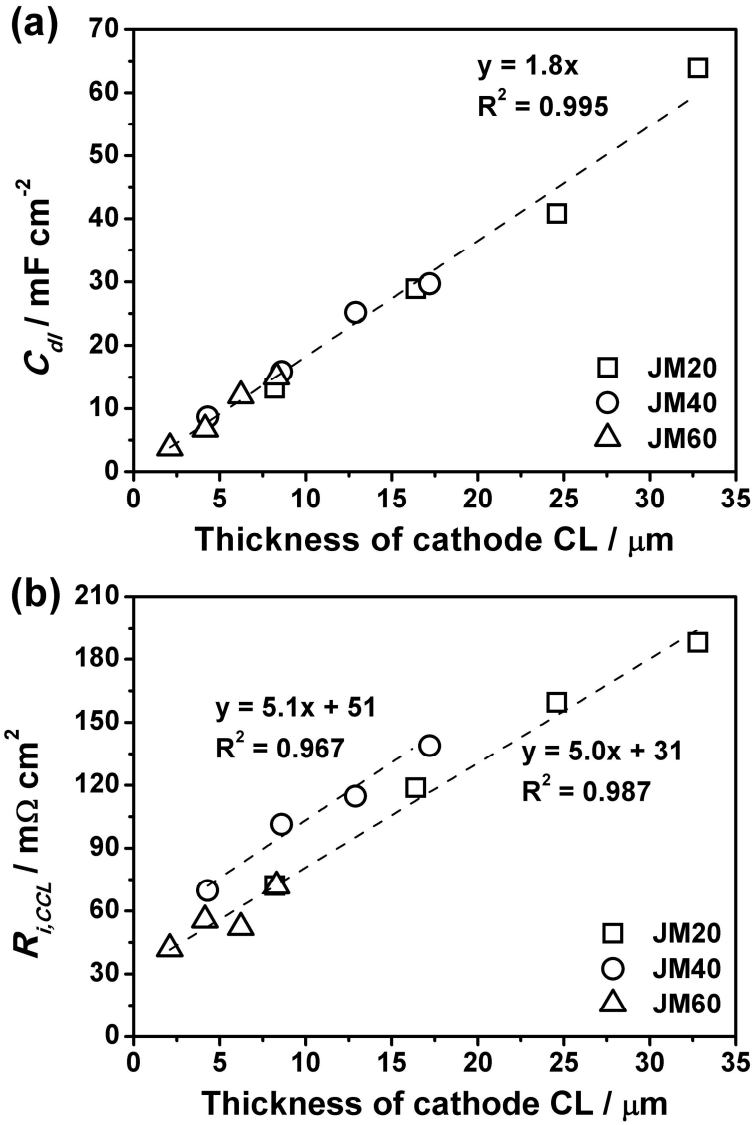
Figure 3.8. (a) (a) Double layer capacitance (C_{dl}) and **(b)** ionic resistance of the cathode CL ($R_{i,CCL}$) by fitting the EIS data with the thickness of the cathode CL.

3.1.6 Fitting of Faradaic EIS

A general equivalent circuit for PEMFC under the operating condition is showed in Fig. 3.9 (a). This circuit contains wire inductance (L_w), constant phase element of anode electrode (CPE_{anode}), charge transfer resistance at anode side (R_{anode}), electrolyte resistance (R_{PEM}), constant phase element of cathode electrode ($CPE_{cathode}$), charge transfer resistance at cathode side ($R_{cathode}$), and Warburg element (short circuit terminus) that is related with mass transfer resistance. The EIS data that was measured at 0.5 V under faradaic condition in Fig. 3.5 was fitted with this equivalent circuit, and one of the Warburg parameter Z_{Ws}-R that has the dimension of resistance could be estimated and shown in Fig. 3.9 (b). Z_{Ws}-R was increased with the thickness of cathode CL. The mass transfer resistance is the interruption of the oxygen transport from the GDL to the catalyst. The interruption is increased with the water formation because generated water blocks the oxygen pathway in the CL. 0.5 V of cell voltage is in high current region, and product water would be generated vigorously at this cell voltage. Since the thick cathode CL interrupts water emission to the GDL, the mass transfer resistance is proportional to the thickness of cathode CL. The EIS data of JM20, JM40, and JM60 at 0.5, 0.6, and 0.7 V under faradaic condition were fitted, and the estimated double layer capacitances (C_{dl}) of cathode CLs are shown in Fig. 3.9 (c). The dashed line A is same with the trend line in Fig. 3.8 (a). In Fig. 3.9 (c), the double layer capacitances were increased with the thickness of cathode CL. However over 10 μm,

the slope became gentle and C_{dl} was limited under 25 mF cm^{-2}. The slope decrease is not shown under non-faradaic condition, and it implies that there is an effective thickness of cathode CL. Increase of cathode CL thickness caused increase of mass transfer resistance as well as increase of ionic resistance. Therefore the mass transfer resistance is also an important factor of the limitation of performance enhancement.
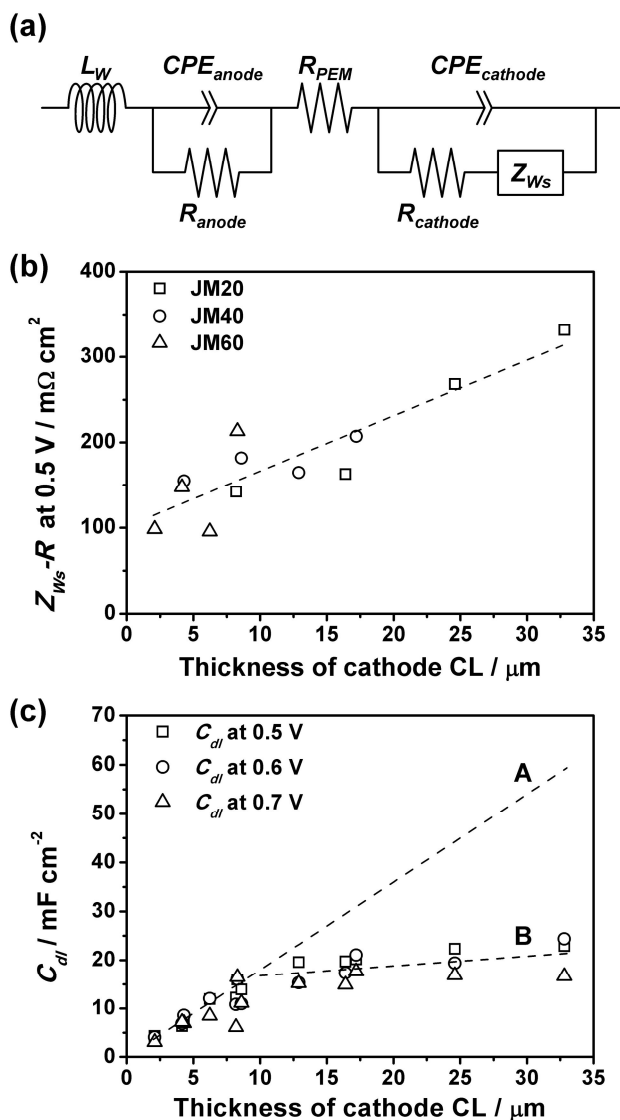
Figure 3.9. (a) Equivalent circuit of PEMFC under the faradaic condition. The fitting results; (b) resistive Warburg parameters (Z_{Ws}-R) at 0.5 V and (c) double layer capacitance (C_{dl}) of JM20, JM40, and JM60 cathode catalyst layers at 0.5, 0.6, and 0.7 V.

3.2 Activation Study

3.2.1 XRD Measurement and Particle Size Estimation

XRD patterns of 40 wt.% Pt/C powder, as-deposited CL on NR212, and cathode CLs of PFSI10, PFSI20, PFSI30, and PFSI40 after activation are shown in Fig. 3.10 (a). Pt(220) peaks were fitted to Gaussian distribution as shown in Fig. 3.10 (b), and the crystallite sizes of Pt were estimated by using Eq. (1). Pt particle size changes during MEA preparation and single cell activation were shown in Fig. 3.10 (c). Average Pt particle size in as-deposited CL was 0.3 nm larger than Pt/C powder. It means that catalyst ink preparation and spray deposition could affect on Pt growth although heating process such as hot-pressing was never done during CCM preparation. The probable cause of particle growth would be the high acidity of PFSI solution and ultrasonication process of catalyst ink. After activation, average Pt particle in cathode CL was grown about 0.4 nm, and totally 0.7 nm of particle growth was occurred during CCM preparation and activation process. It would be due to high potential, high cell temperature, heat of reaction, and oxidative condition of cathode CL. The dissolved Pt particle can re-deposit on other Pt particle, and Pt migration and fusion would occur during activation.
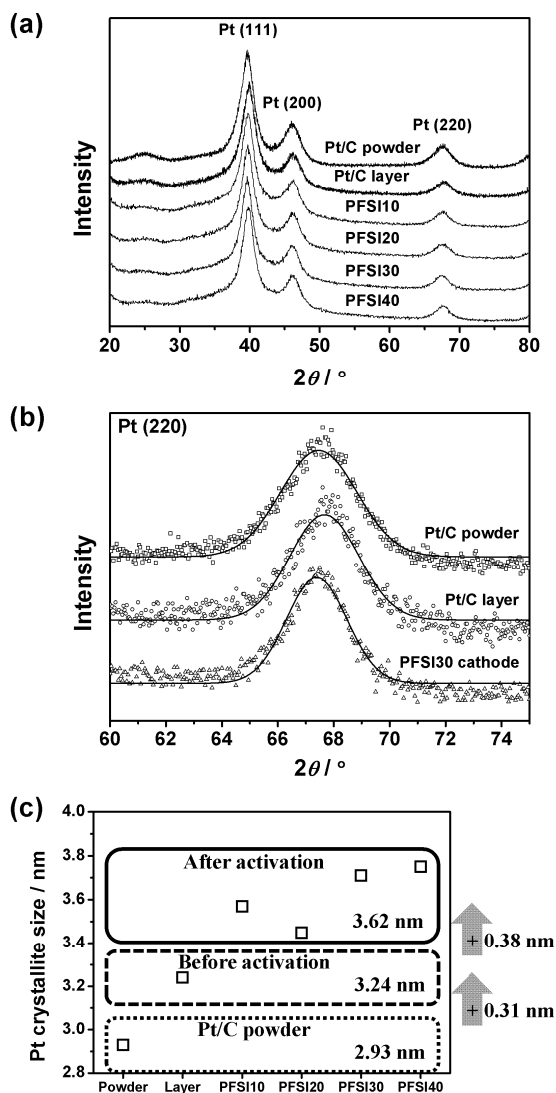
Figure 3.10. (a) XRD patterns of 40 wt.% Pt/C powder, as-deposited CL on NR212, and cathode CLs of PFSI10, PFSI20, PFSI30, and PFSI40 after activation, and (b) those of magnified Pt(220) peaks (symbols) and Gaussian fitting results (lines). (c) Pt crystallite sizes of samples in (a).

3.2.2 Cyclic Voltammetry and Pt Utilization Efficiency

Cyclic voltammograms of as-prepared and activated PFSI10, PFSI20, PFSI30, and PFSI40 were shown in Fig. 3.11. Shape of CVs were changed after activation especially hydroxide anion (OH⁻) adsorption and desorption region. However it is hard to compare detail shape changes of CVs using Fig. 3.11. CV of PFSI40 was slightly shifted to upward in Fig. 3.11 (a) and (b). It would be due to hydrogen crossover through Nafion membrane from anode to cathode, and the hydrogen oxidation current would affect on CV. Small size of scratch or pinhole might be formed during MEA preparation.

First of all, ECSAs were estimated by using hydrogen desorption charges and Eq. (2). The ECSA values of each sample were shown in Fig. 3.12 (a). ECSA was slightly decreased with increase of PFSI content. It could be the experimental error, or increased PFSI can increase the number of electrically insulated catalyst. The important thing is that the ECSAs were decreased after activation process, and the decreasing ratio was not changed with the change of PFSI content in cathode CL. The decreasing ratio was $7.95 \pm 0.15\%$, and it would be due to the increase of Pt particle growth during activation. In other researches, ECSA is decreased after activation, and the researchers say that the increase of ECSA is one of the reasons for performance enhancement after activation.[80-84] However their insistence can be refuted by this contrary result. Enhanced ORR activity of Pt by increased particle size would be

possible to explain the performance enhancement rather than increase of catalytic active sites.[85,86] One certain thing is that CL structure and CV measuring condition for as-prepared MEA in this study would be optimized for electrochemical test. Therefore it would be due to the difference of CL deposition method and experimental condition. U_{Pt} was slightly increased except for PFSI20 as shown in Fig. 3.12 (b), and it would be reasonable saying that U_{Pt} was not changed after activation. Because ECSAs were decreased about 8% and Pt size was increased about 0.4 nm, U_{Pt} showed consistent value, about 0.67. Z. Qi et al. insisted that the activation process increases catalyst utilization by opening many "dead" regions in the CL.[58] They also said that although a proton conductor such as Nafion is mixed into a CL to make it conduct proton in three dimensions, many of the catalyst sites are not available for reaction due to various reasons such as (1) blockage of pore and interruption of reactant diffusion to the reaction sites, (2) dehydration of Nafion near the catalyst sites, and (3) insulation of ionic or electronic pathway to the reaction sites. (1) and (2) could be changed during activation, however (3) was not shown in this study because U_{Pt} was not changed. Although the ionic or electronic conductivity could be increased, the initially insulated sites were not changed to active sites after activation.
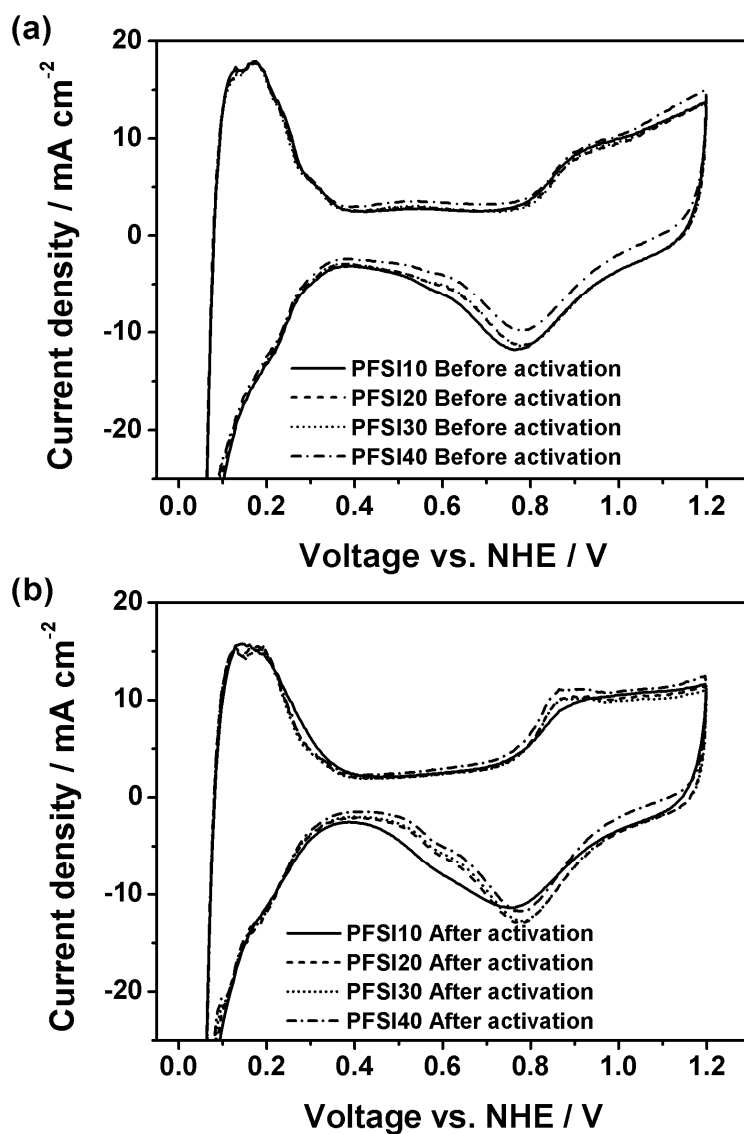
Figure 3.11. CVs of cathode CLs for (a) as-prepared and (b) activated MEAs.
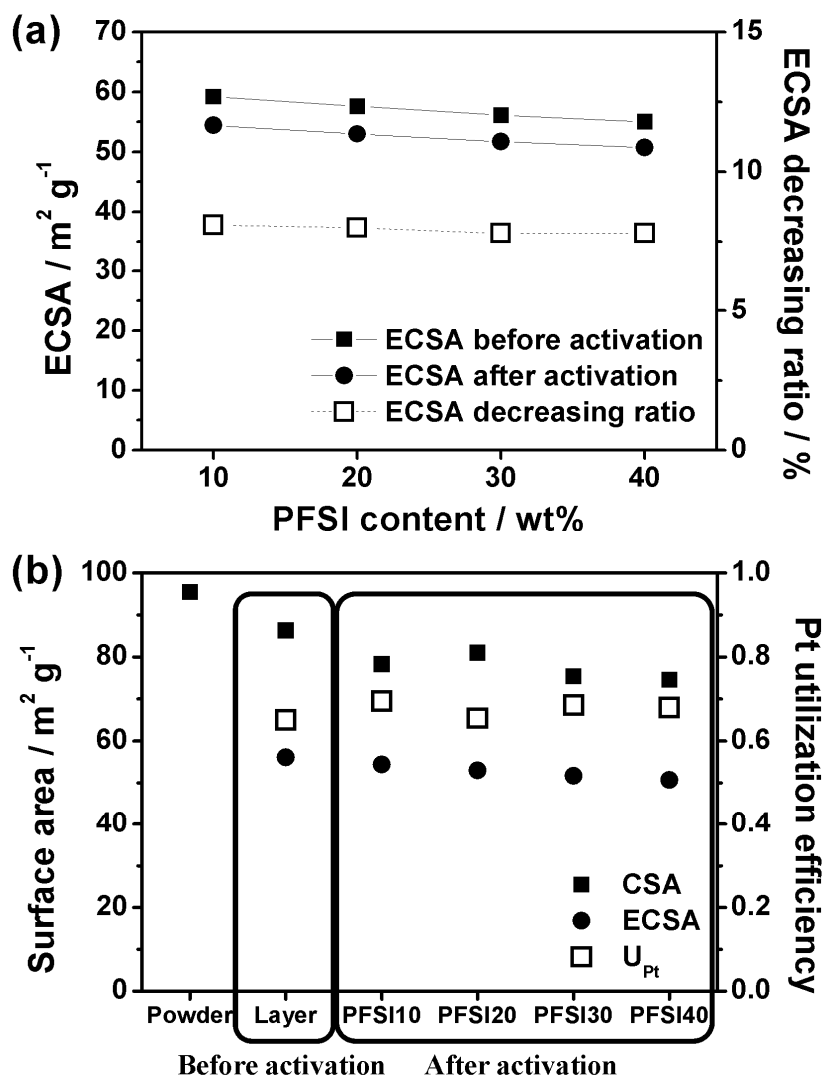
Figure 3.12. (a) ECSA values and decreasing ratio of cathode CLs for PFSI10, PFSI20, PFSI30, PFSI40, and (b) Pt utilization efficiencies those were calculated from CSAs and ECSAs.

3.2.3 Analysis of Normalized Cyclic Voltammetry

Cyclic voltammograms in Fig. 3.11 is hard to compare the shape changes with activation. Therefore all of the current densities in CVs were normalized by their hydrogen desorption charges (Q_H), and the $i \times Q_H^{-1}$ plots were shown in Fig. 3.13. Normalized CVs in Fig. 3.13 show four things of shape change after activation; (1) top of the hydrogen desorption peak at 0.18 V is changed and the difference is increased with increase of PFSI content, (2) thickness of double layer between 0.40 and 0.55 V was decreased, (3) onset potential of hydroxide anion (OH⁻) adsorption peak was shifted to negative potential and top of the peak was flattened, (4) and Pt reduction peak (or hydroxide anion desorption peak) near 0.77 V was increased. Decrease of Pt reduction peak would be caused by decrease of OH⁻ adsorption charge, and it is due to the negative shift of OH⁻ adsorption peak. The flattened shape of the OH⁻ adsorption peak would be due to the cleaning of Pt surface after activation because impurities can affect on OH⁻ adsorption.[87-88] Decreased double layer thickness would be due to disappearance of a redox peaks near 0.5 V those were shown on CV of as-prepared MEAs. Differences of normalized current density between as-prepared and activated MEAs, $\Delta(i \times Q_H^{-1}) = (i \times Q_H^{-1})_{before} - (i \times Q_H^{-1})_{after}$, were plotted in Fig. 3.14 for detail comparison of CV change. The forward scans (straight lines) have positive values and backward scans (dashed lines) have negative values under 0.6 V because double layer thickness of as-prepared MEA was thicker than that of activated MEA in Fig. 3.13.

However forward scans have negative values and backward scans have positive values from 0.6 V to 1.1 V because OH$^-$ adsorption and desorption charge of as-prepared MEA was smaller than that of activated MEA.

Four regions of Fig. 3.14 is enlarged and shown in Fig. 3.15. The differences of hydrogen adsorption-desorption (HAD) peaks between as-prepared and activated MEAs are clearly shown in Fig. 3.15 (a). There were four peaks at 0.100, 0.180, 0.245, and 0.325 V for cathode CL of PFSI10. These four peaks were also shown for cathode CL of PFSI20, PFSI30, and PFSI40. However the peak positions of them were slightly shifted to negative potential such as 0.090, 0.165, 0.240, and 0.300 V. Hydrogen desorption peak positions of polycrystalline Pt is not consistent because the ratio of surface structures such as Pt(111), Pt(100), and Pt(110) for polycrystalline Pt is different. Moreover specific adsorption of anion can affect on the HAD peak position, and the effect depends on the anion structure and surface structure of Pt.[87,89-92] In single cell test, the electrolyte is Nafion. The anion in Nafion, sulfonate anion (RSO$_3^-$) in PFSI, can affect on Pt because sulfonate anion also has tetrahedral structure. R. Subbaraman et al. showed that Nafion is not a non-adsorbing electrolyte and that in perchloric acid solution, the sulfonate groups present in the Nafion structure are indeed specifically adsorbed on well-characterized Pt single crystal surfaces, Pt-poly, high-surface-area catalysts, and Pt-skin surfaces.[16] In Fig. 3.16, CVs of 40 wt.% Pt/C in 0.5 M sulfuric acid (H$_2$SO$_4$) and 0.1 M perchloric acid (HClO$_4$) electrolyte are shown.

Because perchlorate anion (ClO_4^-) is not specifically adsorb on Pt surface, broad single hydrogen desorption peak was shown. However in sulfuric acid, there were four peaks at 0.109, 0.183, 0.225, and 0.310 V because of the anion effect on Pt surface. Moreover these peak positions were similar to the peak positions in Fig. 3.15 (a). Therefore the peaks in Fig. 3.15 (a) would be related to the sulfonate anion adsorption on Pt. Because the y-axis of Fig. 3.15 (a) means the differences between CVs of as-prepared and activated MEAs, it is possible to say that the interaction between Pt and sulfonate anion in PFSI was strong before activation, and the interaction was weakened after activation. The strong interaction between Pt(111) and sulfonate anion also shown in Fig. 3.15 (b). There is a pair of adsorption-desorption peaks at 0.49 V, and it would be the sulfonate anion adsorption-desorption peaks on Pt(111) surface.[16] This peak was also shown at half cell CV of H_2SO_4 electrolyte in Fig. 3.16. As shown in Fig. 3.13 and Fig. 3.15 (b), this adsorption-desorption peaks were increased with increase of PFSI content in cathode CL. It means that the portion of Pt(111) sites which interact strongly with PFSI is increased with increase of PFSI content, and this interaction was removed after activation. One interesting thing is that the relative intensity of 0.165 V peak in Fig. 3.15 (a) was increased with increase of the peak in Fig. 3.15 (b). Therefore it could be supposed that the 0.180 V peak is hydrogen desorption peak on Pt(111). Strong interaction between Pt and PFSI would interrupt OH^- adsorption for as-prepared MEA. In other words, onset potential of OH^-

adsorption peak was shifted to positive potential after activation because the interaction between Pt and PFSI was removed. In the case of PFSI10, difference of Pt reduction peak at 0.78 V was not shown in Fig. 3.14. Since the low PFSI content in PFSI10 results low interaction between PFSI and Pt, the difference of OH⁻ adsorption charges between as-prepared and activated MEA was smaller than other cases as shown in Fig. 3.13. Therefore the difference of Pt reduction peak for PFSI in Fig. 3.14 was not shown. One interesting thing is that the HQ/Q redox peaks at 0.6 V caused by carbon oxidation were increased after activation as shown in Fig. 3.15 (c). Hydroquinone (benzene-1,4-diol, $C_6H_4(OH)_2$) can be oxidized to quinine (1,4-benzoquinone, $C_6H_4O_2$) and it is reversible reaction. HQ/Q redox couple caused by the surface oxide formation on the carbon black support surface.[20,69-71] The reaction of HQ-Q redox can be formulated as the following:[72]

$$C=O + e^- + H^+ \leftrightarrow C–OH$$

Because dashed line is backward sweep, positive value means that the reduction peak was increased after activation. Surface of the carbon black support in cathode CL would be oxidized during activation and therefore this redox reaction would be enhanced. However, increasing ratio was decreased with PFSI content in Fig. 3.15 (c). It would be due to high PFSI coverage on carbon surfaces when the content of PFSI is increased, and PFSI coverage would cause the disruption of surface oxide formation on carbon.
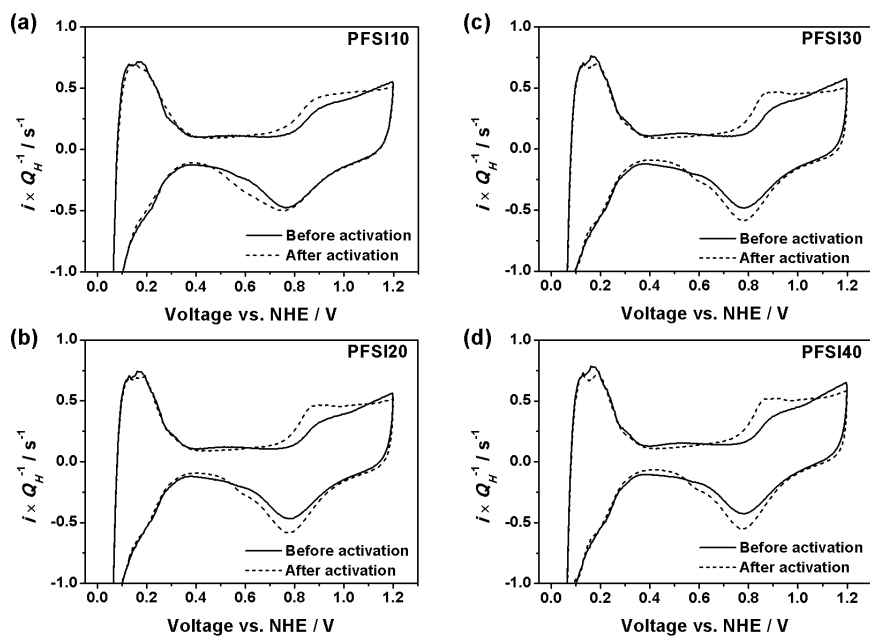
Figure 3.13. $i \times Q_H^{-1}$ **plots of cathode CLs for (a) PFSI10, (b) PFSI20, (c) PFSI30, and (d) PFSI40.**
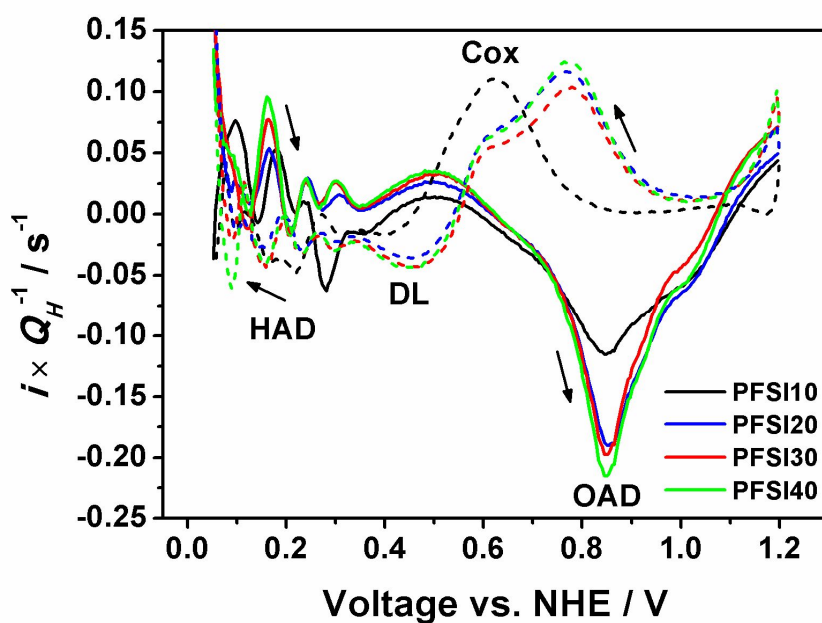
Figure 3.14. $(i \times Q_H^{-1})_{before} - (i \times Q_H^{-1})_{after}$ of cathode CLs for PFSI10, PFSI20, PFSI30, and PFSI40. Forward sweeps (lines) and backward sweeps (dashes).
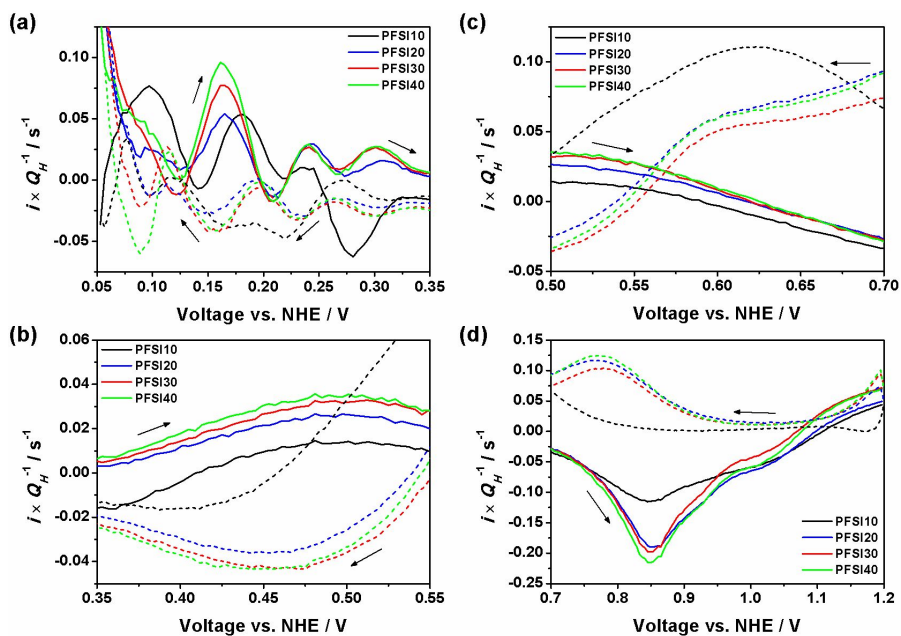
Figure 3.15. Magnified plots of CVs in Fig. 3.14; (a) HAD, (b) DL, (c) Cox, and (d) OAD region. Forward sweeps (lines) and backward sweeps (dashes).
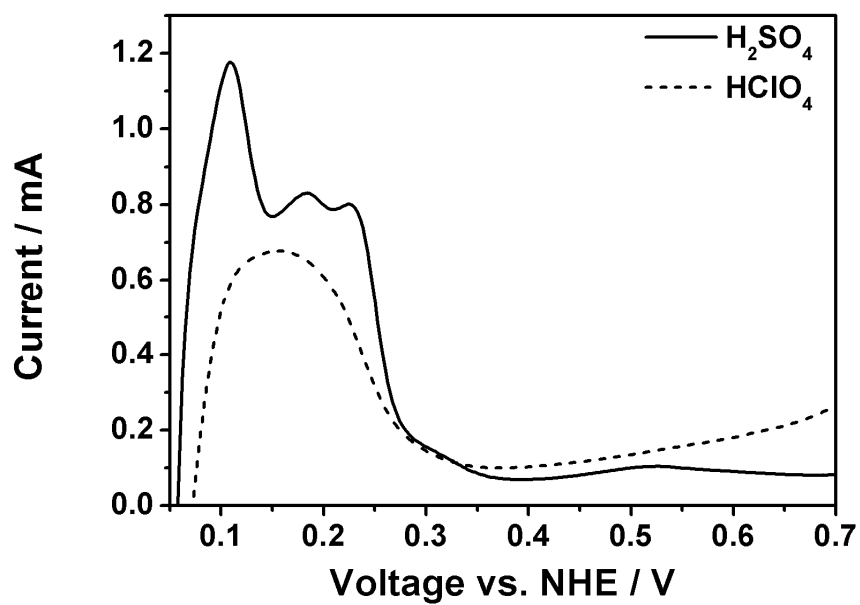
Figure 3.16. CV of JM 40 wt.% Pt/C in 0.5 M H₂SO₄ (solid) and in 0.1 M HClO₄ solution (dash) at HAD region.

3.2.4 Analysis of Non-Faradaic EIS

Non-faradaic EIS Nyquist plots of cathode CLs for as-prepared and activated MEAs are shown in Fig. 3.17 (a) and (b), respectively. The slope in Nyquist plot was increased with increase of PFSI content in both cases. The limiting value of Z_{Re} in low frequency is proportional to ionic resistance of CL.[48,50] Therefore the ionic resistance of cathode CL would be decreased with increase of PFSI content. The overall-range Nyquist plots of as-prepared and activated MEAs are shown in inset of Fig. 3.17. The shapes of Nyquist plots at low frequency region were similar because it is related with charge transfer resistance of crossovered hydrogen oxidation. The shape of PFSI40 is different with that of others because hydrogen crossover in PFSI40 would be higher than others. This result is consistent with the up-shifted CV of PFSI40 as shown in Fig. 3.13.

The EIS results in Fig. 3.17 were fitted by using modified TLM in Fig. 1.5 (b). The fitted results of $R_{i,CCL}$, R_{PEM}, and C_{dl} are shown in Fig. 3.18. In Fig. 3.18 (a), ionic resistances of cathode CL was decreased with increase of PFSI content because PFSI is ionic conductor. $R_{i,CCL}$ and R_{PEM} were decreased for all of the activate MEAs as shown in Fig. 3.18 (a) and (b), respectively. It would be due to increased hydration of Nafion and PFSI after activation.[82] Until a few years ago, Schroeder's paradox of Nafion had been reported. Schroeder's paradox is that the water content (λ) of liquid equilibrated Nafion is 22 $mol_{H2O}\ mol_{SO3^-}^{-1}$ and that of vapor equilibrated Nafion is 14

mol_{H2O} mol_{SO3-}^{-1}.[17,79,94-98] However L. M. Onishi et al. showed the absence of Schroeder's paradox at 2007. They showed that thermal history of the Nafion is strongly related with water content, and the preboiled Nafion water content in conductivity experiments changed slightly with increasing temperature, but the predried Nafion water content rose dramatically with temperature.[17] In this study, predried Nafion membrane was used, and CCM was predried after spray deposition of CL. Moreover activation was carried out at 70°C with fully humidified condition. Therefore the decrease of $R_{i,CCL}$ and R_{PEM} would be due to the increased water content in Nafion membrane and PFSI. $R_{i,CCL} \times R_{PEM}^{-1}$ that is normalized $R_{i,CCL}$ by R_{PEM} to remove the increased water content was shown in Fig. 3.18 (c). The change of normalized $R_{i,CCL}$ was very small, and it means that the change of ionic resistance in CL after activation is due to the change of hydration. C_{dl} of cathode CL was also decreased after activation as shown in Fig. 3.18 (d). It means that accessible electrode surface was decreased after activation. However ECSA decrease was only caused by the Pt particle growth, and the decrease of ECSA by the decrease of accessible electrode surface area was not shown. Therefore decrease of the C_{dl} would be related with decreased area of carbon surface that proton and electron can be reached to.
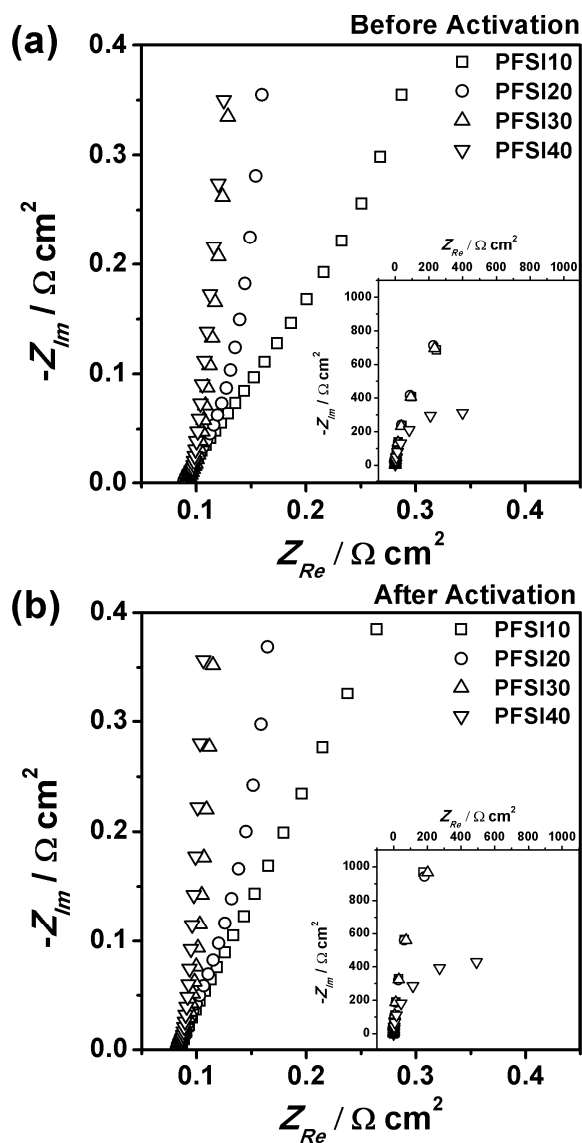
Figure 3.17. Nyquist plots of non-faradaic EIS for cathode CLs of (a) as-prepared and (b) activated MEAs.
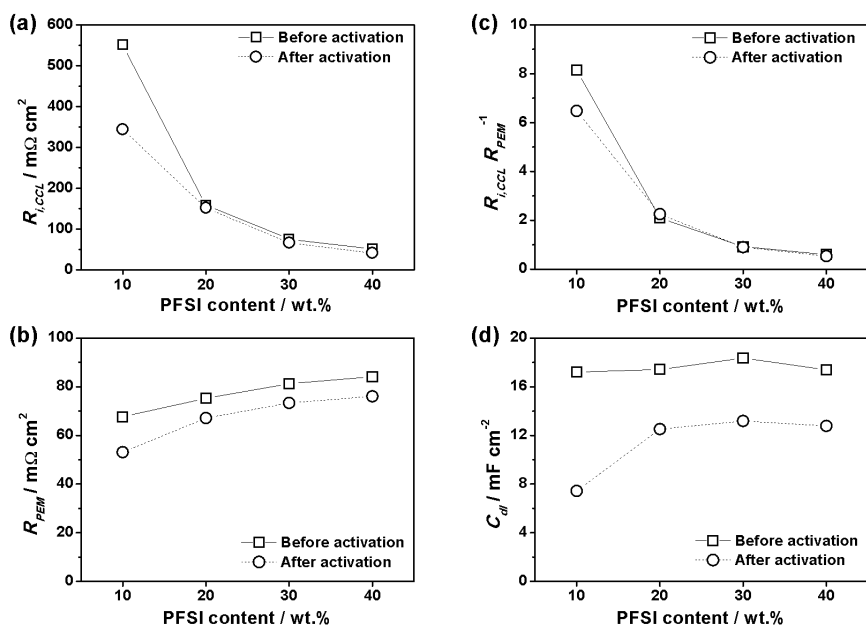
Figure 3.18. The fitted results of non-faradaic EIS results in Fig. 3.17; (a) $R_{i,CCL}$, (b) R_{PEM}, (c) $R_{i,CCL}/R_{PEM}$, and (d) C_{dl}.

3.2.5 Analysis of Faradaic EIS and Degree of Activation

EIS results of as-prepared and activated MEAs at 0.7 V with H_2/air reactants are shown in Fig. 3.19 (a) and (b), respectively. Loop resistances of impedances are shown in Fig. 3.19 (c). In both cases, loop resistance was decreased with increase of PFSI content in cathode CL. However loop resistance of PFSI40 was larger than that of PFSI30 before and after activation. High loop resistance at 0.7 V would arouse low performance at high voltage region of polarization test. There is optimum content of PFSI in cathode CL, and many researchers suggest that the optimum content is about 30 wt.% versus catalyst weight.[99-103] O_2 diffusion problem in the agglomerates would be occurred by high content of PFSI. M. Lee et al. said that this gas diffusion problem occurred for high PFSI content due to the gas being forced to diffuse either through ticker PFSI films or water-filled channels, so that the intrinsic limiting mass transport behavior of air in narrow channels, due to the back-diffusion of N_2, would become more severe.[40,104,105] In Fig. 3.19 (c), activation ratio using loop resistance of EIS result was estimated by $1-(R_{loop,Aft.} / R_{loop,Bef.})$. Activation ratio using EIS was decreased with increasing of PFSI content in cathode CL. Because loop resistances of activated MEAs are the minimum resistances measured at optimized state, activation ratio using EIS is influenced by the MEA performance of as-prepared MEA. Therefore low activation ratio means that the resistance of as-prepared MEA is relatively low, in other words, as-prepared MEA has relatively high performance. Furthermore it means that

the effect of PFSI content on the performance of as-prepared MEA is higher than that of activated MEA.

3.2.6 Analysis of Polarization Curve and Degree of Activation

The polarization curves of as-prepared and activated MEAs with H_2/O_2 reactants are shown in Fig. 3.20 (a) and (b), respectively. In polarization test, performance enhancement was observed after activation and the trend of polarization curves is along with the EIS results. The optimized PFSI content in cathode CL was 30 wt.%, and the performance of PFSI30 was highest in both cases of as-prepared and activated MEAs. Although performance of PFSI40 was higher than that of PFSI20 before activation, performance of PFSI40 was lower than that of PFSI20 after activation. It was caused by low activation ratio for PFSI40 as shown in Fig. 3.19 (c).

In general, current density at 0.6 V in polarization curve is used as a representative performance of MEA. Therefore current densities of polarization curve at 0.6 V for as-prepared and activated MEAs are shown in Fig. 3.21 (a). $i_{0.6V}$ was increased with increase of PFSI content in cathode CL and 30 wt.% was optimized content. As stated earlier, diffusion problem in agglomerates would be occurred by high PFSI content, and it caused low $i_{0.6V}$ of PFSI40. In Fig. 3.21 (b), activation ratio and value using IV were estimated by $1-(\,i_{0.6V,Bef.}\,/\,i_{0.6V,Aft.}\,)$ and $i_{0.6V,Aft.} - i_{0.6V,Bef.}$, respectively. Activation ratio and value using IV were also decreased with increasing of PFSI content in cathode CL.

This result is similar to the result of activation ratio using EIS in Fig. 3.19 (c) although the cell voltage and oxygen concentration in cathode supplement was different. Change of open circuit voltages (OCVs) are shown in Fig. 3.21 (c). OCV was increased after activation for all of the MEAs, and the trend of OCV increase was also similar to the trend of degree of activation. V. B. Silva et al. reported OCV increment after activation.[81] They showed that the OCV was increased during activation cycles although hydrogen crossover at open circuit was increased along the activation procedure because overvoltage of ORR was decreased caused by the reduced mixed potential effect. After activation, OCVs of MEAs had similar values except PFSI40. As shown in CV and non-faradaic EIS, small size of scratch or pinhole would be present on PEM of PFSI40. Therefore the amount of hydrogen crossover in PFSI40 would be higher than that in other MEAs, and it results low OCV for PFSI40.

In this study, interaction between Pt and sulfonate anion in PFSI became strong with increase of PFSI content before activation, and this interaction was disappeared after activation. Markovic et al. reported the relationship between anion adsorption and ORR kinetics on Pt crystal faces.[40,101] They showed that the variation in activity at 0.8 to 0.9 V is relatively small between the three low index faces, with activity increasing in the order (100) < (110) ≈(111) in perchloric acid. However in sulfuric acid, the variations in activity with crystal face were much larger, with the difference between the most active and the least active being about two orders of magnitude, and

increased in the opposite order (111)<<(100)<(110).[101] It is due to the anion adsorption on Pt(111). Because sulfate anion in sulfuric acid electrolyte and sulfonate anion in PFSI have tetrahedral structure, they easily adsorb on Pt(111), and this anion adsorption interrupts the ORR kinetics. Therefore from the viewpoint of catalytic activity, degree of activation should be increased with increase of PFSI content because increase of PFSI content caused high interaction between Pt and sulfonate anion in PFSI. However degree of activation that was estimated by EIS or IV curve was decreased with increase of PFSI content. These conflicting results mean that the portion of catalyst activation on MEA activation is small, and other crucial factor would be exist. The crucial factor would be increased water content of Nafion and PFSI. Therefore more study such as activation test after pretreatment of CCM to make maximum hydration state would be useful to confirm the hydration effect on activation.
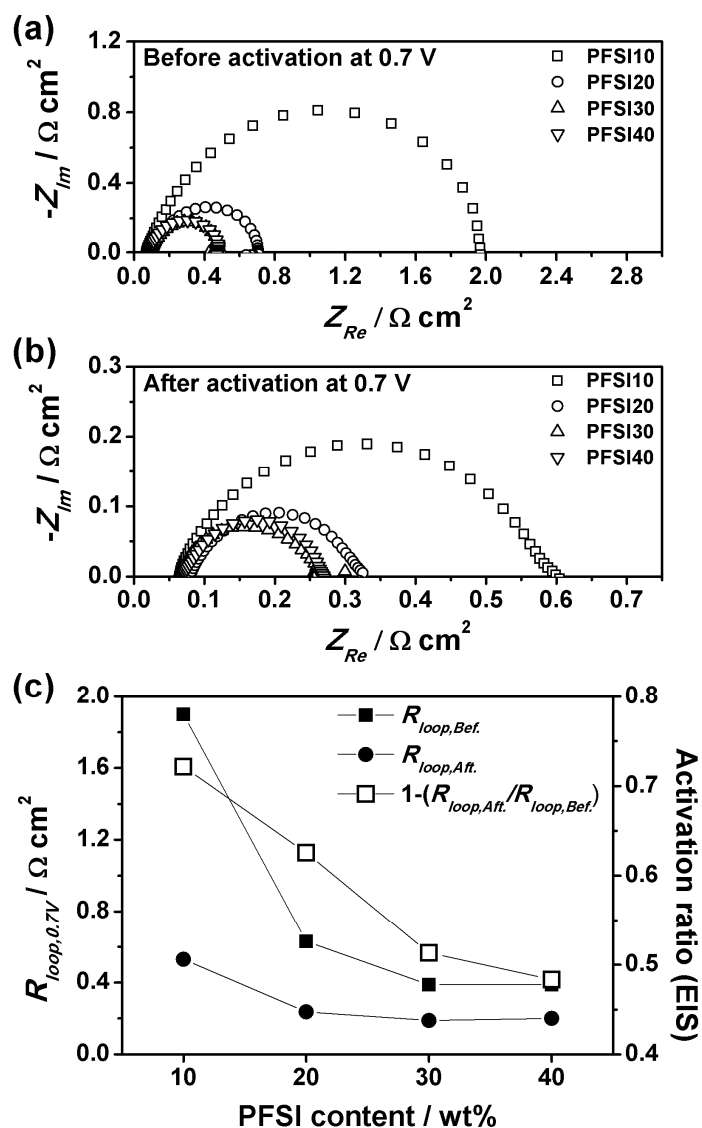
Figure 3.19. EIS Nyquist plots of (a) as-prepared and (b) activated MEAs at 0.7 V with H₂/air reactants. (c) Estimated activation ratio and loop resistances by using the results in (a) and (b).
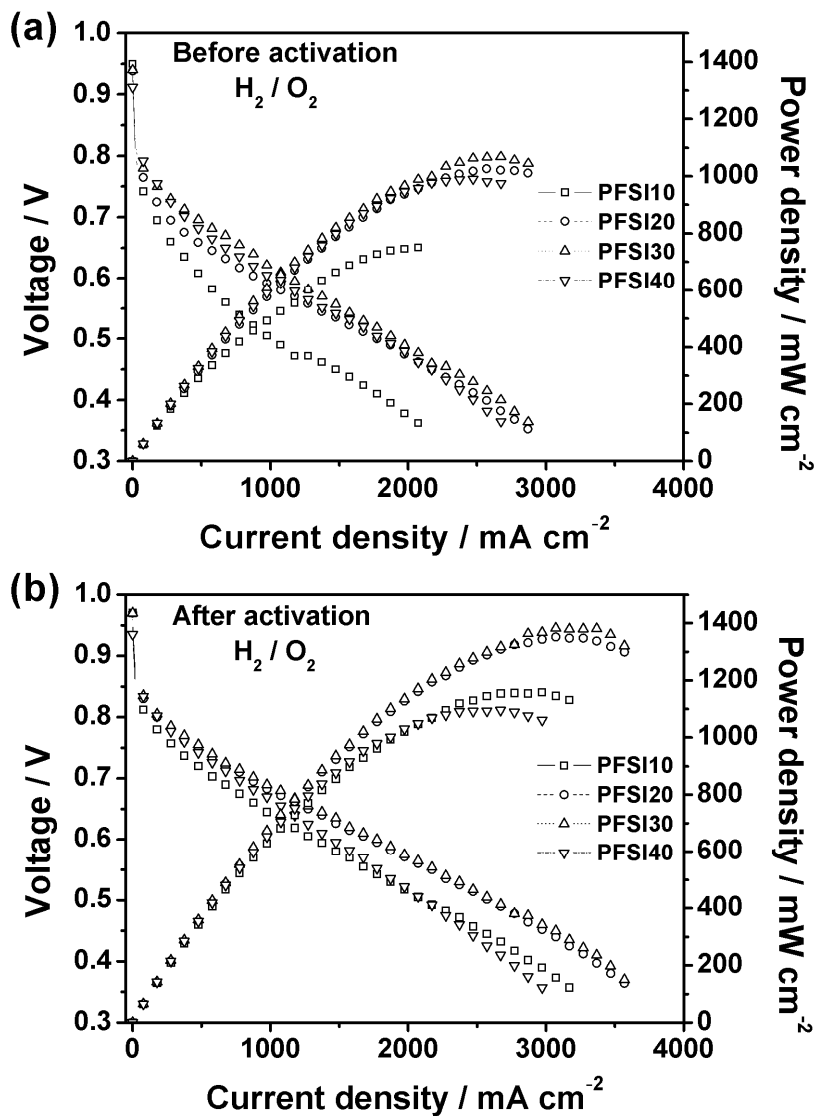
Figure 3.20. The polarization curves of (a) as-prepared and (b) activated MEAs with H₂/O₂ reactants.

(a) Before activation H_2 / O_2 — PFSI10, PFSI20, PFSI30, PFSI40

(b) After activation H_2 / O_2 — PFSI10, PFSI20, PFSI30, PFSI40

Axes: Voltage / V, Current density / mA cm^{-2}, Power density / mW cm^{-2}
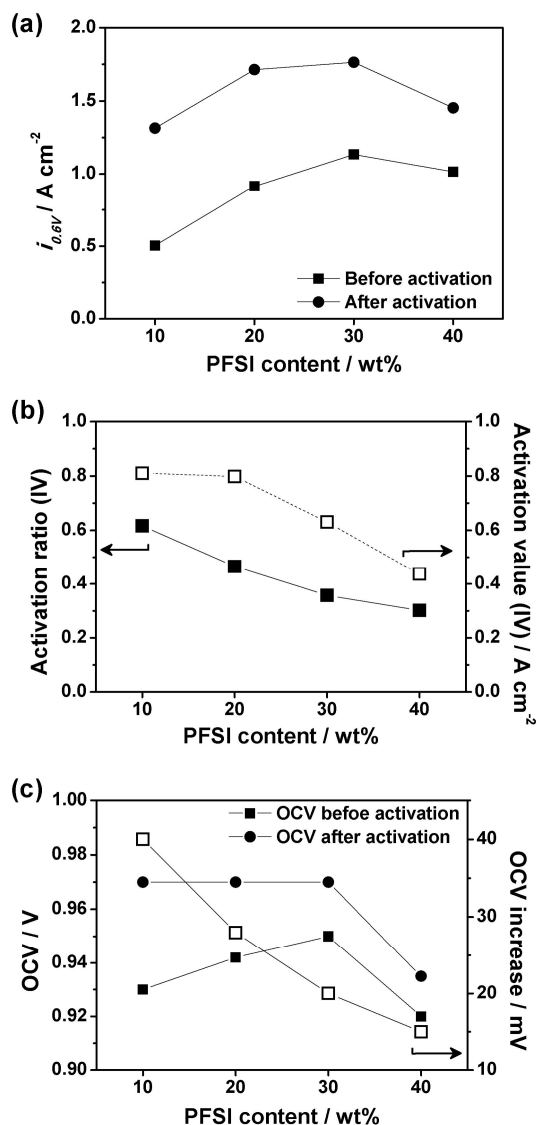
Figure 3.21. Current densities of polarization curves in Fig. 3.20 at 0.6 V ($i_{0.6V}$) for (a) as-prepared and activated MEAs. (b) Estimated activation ratio and value by using the results in (a). (c) Ratio and value of OCV variation after activation.

3.3 Interface study

3.3.1 Cyclic Voltammetry and ECSA

The thickness of PFSI film on CL would be estimated from the information about typical thickness (50.8 μm) and basis weight (100 g m^{-2}) of NR212 membrane.[64] Estimated film thicknesses of 0.1 and 0.35 mg cm^{-2} PFSI are 0.51 and 1.78 μm, respectively. Because some of the deposited PFSI would penetrate into CL, actual thickness of PFSI film would be lower than these values.

Cyclic voltammograms of cathode CLs for MEAs those were not hot-pressed are shown in Fig. 3.22. The shapes of CVs in Fig. 3.22 (a) were similar to that in Fig. 3.13 (c) because CL deposition method (spray) was same and they were non hot-pressed MEAs. Therefore CLs of PFSI30, IF00, IF10, and IF35 have same composition, however interfacial resistance between PEM and CL would be different because of the different adhesional method. In Fig. 3.22, shape of CVs were changed after activation especially OH$^-$ adsorption and desorption region. OH$^-$ adsorption peaks were shifted to negative potential, and OH$^-$ desorption peaks were increased because the areas of OH$^-$ adsorption peaks were increased after activation.
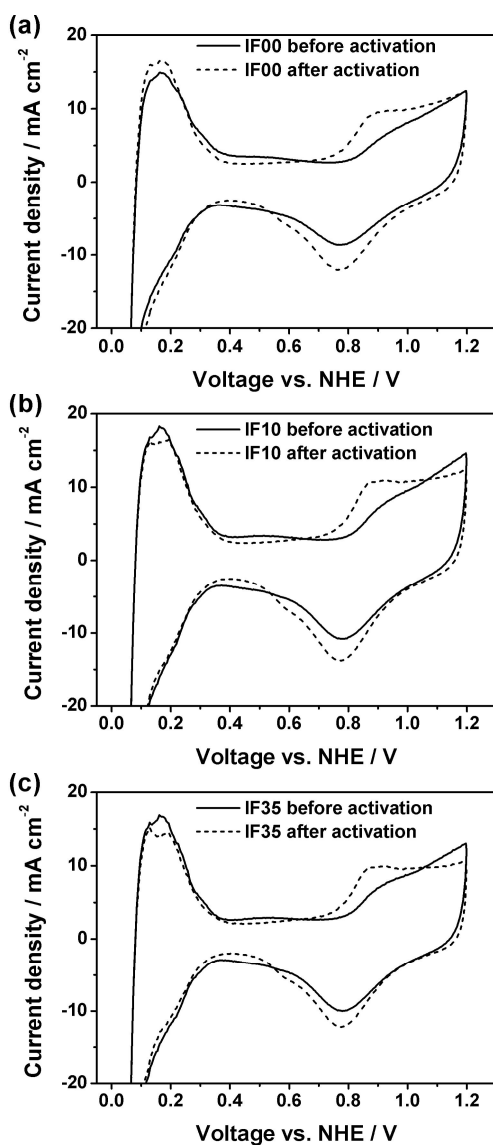
Figure 3.22. CVs of cathode CLs for non hot-pressed MEAs; (a) IF00, (b) IF10, and (c) IF35.

CVs of cathode CLs of hot-pressed MEAs are shown in Fig. 3.23. Differences of double layer thickness in Fig. 3.23 were small comparing to Fig. 3.22. Moreover other shape changes of CV such as top of hydrogen desorption peak at 0.18 V, onset potential of OH$^-$ adsorption peak, and the charge of Pt reduction peak, became small for hot-pressed MEAs. Therefore hot-pressing process would affect to the interaction between Pt(111) and sulfonate anion before activation. Re-construction and re-distribution of PFSI in CL would occur during hot-pressing because hot-pressing temperature (130°C) was higher than T_g of Nafion (ca. 120°C). Arrangement of PFSI and Pt would be changed during hot-pressing and changed arrangement of sulfonate anion and Pt would affect to the interaction between Pt(111) and sulfonate anion.

ECSAs of CVs in Fig. 3.22 and Fig. 3.23 are shown in Fig. 3.24 (a) and (b), respectively. ECSA of IF00 was increased and that of IF10 was not changed after activation. ECSAs of the others were decreased after activation. The increase of ECSAs for IF00 would be caused by the unstable interface between CL and PEM before activation. Some of the CL that was not connected to PEM would exist before activation, and highly hydrated IF00 after activation would extend the ion-conductive surface area. Unlike IF00, ECSA of IF00HP was increased after activation. It means that hot-pressing would stabilize the interface and extend the ion-conductive surface area. In Fig. 3.24, ECSA values of non hot-pressed and as-prepared MEAs were increased with increase of PFSI film thickness, and ECSA values of hot-pressed or

activated MEAs were not related with PFSI film thickness. However ECSA decreasing ratio was increased with increase of PFSI film thickness. It would be due to high ECSA of as-prepared MEAs, and it was caused by high interface area when PFSI film was thick. ECSA decreasing ratio of hot-pressed MEAs were also increased with increase of PFSI thickness and that of IF35HP (8.5%) was similar to that of PFSI30 (8.0%). The interfacial stability of IF35HP would be similar to that of PFSI30, and the reason of ECSA decrement after activation would be due to increase of Pt particle size. Hot-pressing process and thick PFSI film would enhance the stability of CL and PEM interface.
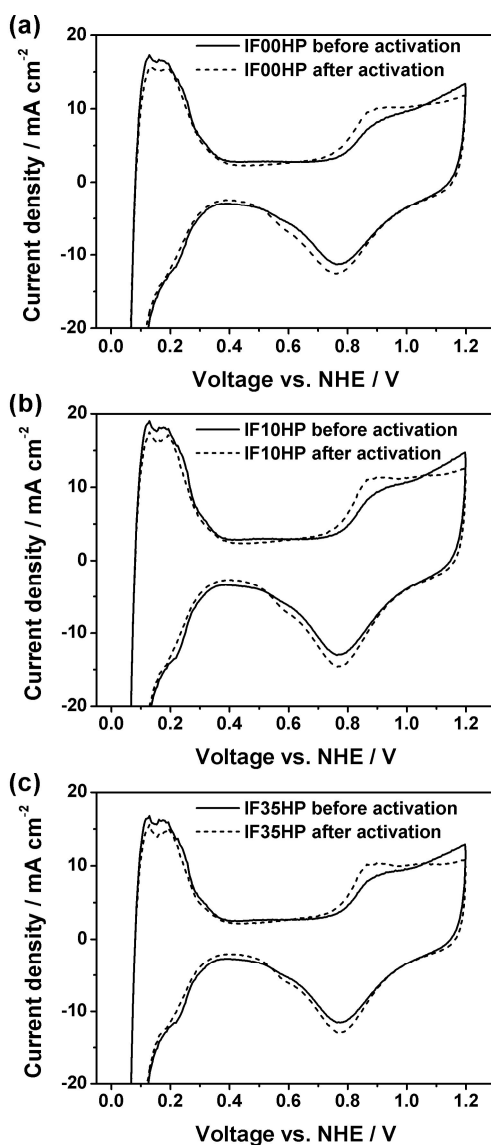
Figure 3.23. CVs of cathode CLs for hot-pressed MEAs; (a) IF00HP, (b) IF10HP, and (c) IF35HP.
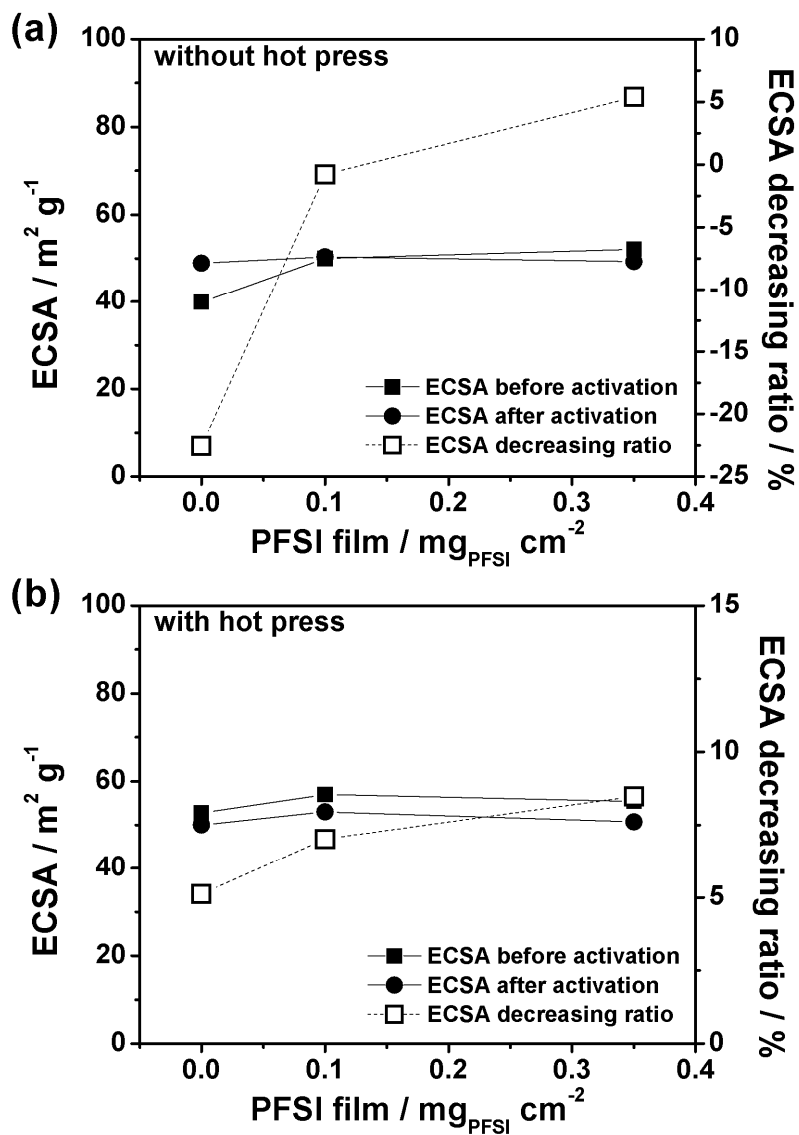
Figure 3.24. ECSAs and ECSA decreasing ratios of (a) non hot-pressed and (b) hot-pressed MEAs.

3.3.2 Analysis of Normalized Cyclic Voltammetry

Differences of normalized current density $\Delta(i \times Q_H^{-1})$ of non hot-pressed and hot-pressed MEAs were shown in Fig. 3.25 (a) and (b), respectively. Hot-pressed MEAs showed larger $\Delta(i \times Q_H^{-1})$ peak at OAD region than non hot-pressed MEAs. It was expected results from the discussions of Fig. 3.22 and Fig. 3.23. Especially $\Delta(i \times Q_H^{-1})$ intensity under 0.55 V was very low. It means that CV shapes of hot-pressed MEAs under HAD and double layer region were not changed during activation. The change of HQ-Q redox couple at 0.6 V was not shown in Fig. 3.25 (a) and (b) irrelevant to activation and hot-pressing process because the ratio of exposed carbon surfaces were not change. $\Delta(i \times Q_H^{-1})$ at HAD and double layer regions were magnified and plotted in Fig. 3.26. $\Delta(i \times Q_H^{-1})$ of non hot-pressed MEAs in Fig. 3.26 (a) was similar to the plot in Fig. 3.15 (a). The hydrogen desorption peak at 0.165 V was outstanding and it means strong interaction between sulfonate anion and Pt(111) surface before activation. However hydrogen desorption peak at 0.165 V was smaller than that at 0.240 V for hot-pressed MEAs in Fig. 3.26 (b). Sulfonate anion adsorption peak of hot-pressed MEAs in Fig. 3.26 (c) was also smaller than that of non hot-pressed MEAs in Fig. 3.26 (d). Decrease of 0.165 V and 0.490 V peaks for hot-pressed MEAs means that hot-pressing process weakened the interaction between Pt(111) surface and sulfonate anion in PFSI. In Fig. 3.27, $i \times Q_H^{-1}$ differences of non hot-pressed and hot-pressed MEAs, $(i \times Q_H^{-1})_{nonHP} - (i \times Q_H^{-1})_{HP}$, are shown. Before activation, difference of CV

shapes between non hot-pressed and hot-pressed MEAs was large as shown in Fig. 3.27 (a). However CV shapes after activation were almost same irrelevant to hot-pressing process as shown in Fig. 3.27 (b). As shown in Fig. 3.24 and Fig. 3.27 (b), ECSAs and CV shapes were almost same irrelevant to hot-pressing process. It means that cathode CLs would have similar state irrelevant to hot-pressing process if the CL compositions are same.
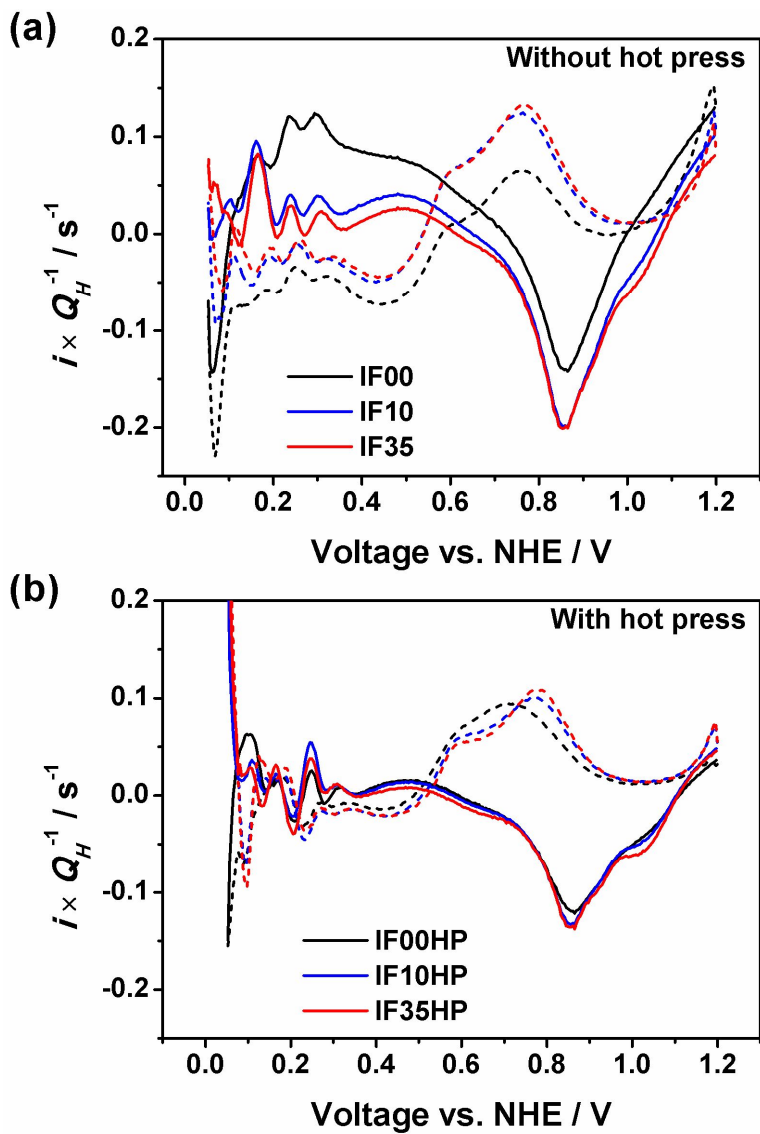
Figure 3.25. $(i \times Q_H^{-1})_{before} - (i \times Q_H^{-1})_{after}$ of cathode CLs for (a) non hot-pressed and (b) hot-pressed MEAs. Forward sweeps (lines) and backward sweeps (dashes).
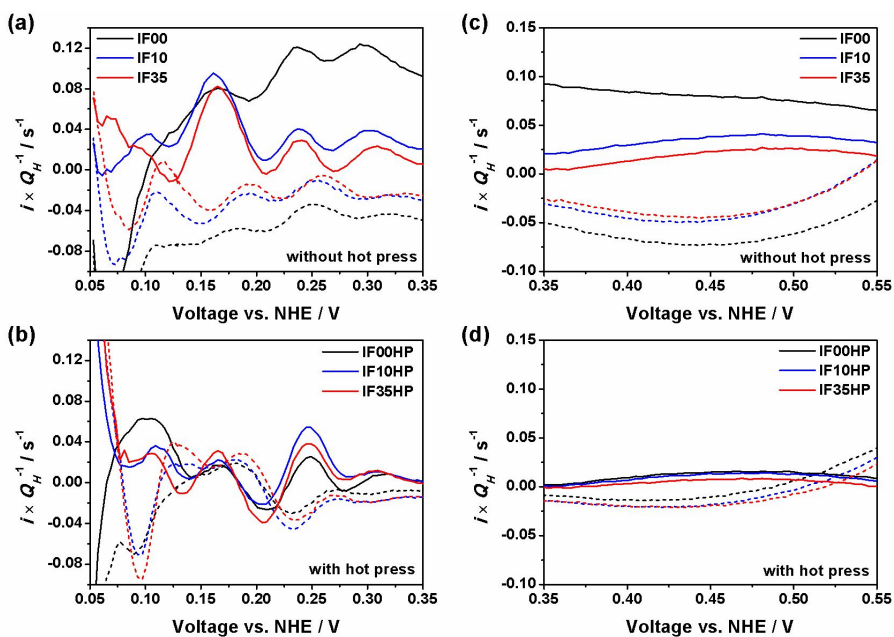
Figure 3.26. Magnified plots of CVs in Fig. 3.25; HAD region of (a) non hot-pressed and (b) hot-pressed MEAs, and DL region of (c) non hot-pressed and (d) hot-pressed MEAs. Forward sweeps (lines) and backward sweeps (dashes).
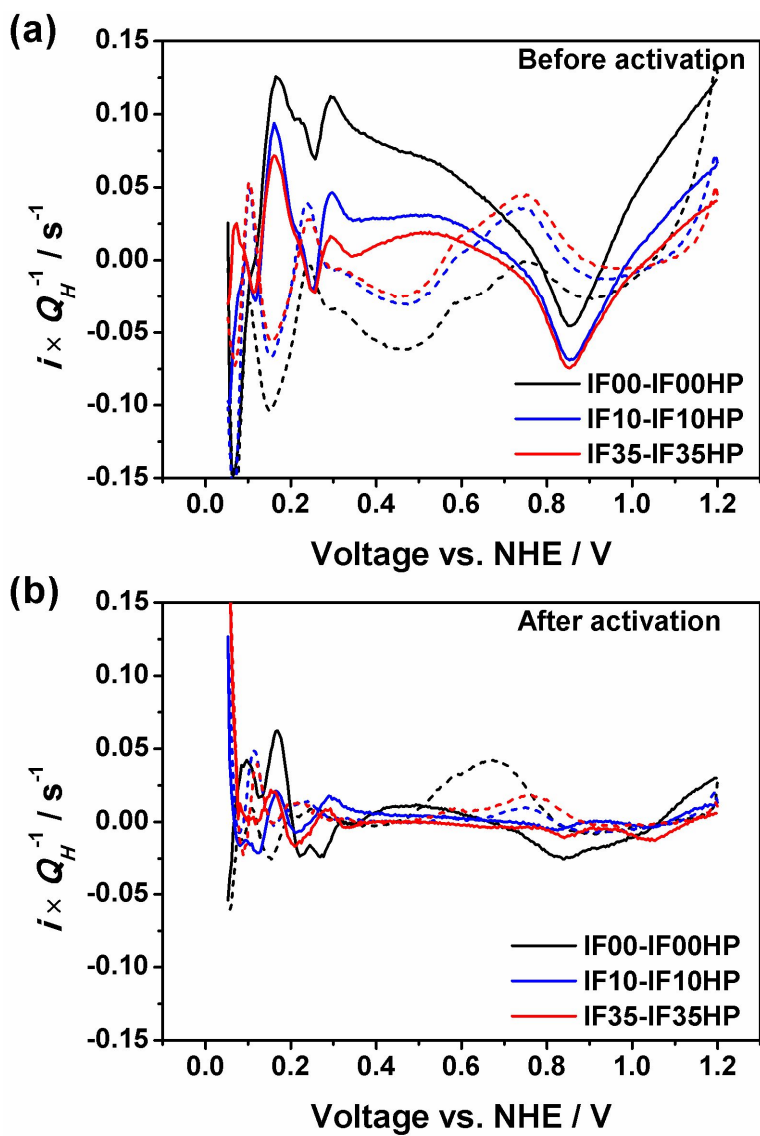
Figure 3.27. $(i \times Q_H^{-1})_{NonHP} - (i \times Q_H^{-1})_{HP}$ of cathode CLs of (a) as-prepared and (b) activated MEAs. Forward sweeps (lines) and backward sweeps (dashes).

3.3.3 Analysis of Non-Faradaic EIS

Nyquist plots of non-faradaic EIS results are shown in Fig. 3.28. Limiting values of Z_{Re} at low frequency that is proportional to ionic resistance was decreased with increase of PFSI film thickness.[48,50] High loading of PFSI film on CL would extend the interface area, and it would cause decrease of limiting Z_{Re} value. In the case of IF00HP, limiting value of Z_{Re} was increased after activation. The CL and PEM of IF00HP might be damaged after activation because the roughness of CL surface was high and the interface would be very unstable.

The non-faradaic EIS results in Fig. 3.28 were fitted by using modified TLM in Fig. 1.5 (b), and the estimated electrochemical properties such as $R_{i,CCL}$, R_{PEM}, and C_{dl} are shown in Fig. 3.29. In this study, there were three variables to compare the effect on electrochemical properties; activation of MEA (as-prepared and activated MEA), hot-pressing (non hot-pressed and hot-pressed MEA), and thickness of PFSI film (0.00, 0.10, and 0.35 mg$_{PFSI}$ cm^{-2}). $R_{i,CCL}$ changes of non hot-pressed and hot-pressed MEAs during activation were shown in Fig. 3.29 (a) and (d), respectively. $R_{i,CCL}$ values were decreased with increase of PFSI film thickness regardless hot-pressing and activation. It would be due to increase of interface area with increase of PFSI film thickness. In most cases, $R_{i,CCL}$ values were decreased after activation except for IF00HP. $R_{i,CCL}$ increase of IF00HP after activation would be due to interfacial damage as stated earlier. Increase of $R_{i,CCL}$ after activation for MEA made by CCM method was also shown in

95

previous activation study, and it would be caused by increase of PFSI hydration in cathode CL. R_{PEM} changes are shown in Fig. 3.29 (b) and (e). The increase of PEM thickness was smaller than 2 μm, and it was < 5% of the PEM thickness. Therefore R_{PEM} were irrelevant to thickness of PFSI film though the membrane thickness was increased. Moreover R_{PEM} was also decreased after activation, and this result was same with the result in activation study. R_{PEM} decrease after activation would be due to increased hydration of PEM after activation. Estimated C_{dl} values are shown in Fig. 3.29 (c) and (f). C_{dl} values were not changed with increase of PFSI film thickness, and hot-pressing process was also not affected to C_{dl}. In general, C_{dl} is proportional to the electrode surface area that proton and electron can be reached, and this area would not change with increase of PFSI film thickness. The irrelevance of C_{dl} and PFSI film thickness is parallel to the irrelevance of ECSA and PFSI film thickness as shown in Fig. 3.24. C_{dl} was decreased after activation, and this result was also same with the result in activation study. As stated earlier in activation study, decrease of C_{dl} after activation would be caused by decrease of carbon surface that proton and electron can be reached to. C_{dl} of IF00 was not increased but decreased after activation. ECSA of as-prepared IF00 was small because of the unstable interface, and the unstable interface caused low C_{dl} value of as-prepared IF00.
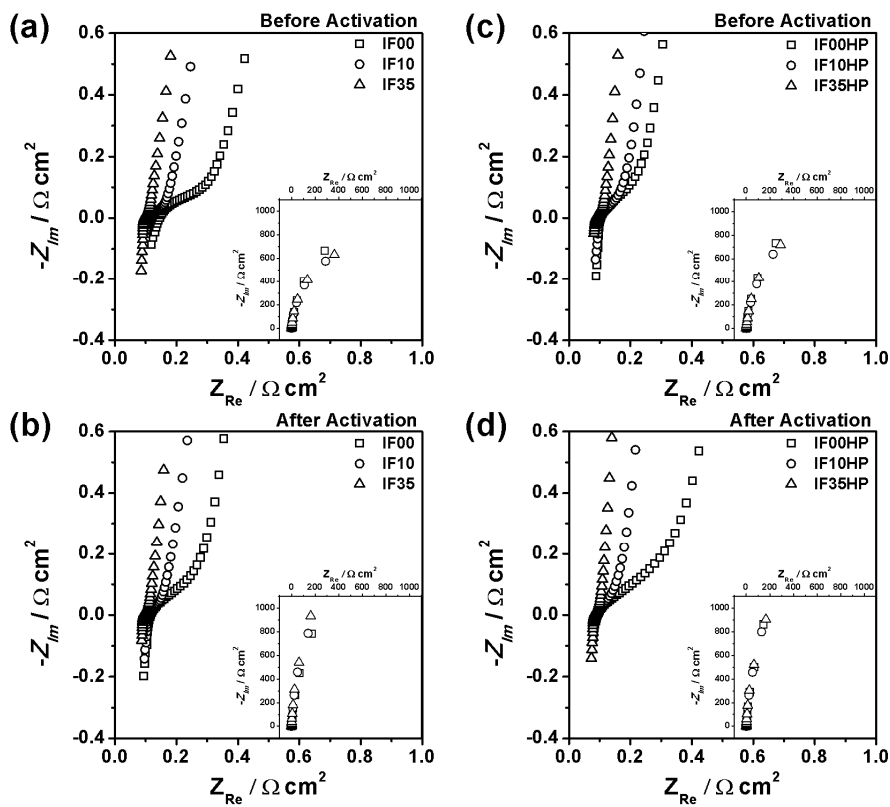
Figure 3.28. Nyquist plots of non-faradaic EIS results with H_2/N_2 feed; (a) as-prepared and (b) activated MEAs without hot-pressing, and (c) as-prepared and (d) activated MEAs with hot-pressing.
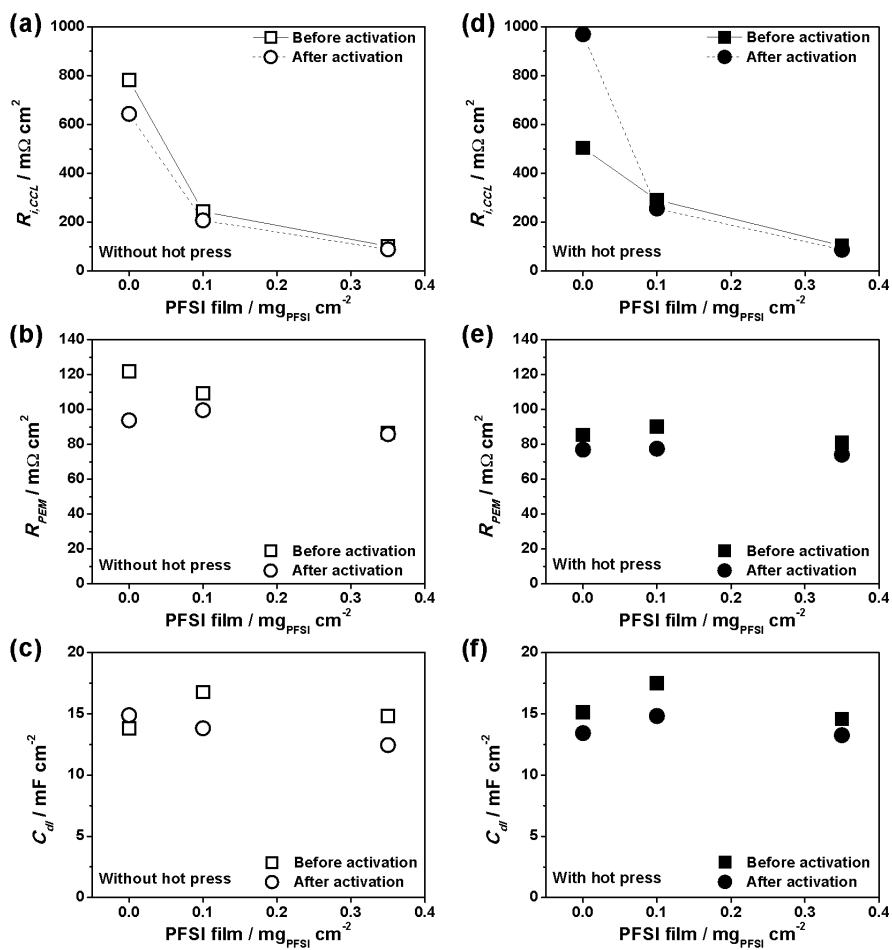
Figure 3.29. The fitted results of non-faradaic EIS results in Fig. 3.28; (a) $R_{i,CCL}$, (b) R_{PEM}, and (c) C_{dl} of non hot-pressed MEAs and (d) $R_{i,CCL}$, (e) R_{PEM}, and (f) C_{dl} of hot-pressed MEAs.

R_{PEM} plots those were shown in Fig. 3.29 (b) and (e) were hard to know the relationship between R_{PEM} and hot-pressing. Therefore R_{PEM} was re-plotted in Fig. 3.30 (a) and (b). In both cases of as-prepared and activated MEAs, R_{PEM} of hot-pressed MEAs were larger than that of non hot-pressed MEAs. However in literature, ionic conductivity of Nafion was decreased after hot-pressing.[106] The structure of Nafion membrane would be the model of ionic clusters with spherical shape of micelle structure.[107,108] Han et al. showed why Nafion conductivity was decreased after hot-pressing by using ^{1}H NMR.[109] They said that hot-pressing mainly reduced the sizes and number of the big pores, and it caused the reduction of water uptake and proton conductivity after hot-pressing.[109] Therefore in this study, ionic resistance of PEM would be decreased after activation. The decrease of R_{PEM} after hot-pressing would be due to the enhancement of interfacial stability and ionic path continuity between PEM and PFSI film. The relationships between electrochemical properties (R_{PEM}, $R_{i,CCL}$, and C_{dl}) and experimental conditions (activation, hot-pressing, and PFSI film thickness) were summarized in Table 4.
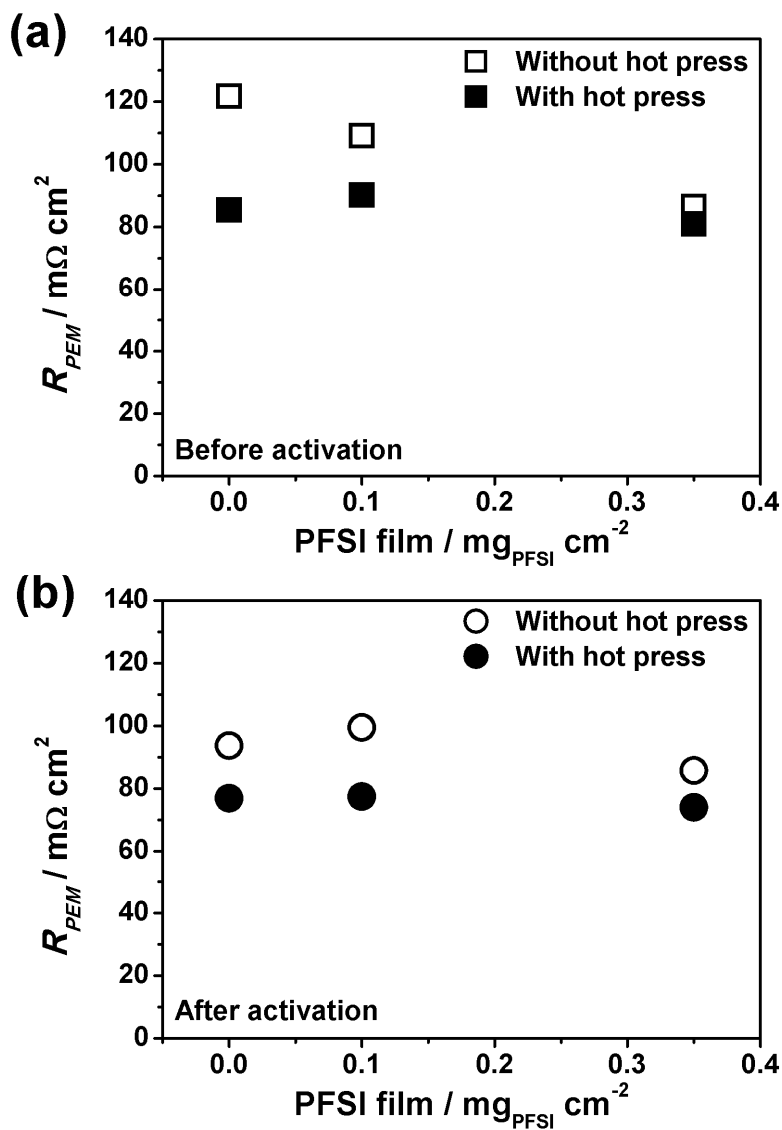
Figure 3.30. The fitted R_{PEM} values of non-faradaic EIS results for (a) as-prepared and (b) activated MEAs.

Table 4. The relationship between electrochemical properties (R_{PEM}, $R_{i,CCL}$, and C_{dl}) and experimental conditions

Electrochemical property	Activation	Hot-pressing	Thick PFSI film
R_{PEM}	Decrease	Decrease	Irrelevance
$R_{i,CCL}$	Decrease	Irrelevance	Decrease
C_{dl}	Decrease	Irrelevance	Irrelevance

3.3.4 MEA Performances and Degree of Activation

Polarization curves of non hot-pressed and hot-pressed MEAs are shown in Fig. 3.31. These polarization curves were measured with H_2/air reactants after activation. MEA performances were increased with increase of PFSI film thickness in both cases. As stated earlier, increase of PFSI film thickness caused increase of interface area, and $R_{i,CCL}$ were decreased dramatically. Therefore in Fig. 3.31, great influence of interface area on MEA performance would be confirmed. Moreover the performances of hot-pressed MEAs in Fig. 3.31 (b) were higher than that of non hot-pressed MEAs in Fig. 3.31 (a). Hot-pressing was related to interface stability between PFSI film and PEM, and unstable interface caused large R_{PEM}. Therefore crucial effect of interface stability on MEA performance was also confirmed in Fig. 3.31. The difference of performances between IF10HP and IF35HP was very small in comparison with that between IF10 and IF35. Therefore I can conclude that hot-pressing would minimize the use of PFSI film for high performance. In spite of relatively low current density, current densities of non hot-pressed MEAs at high current region were decreased rapidly (so-called high concentration overpotential) in comparison with hot-pressed MEAs. It would be due to bad water management in cathode CL that was caused by unstable interface of non hot-pressed MEAs.
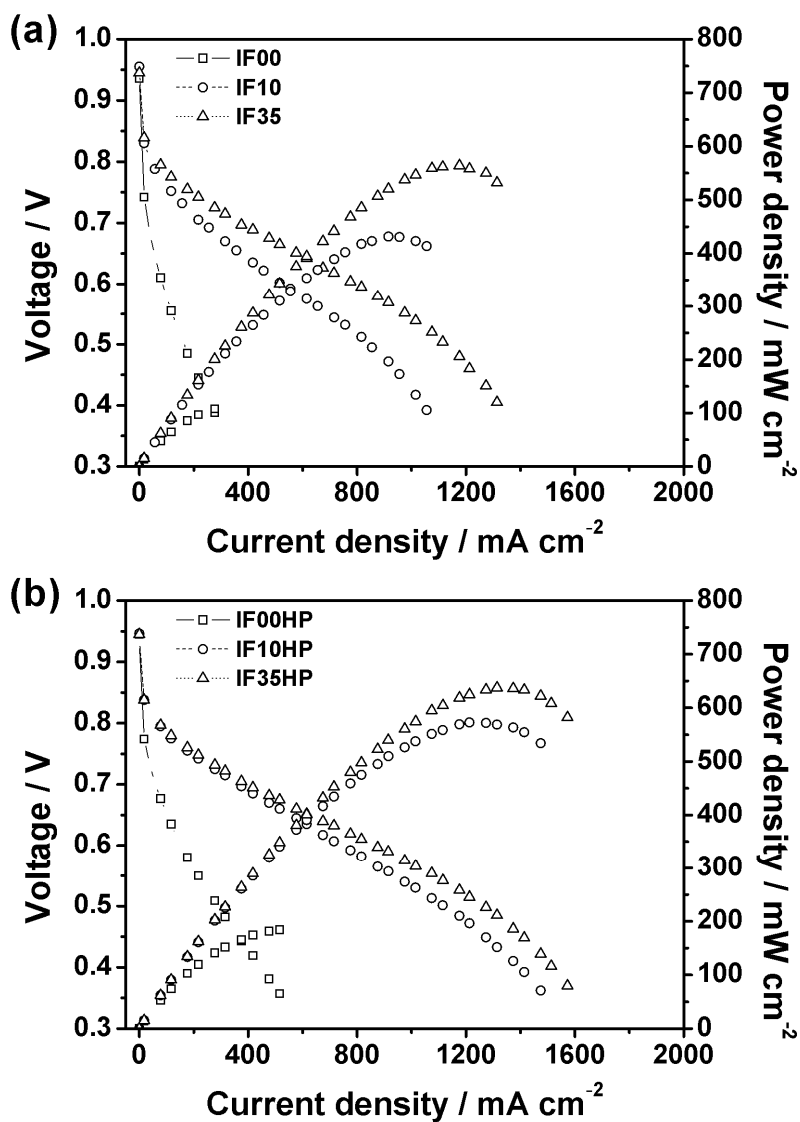
Figure 3.31. Polarization curves of (a) non hot-pressed and (b) hot-pressed MEAs after activation with H₂/air reactants.

The current densities of polarization curves with H_2/O_2 reactants at 0.6 V before and after activation are shown in Fig. 3.32 (a). Performance enhancement was observed after activation in both cases of non hot-pressed and hot-pressed MEAs. Degree of activations such as activation ratio and value using IV curve are shown in Fig. 3.32 (b) and (c), respectively. In Fig. 3.32 (b), activation ratio was decreased with increase of PFSI film thickness, and activation ratios of non hot-pressed MEAs were higher than those of hot-pressed MEAs. Because low activation ratio means high performance of as-prepared MEA, hot-pressed MEAs showed higher performance than non hot-pressed MEAs. Stable interface by hot-pressing and high interface area by thick PFSI film would cause high performance of as-prepared MEAs. Low interaction between Pt and sulfonate anion for hot-pressed MEAs would also cause high performance of as-prepared MEAs. Tendency of activation ratio change with PFSI film thickness in Fig. 3.32 (b) was similar to that with PFSI content in cathode CL as shown in Fig. 3.21 (b). However activation value using IV curves in Fig. 3.32 (c) were increased with increase of PFSI film thickness. Tendency of activation value change with PFSI film thickness were contrary to that with PFSI content in cathode CL in Fig. 3.21 (b). It would be due to low performance of activated MEAs that had bad interface stability and small interface area.
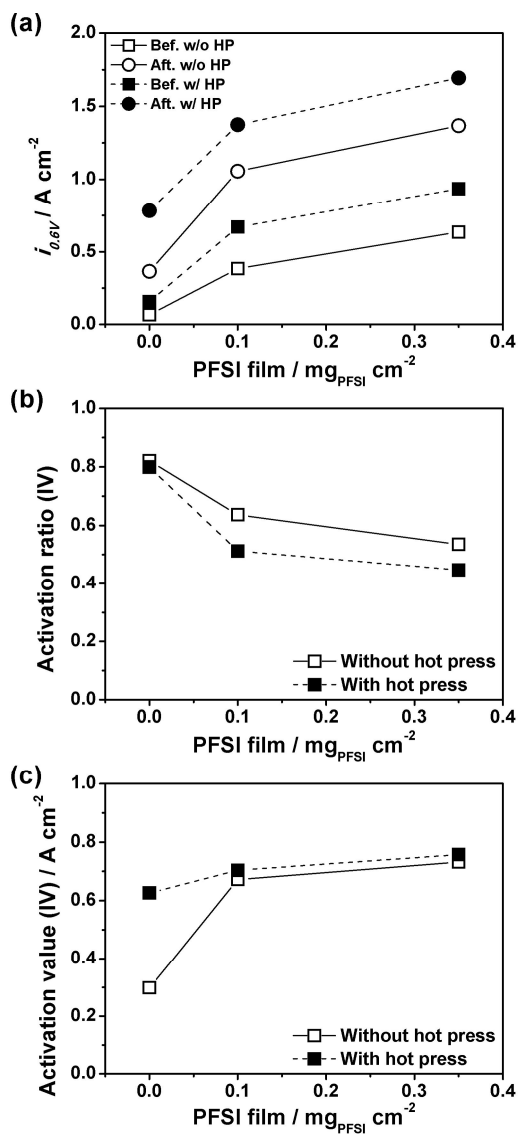
Figure 3.32. (a) Current densities of polarization curves with H$_2$/O$_2$ reactants at 0.6 V ($i_{0.6V}$). (b) Estimated activation ratios and (c) activation values using $i_{0.6V}$.

Nyquist plots of faradaic EIS results with H_2/air reactants after activation at 0.7 and 0.5 V were shown in Fig. 3.33. High frequency resistances of non hot-pressed MEAs were higher than that of hot-pressed MEAs in all of EIS results in Fig. 3.33. This result was consistent with the R_{PEM} results those were measured by non-faradaic EIS. Loop resistances of non hot-pressed MEAs at 0.7 V were larger than that of hot-pressed MEAs. It would be due to unstable interface between PFSI film and PEM. In Fig. 3.33 (c), loop resistances of IF35 and IF35HP were similar, and high frequency resistances of them were different. It means that 0.35 mg_{PFSI} cm^{-2} would be enough to minimize the roughness differences between PFSI film and PEM. However loop resistances of IF35 and IF35HP at 0.5 V showed significant gap. It would be due to high current density and bad water management at the unstable interface.
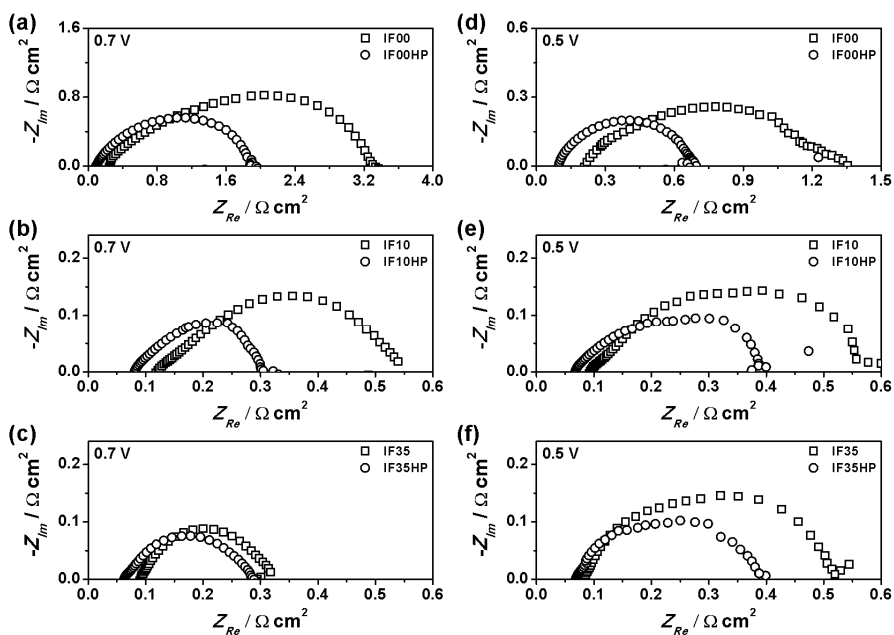
Figure 3.33. EIS Nyquist plots of MEAs with (a) 0, (b) 0.1, and (a) 0.35 mg$_{PFSI}$ cm^{-2} of PFSI film at 0.7 V, and with (d) 0, (e) 0.1, and (f) 0.35 mg$_{PFSI}$ cm^{-2} of PFSI film at 0.5 V.

Chapter 4. Conclusions

The increased ionic resistance with increased thickness of the cathode CL was estimated and the effect of the increased ionic resistance on MEA performance was evaluated. Using commercial 20, 40, and 60 wt.% Pt/C catalysts as a MEA cathode catalyst, high catalyst loading was a critical factor for realizing high performance in the high voltage region. The Pt/C ratio became a key factor to realize high performance in the low voltage region when catalyst loading was large, because of the thickness of the cathode CL. The increased ionic resistance of the CL was largely responsible for this aspect, particularly when using the 20 wt.% Pt/C. While the 20, 40, and 60 wt.% Pt/C ECSAs were different (67, 61, and 36 m^2 g^{-1}, respectively), U_{Pt} values were similar at approximately 0.60. The modified TLM was designed for easy fitting to estimate C_{dl} and $R_{i,CCL}$. Fitting data were reasonably matched with the experimental results in overall frequency, and C_{dl} and $R_{i,CCL}$ were estimated. The C_{dl} of the cathode CL was linearly proportional to thickness of the cathode CL with a slope of 18 F cm^{-3} regardless of the Pt/C ratio. While $R_{i,CCL}$ was also linearly proportional to the thickness, the intercept was not zero, and the 40 wt.% Pt/C trend line did not correspond with that of the others. The ionic conductivity of the CL was 0.020 S cm^{-1} in the $R_{i,CCL}$ plot, and this value was similar to the state of a Nafion membrane under a 64% relative humidity condition. In faradaic condition, the mass transfer resistance was increased

with the thickness of cathode CL, and double layer capacitance was limited under 25 mF cm^{-2}. The increased thickness of cathode CL caused the increased ionic resistance and mass transfer resistance, and these side effects would limit the performance enhancement.

In activation study, Pt particle size was increased after activation, and it caused decrease of ECSA. The result of ECSA reduction after activation is contrary to the results in literature. It would be due to the optimized experimental condition before activation. Pt utilization efficiency was not changed after activation, and therefore it is hard to say that insulated ionic or electronic pathway to the reaction sites is connected after activation as Z. Qi said.[58] Pt(111) of as-prepared cathode CL those were deposited by spray CCM method were highly interacted with sulfonate anion of PFSI. The interaction was increased with increase of PFSI content in cathode CL, and was disappeared after activation. Therefore ORR activity of Pt for would be increased after activation. $R_{i,CCL}$ was decreased with increase of PFSI because the amount of ionic conductor was increased. $R_{i,CCL}$ R_{PEM} were decreased after activation because Nafion was hydrated after activation. After activation, C_{dl} was also decreased, and it would be due to decreased area of carbon surface that proton and electron can be reached to. However C_{dl} was irrelevant to PFSI content. EIS and polarization results showed that activation ratio and value were decreased with increase of PFSI content in cathode CL. It means that high content of PFSI in cathode CL caused high performance of as-

prepared MEA. However this result is contrary to the result of Pt-PFSI interaction. It means that the effect of catalyst activation on MEA activation is smaller than other crucial factor, and it would be increased water content in Nafion and PFSI. The optimum PFSI content in cathode CL was 30 wt.%.

The interfacial features between CL and PEM was controlled by changing PFSI film thickness and hot-pressing. CV change of non hot-pressed MEAs after activation was similar to that of spray CCM MEAs in activation study. However CV shape of as-prepared hot-pressed MEAs was similar to that of activated MEAs. It means that the interaction between Pt(111) and sulfonate anion in PFSI became weaken after hot-pressing. The relationships between electrochemical properties (R_{PEM}, $R_{i,CCL}$, and C_{dl}) and experimental conditions (activation, hot-pressing, and PFSI film thickness) were evaluated and summarized in Table 4. Interface stability that is related to the interface between PEM and PFSI film was improved by hot-pressing, and it reduced R_{PEM} value. Interface area that is related to the interface between PFSI film and CL was enhanced by increase of PFSI film thickness, and it reduced $R_{i,CCL}$. Activation ratios of hot-pressed MEAs were lower than those of non hot-pressed MEAs because as-prepared hot-pressed MEAs showed relatively high performance due to improved interface stability. However activation values were increased with increase of PFSI film thickness because performance of activated MEAs that had bad interface stability and small interface area was too low.

In $R_{i,CCL}$ value of modified TLM in this thesis include one of the interface feature between CL and PEM, and therefore it is hard say that $R_{i,CCL}$ is ionic resistance of CL. Interface resistance of MEA that was prepared by CCM would be $31 - 51$ Ω cm^2 as shown in Fig. 3.8.

References

1. F. Barbir, "PEM Fuel Cells: Theory and Practice", *Elsevier Academic Press*, San Diego (2005).

2. R. O'Hayre, S-W. Cha, W. Colella, and F. B. Prinz, "Fuel Cell Fundamentals", *John Wiley & Sons*, New York (2006).

3. Fuel Cell Today, "History", http://www.fuelcelltoday.com/about-fuel-cells/history.

4. Wikipedia, "Fuel Cell", http://en.wikipedia.org/wiki/Fuel_cell#cite_note-2.

5. 2004 Smithsonian Institute, "Fuel Cell Origins", http://americanhistory.si.edu/fuelcells/origins/orig1.htm.

6. National Aeronautics and Space Administration, "Gemini: Bridge to the Moon", http://www.nasa.gov/externalflash/gemini_gallery.

7. DOE Hydrogen and Fuel Cells Program, "FY2011 Progress Report for the DOE Hydrogen and Fuel Cells Program", *U.S. Department of Energy*, Washington, D.C. (2011).

8. 2011 Gulf Oil International, "Alternative Fuel Cars in London, Hydrogen and Bio-Fuel Cars", http://www.gulfoilltd.com.

9. J. Zhang, "PEM Fuel Cell Electrocatalysts and Catalyst Layers, Fundamentals and Applications Part I", *Springer-Verlag*, London (2008).

10. J. Zhang, B. A. Litteer, W. Gu, H. Liu, and H. A. Gasteiger, "Effect of

Hydrogen and Oxygen Partial Pressure on Pt Precipitation within the Membrane of PEMFCs", *J. Electrochem. Soc.*, **154**, B1006 (2007).

11. N. Nonoyama, S. Okazaki, A. Z. Weber, Y. Ikogi, and T. Yoshida, "Analysis of Oxygen-Transport Diffusion Resistance in Proton-Exchange-Membrane Fuel Cells", *J. Electrochem. Soc.*, **158**, B416 (2011).

12. A. Ohma, S. Suga, S. Yamamoto, and K. Shinohara, "Membrane Degradation Behavior during Open-Circuit Voltage Hold Test", *J. Electrochem. Soc.*, **154**, B757 (2007).

13. J. H. Kim, E. A. Cho, J. H. Jang, H. J. Kim, T. H. Lim, I. H. Oh, J. J. Ko, and S. C. Oh, "Effects of Cathode Inlet Relative Humidity on PEMFC Durability during Startup–Shutdown Cycling I. Electrochemical Study", *J. Electrochem. Soc.*, **157**, B104 (2010).

14. R. Borup, J. Meyers, B. Pivovar, Y. S. Kim, R. Mukundan, N. Garland, D. Myers, M. Wilson, F. Garzon, D. Wood, P. Zelenay, K. More, K. Stroh, T. Zawodzinski, J. Boncella, J. E. McGrath, M. Inaba, K. Miyatake, M. Hori, K. Ota, Z. Ogumi, S. Miyata, A. Nishikata, Z. Siroma, Y. Uchimoto, K. Yasuda, K. Kimijima, and N. Iwashita, "Scientific Aspects of Polymer Electrolyte Fuel Cell Durability and Degradation", *Chem. Rev.*, **107**, 3904 (2007).

15. G. Wu, K. L. More, C. M. Johnston, and P. Zelenay, "High-Performance Electrocatalysts for Oxygen Reduction Derived from Polyaniline, Iron, and

Cobalt", *Science*, **332**, 443 (2011).

16. R. Subbaraman, D. Strmcnik, A. P. Paulikas, V. R. Stamenkovic, and N. M. Markovic, "Oxygen Reduction Reaction at Three-Phase Interfaces", *ChemPhysChem*, **11**, 2825 (2010).

17. L. M. Onishi, J. M. Prausnitz, and J. Newman, "Water-Nafion Equilibria. Absence of Schroeder's Paradox", *J. Phys. Chem. B*, **111**, 10166 (2007).

18. A. Z. Weber and J. Newman, "Effects of Membrane- and Catalyst-Layer-Thickness Nonuniformities in Polymer-Electrolyte Fuel Cells", *J. Electrochem. Soc.*, **154**, B405 (2007).

19. W. Liu and D. Zuckerbrod, "*In Situ* Detection of Hydrogen Peroxide in PEM Fuel Cells", *J. Electrochem. Soc.*, **152**, A1165 (2005).

20. M. K. Debe, A. K. Schmoeckel, G. D. Vernstrom, and R. Atanasoski, "High voltage stability of nanostructured thin film catalysts for PEM fuel cells", *J. Power Sources*, **161**, 1002 (2006).

21. L. Gancs, T. Kobayashi, M. K. Debe, R. Atanasoski, and A. Wieckowski, "Crystallographic Characteristics of Nanostructured Thin-Film Fuel Cell Electrocatalysts: A HRTEM Study", *Chem. Mater.*, **20**, 2444 (2008).

22. Y.-G. Yoon, G.-G. Park, T.-H. Yang, J.-N. Han, W.-Y. Lee, and C.-S. Kim, "Effect of pore structure of catalyst layer in a PEMFC on its performance", *Int. J. Hydrogen Energy*, **28**, 657 (2003).

23. Y.-H. Cho, H.-S. Park, Y.-H. Cho, D.-S. Jung, H.-Y. Park, and Y.-E. Sung, "Effect of platinum amount in carbon supported platinum catalyst on performance of polymer electrolyte membrane fuel cell", *J. Power Sources*, **172**, 89 (2007).

24. H.-S. Park, Y.-H. Cho, Y.-H. Cho, C. R. Jung, J. H. Jang, and Y.-E. Sung, "Performance enhancement of PEMFC through temperature control in catalyst layer fabrication", *Electrochim. Acta*, **53**, 763 (2007).

25. G. Bender, T. A. Zawodzinski, and A. P. Saab, "Fabrication of high precision PEFC membrane electrode assemblies", *J. Power Sources*, **124**, 114 (2003).

26. X. Wang, H. Zhang, J. Zhang, H. Xu, X. Zhu, J. Chen, and B. Yi, "A bi-functional micro-porous layer with composite carbon black for PEM fuel cells", *J. Power Sources*, **162**, 474 (2006).

27. P. G. Stampino, C. Cristiani, G. Dotelli, L. Omati, L. Zampori, R. Pelosato, and M. Guilizzoni, "Effect of different substrates, inks composition and rheology on coating deposition of microporous layer (MPL) for PEM-FCs", *Catal. Today*, **147S**, S30 (2009).

28. R. Benitez, J. Soler, and L. Daza, "Novel method for preparation of PEMFC electrodes by the electrospray technique", *J. Power Sources*, **151**, 108 (2005).

29. J. W. Ihm, H. Ryu, J. S. Bae, W. K. Choo, and D. K. Choi, "High performance of electrode with low Pt loading prepared by simplified direct screen printing

process in PEM fuel cells", *J. Mater. Sci.*, **39**, 4647 (2004).

30. A. Smirnova, X. Dong, H. Hara, A. Vasiliev, and N. Sammes, "Novel carbon aerogel-supported catalysts for PEM fuel cell application", *Int. J. Hydrogen Energy*, **30**, 149 (2005).

31. A. D. Taylor, E. Y. Kim, V. P. Humes, J. Kizuka, and L. T. Thompson, "Inkjet printing of carbon supported platinum 3-D catalyst layers for use in fuel cells", *J. Power Sources*, **171**, 101 (2007).

32. J. H. Cho, J. M. Kim, J. Prabhuram, S. Y. Hwang, D. J. Ahn, H. Y. Ha, and S.-K. Kim, "Fabrication and evaluation of membrane electrode assemblies by low-temperature decal methods for direct methanol fuel cells", *J. Power Sources*, **187**, 378 (2009).

33. M. S. Wilson and S. Gottesfeld, "Thin-film catalyst layers for polymer electrolyte fuel cell electrodes", *J. Appl. Electrochem.*, **22**, 1 (1992).

34. M. S. Wilson and S. Gottesfeld, "High Performance Catalyzed Membranes of Ultra-low Pt Loadings for Polymer Electrolyte Fuel Cells", *J. Electrochem. Soc.*, **139**, L28 (1992).

35. M. S. Wilson, J. A. Valerio, and S. Gottesfeld, "Low Platinum Loading Electrodes for Polymer Electrolyte Fuel Cells Fabricated Using Thermoplastic Ionomers", *Electrochim. Acta*, **40**, 355 (1995).

36. H. Tang, S. Wang, M. Pan, S. P. Jiang, and Ruan, "Performance of direct

methanol fuel cells prepared by hot-pressed MEA and catalyst-coated membrane (CCM)", *Electrochim. Acta*, **52**, 3714 (2007).

37. X. Ren, M. S. Wilson, and S. Gottesfeld, "High Performance Direct Methanol Polymer Electrolyte Fuel Cells", *J. Electrochem. Soc.*, **143**, L12 (1996).

38. J. Xie, K. L. More, T. A. Zawodzinski, and W. H. Smith, "Porosity of MEAs made by "Thin Film Decal" Method and Its Effect on Performance of PEFCs", *J. Electrochem. Soc.*, **151**, A1841 (2004).

39. H.-S. Park, Y.-H. Cho, Y.-H. Cho, I.-S. Park, N. Jung, M. Ahn, and Y.-E. Sung, "Modified Decal Method and Its Related Study of Microporous Layer in PEM Fuel Cells", *J. Electrochem. Soc.*, **155**, B455 (2008).

40. M. Lee, M. Uchida, H. Yano, D. A. Tryk, H. Uchida, and M. Watanabe, "New evaluation method for the effectiveness of platinum/carbon electrocatalysts under operating conditions", *Electrochim. Acta*, **55**, 8504 (2010).

41. X.-Z. Yuan, C. Song, H. Wang, and J. Zhang, "Electrochemical Impedance Spectroscopy in PEM Fuel Cells, Fundamentals and Applications", *Springer-Verlag*, London, 2010.

42. S. Ochi, O. Kamishima, J. Mizusaki, and J. Kawamura, "Investigation of proton diffusion in Nafion®117 membrane by electrical conductivity and NMR", *Solid State Ionics*, **180**, 580 (2009).

43. J. Greeley, I. E. L. Stephens, A. S. Bondarenko, T. P. Johansson, H. A. Hansen,

T. F. Jaramillo, J. Rossmeisl, I. Chorkendorff, and J. K. Norskov, "Alloys of platinum and early transition metals as oxygen reduction electrocatalysts", *Nature Chem.*, **1**, 552 (2009).

44. G. Lin and T. V. Nguyen, "Effect of Thickness and Hydrophobic Polymer Content of the Gas Diffusion Layer on Electrode Flooding Level in a PEMFC", *J. Electrochem. Soc.*, **152**, A1942 (2005).

45. Y.-H. Cho, J. W. Bae, Y.-H. Cho, J. W. Lim, M. Ahn, W.-S. Yoon, N.-H. Kwon, J. Y. Jho, and Y.-E. Sung, "Performance enhancement of membrane electrode assemblies with plasma etched polymer electrolyte membrane in PEM fuel cell", *Int. J. Hydrogen Energy*, **35**, 10452 (2010).

46. Y.-H. Cho, J. Kim, S. J. Yoo, T.-Y. Jeon, M. Ahn, N. Jung, Y.-H. Cho, J. W. Lim, J. K. Lee, W.-S. Yoon, and Y.-E. Sung, "Enhancement of polymer electrolyte membrane fuel cell performance by boiling a membrane electrode assembly in sulfuric acid solution", *J. Power Sources*, **195**, 5952 (2010).

47. C. Boyer, S. Gamburzev, O. Velev, S. Srinivasan, and A. J. Appleby, "Measurements of proton conductivity in the active layer of PEM fuel cell gas diffusion electrodes", *Electrochim. Acta*, **43**, 3703 (1998).

48. M. C. Lefebvre, R. B. Martin, and P. G. Pickup, "Characterization of Ionic Conductivity Profiles within Proton Exchange Membrane Fuel Cell Gas Diffusion Electrodes by Impedance Spectroscopy", *Electrochem. Solid-State*

Lett., **2**, 259 (1999).

49. R. de Levie, "Advances in Electrochemistry and Electrochemical Engineering", **6**, *John Wiley & Sons*, New York (1967).

50. J. Gazzarri, M. Eikerling, Q. Wang, and Z.-S. Liu, "Estimation of Local Relative Humidity in Cathode Catalyst Layers of PEFC", *Electrochem. Solid-State Lett.*, **13**, B58 (2010).

51. J. H. Jang, S. Jeon, J. H. Cho, S.-K. Kim, S.-Y. Lee, E.A. Cho, H.-J. Kim, J. Han, and T.-H. Lim, "Complex Capacitance Analysis of Ionic Resistance and Interfacial Capacitance in PEMFC and DMFC Catalyst Layers", *J. Electrochem. Soc.*, **156**, B1293 (2009).

52. H. Nara, S. Tominaka, T. Momma, and T. Osaka, "Impedance Analysis Counting Reaction Distribution on Degradation of Cathode Catalyst Layer in PEFCs", *J. Electrochem. Soc.*, **158**, B1184 (2011).

53. Y. Liu, M. W. Murphy, D. R. Baker, W. Gu, C. Ji, J. Jorne, and H. A. Gasteiger, "Proton Conduction and Oxygen Reduction Kinetics in PEM Fuel Cell Cathodes: Effects of Ionomer-to-Carbon Ratio and Relative Humidity", *J. Electrochem. Soc.*, **156**, B970 (2009).

54. S.-J. Lee and S.-I. Pyun, "Effect of annealing temperature on mixed proton transport and charge transfer-controlled oxygen reduction in gas diffusion electrode", *Electrochim. Acta*, **52**, 6525 (2007).

55. M. Eikerling and A. A. Kornyshev, "Modelling the performance of the cathode catalyst layer of polymer electrolyte fuel cells", *J. Electroanal. Chem.*, **453**, 89 (1998).

56. Y. G. Chirkov and V. I. Rostokin, "Calculation of Optimum Thickness of Active Layer of Oxygen and Air Cathodes of Fuel Cell with Nafion and Platinum", *Russ. J. Electrochem.*, **45**, 183 (2009).

57. M. Lee, M. Uchida, D. A. Tryk, H. Uchida, and M. Watanabe, "The effectiveness of platinum/carbon electrocatalysts: Dependence on catalyst layer thickness and Pt alloy catalytic effects", *Electrochim. Acta*, **56**, 4783 (2011).

58. Z. Qi and A. Kaufman, "Activation of low temperature PEM fuel cells", *J. Power Sources*, **111**, 181 (2002).

59. X.-Z. Yuan, S. Zhang, J. C. Sun, and H. Wang, "A review of accelerated conditioning for a polymer electrolyte membrane fuel cell", *J. Power Sources*, **196**, 9097 (2011).

60. B.-K. Kho, I.-H. Oh, S.-A. Hong, and H. Y. Ha, "The effect of pretreatment methods on the performance of passive DMFCs", *Electrochim. Acta*, **50**, 781 (2004).

61. Z. Xu, Z. Qi, C. He, and A. Kaufman, "Combined activation methods for proton-exchange membrane fuel cells", *J. Power Sources*, **156**, 315 (2006).

62. A. Lindermeir, G. Rosenthal, U. Kunz, and U. Hoffmann, "On the question of

MEA preparation for DMFCs", *J. Power Sources*, **129**, 180 (2004).

63. J. R. Macdonald, "Impedance Spectroscopy Emphasizing Solid Materials and Systems", *John Wiley & Sons*, New York (1987).

64. DuPont Fuel Cells, "DuPont^{TM} Nafion$^{®}$ PFSA membranes", http://www2. dupont.com/FuelCells/en_US/assets/downloads/dfc201.pdf.

65. SGL Technologies GmBH, Fuel Cell Components, "GDL 34 & 35 Series Gas Diffusion Layer", http://www.sglgroup.com/cms/international/products/ product-groups/su/fuel-cell-components/ (2009).

66. A. Kuver, I. Vogel, and W. Vielstich, "Distinct performance evaluation of a direct methanol SPE fuel cell. A new method using a dynamic hydrogen reference electrode", *J. Power Sources*, **52**, 77 (1994).

67. T. E. Springer, T. A. Zawodzinski, M. S. Wilson, and S. Gottesfeld, "Characterization of Polymer Electrolyte Fuel Cells Using AC Impedance Spectroscopy", *J. Electrochem. Soc.*, **143**, 587 (1996).

68. J. Zhao and A. Manthiram, "In Situ Electrochemical Characterization of Proton Exchange Membrane Fuel Cells Fabricated with Pd–Pt–Ni Cathode Catalysts", *J. Electrochem. Soc.*, **158**, B208 (2011).

69. K. Kinoshita and J. A. S. Bett, "Potentiodynamic Analysis of Surface Oxides on Carbon Blacks", *Carbon*, **11**, 403 (1973).

70. K. H. Kangasniemi, D. A. Condit, and T. D. Jarvi, "Characterization of Vulcan

Electrochemically Oxidized under Simulated PEM Fuel Cell Conditions", *J. Electrochem. Soc.*, **151**, E125 (2004).

71. J.-S. Ye, X. Liu, H. F. Cui, W.-D. Zhang, F.-S. Sheu, and T. M. Lim, "Electrochemical oxidation of multi-walled carbon nanotubes and its application to electrochemical double layer capacitors", *Electrochem. Commun.*, **7**, 249 (2005).

72. J. Wang, G. Yin, Y. Shao, S. Zhang, Z. and Wang, Y. Gao, "Effect of carbon black support corrosion on the durability of Pt/C catalyst", *J. Power Sources*, **171**, 331 (2007).

73. S. B. Brummer, "The Use of Large Anodic Galvanostatic Transients to Evaluate the Maximum Adsorption on Platinum from Formic Acid Solutions", *J. Phys. Chem.*, **69**, 562 (1965).

74. W. Li, W. Zhou, H. Li, Z. Zhou, B. Zhou, G. Sun, and Q. Xin, "Nano-stuctured Pt–Fe/C as cathode catalyst in direct methanol fuel cell", *Electrochim. Acta*, **49**, 1045 (2004).

75. M. Okamoto, T. Fujigaya, and N. Nakashima, "Design of an Assembly of Poly(benzimidazole), Carbon Nanotubes, and Pt Nanoparticles for a Fuel-Cell Electrocatalyst with an Ideal Interfacial Nanostructure", *Small*, **5**, 735 (2009).

76. G. Tamizhmani, J. P. Dodelet, and D. Guay, "Crystallite Size Effects of Carbon-Supported Platinum on Oxygen Reduction in Liquid Acids", *J. Electrochem.*

Soc., **143**, 18 (1996).

77. J. H. Jang and S. M. Oh, "Complex Capacitance Analysis of Porous Carbon Electrodes for Electric Double-Layer Capacitors", *J. Electrochem. Soc.*, **151**, A571 (2004).

78. A. Parthasarathy, B. Dave, S. Srinivasan, and A. J. Appleby, "The Platinum Microelectrode/Nafion Interface: An Electrochemical Impedance Spectroscopic Analysis of Oxygen Reduction Kinetics and Nation Characteristics", *J. Electrochem. Soc.*, **139**, 1634 (1992).

79. T. E. Springer, T. A. Zawodzinski, and S. Gottesfeld, "Polymer Electrolyte Fuel Cell Model", *J. Electrochem. Soc.*, **138**, 2334 (1991).

80. M. Boaventura and A. Mendes, "Activation procedures characterization of MEA based on phosphoric acid doped PBI membranes", *Int. J. Hydrogen Energy*, **35**, 11649 (2010).

81. V. B. Silva and A. Rouboa, "Hydrogen-fed PEMFC: Overvoltage analysis during an activation procedure", *J. Electroanal. Chem.*, **671**, 58 (2012).

82. X.-Z. Yuan, J. C. Sun, H. Wang, and H. Li, "Accelerated conditioning for a proton exchange membrane fuel cell", *J. Power Sources*, **205**, 340 (2012).

83. V. B. Silva and A. Rouboa, "An activation procedure applied to fluorinated and non-fluorinated proton exchange membranes", *Fuel Process. Technol.*, **in-press**.

84. Z. Qi and A. Kaufman, "Quick and effective activation of proton-exchange membrane fuel cells", *J. Power Sources*, **114**, 21 (2003).

85. K. Kinoshita, "Particle Size Effects for Oxygen Reduction on Highly Dispersed Platinum in Acid Electrolytes", *J. Electrochem. Soc.*, **137**, 845 (1990).

86. K. J. J. Mayrhofer, D. Strmcnik, B. B. Blizanac, V. Stamenkovic, M. Arenz, and N. M. Markovic, "Measurement of oxygen reduction activities via the rotating disc electrode method: From Pt model surfaces to carbon-supported high surface area catalysts", *Electrochim. Acta*, **53**, 3181 (2008).

87. D. Aberdam, R. Durand, R. Faure, and F. El-Omar, "Structural Changes of a Pt(111) Electrode Induced by Electrosorption of Oxygen in Acidic Solutions: A Coupled Voltammetry, LEED and AES Study", *Surf. Sci.*, **171**, 303 (1986).

88. R. Gomez and J. Clavilier, "Electrochemical behaviour of platinum surfaces containing (110) sites and the problem of the third oxidation peak", *J. Electroanal. Chem.*, **354**, 189 (1993).

89. N. Markovic, H. Gasteiger, and P. N. Ross, "Kinetics of Oxygen Reduction on Pt(hkl) Electrodes: Implications for the Crystallite Size Effect with Supported Pt Electrocatalysts", *J. Electrochem. Soc.*, **144**, 1592 (1997).

90. S. Motoo and N. Furuya, "Electrochemistry of Platinum Single Crystal Surfaces Part I. Structural Change of the Pt(111) Surface Followed by an

Electrochemical Method", *J. Electroanal. Chem.*, **172**, 339 (1984).

91.   N. Furuya and S. Koide, "Hydrogen Adsorption on Platinum Single-Crystal Surfaces", *Surf. Sci.*, **220**, 18 (1989).

92.   A. M. Funtikov, U. Stimming, and R. Vogel, "Anion adsorption from sulfuric acid solutions on Pt(111) single crystal electrodes", *J. Electroanal. Chem.*, **428**, 147 (1997).

93.   T. A. Zawodzinski, M. Neeman, L. O. Sillerud, and S. Gottesfeld, "Determination of Water Diffusion Coefficients in Perfluorosulfonate Ionomeric Membranes", *J. Phys. Chem.*, **95**, 6040 (1991).

94.   D. R. Morris and X. Sun, "Water-Sorption and Transport Properties of Nafion 117H", *J. Appl. Polym. Sci.*, **50**, 1445 (1993).

95.   T. A. Zawodzinski, J. Davey, J. Valerio, and S. Gottesfeld, "The Water Content Dependence of Electro-Osmotic Drag in Proton-Conducting Polymer Electrolytes", *Electrochim. Acta*, **40**, 297 (1995).

96.   A. Z. Weber and J. Newman, "Transport in Polymer-Electrolyte Membranes I. Physical Model", *J. Electrochem. Soc.*, **150**, A1008 (2003).

97.   A. Z. Weber and J. Newman, "Transport in Polymer-Electrolyte Membranes II. Mathematical Model", *J. Electrochem. Soc.*, **151**, A311 (2004).

98.   K.-H. Kim, K.-Y. Lee, H.-J. Kim, E. A. Cho, S.-Y. Lee, T.-H. Lim, S. P. Yoon, I. C. Hwang, and J. H. Jang, "The effects of Nafion[®] ionomer content in PEMFC

MEAs prepared by a catalyst-coated membrane (CCM) spraying method", *Int. J. Hydrogen Energy*, **35**, 2119 (2010).

99. P. Gode, F. Jaouen, G. Lindbergh, A. Lundblad, and G. Sundholm, "Influence of the composition on the structure and electrochemical characteristics of the PEFC cathode", *Electrochim. Acta*, **48**, 4175 (2003).

100. I. Esparbe, E. Brillas, F. Centellas, J. A. Garrido, R. M. Rodriguez, C. Arias, and P.-L. Cabot, "Structure and electrocatalytic performance of carbon-supported platinum nanoparticles", *J. Power Sources*, **190**, 201 (2009).

101. Z. Qi and A. Kaufman, "Low Pt loading high performance cathodes for PEM fuel cells", *J. Power Sources*, **113**, 37 (2003).

102. S. Mu and M. Tian, "Optimization of perfluorosulfonic acid ionomer loadings in catalyst layers of proton exchange membrane fuel cells", *Electrochim. Acta*, **60**, 437 (2012).

103. Y. W. Rho, O. A. Velev, S. Srinivasan, and Y. T. Kho, "Mass Transport Phenomena in Proton Exchange Membrane Fuel Cells Using O_2/He, O_2/Ar, and O_2/N_2 Mixtures I. Experimental Analysis", *J. Electrochem. Soc.*, **141**, 2084 (1994).

104. Y. W. Rho, S. Srinivasan, and Y. T. Kho, "Mass Transport Phenomena in Proton Exchange Membrane Fuel Cells Using O_2/He, O_2/Ar, and O_2/N_2 Mixtures II. Theoretical Analysis", *J. Electrochem. Soc.*, **141**, 2089 (1994).

105. M. Cappadonia, J. W. Erning, S. M. S. Niaki, and U. Stimming, "Conductance of Nafion 117 membranes as a function of temperature and water content", *Solid State Ionics*, **77**, 65 (1995).

106. T. D. Gierke, G. E. Munn, and F. C. Wilson, "The Morphology in Nafion* Perfluorinated Membrane Products, as Determined by Wide- and Small- Angle X-Ray Studies", *J. Polym. Sci., Polym. Phys.*, **19**, 1687 (1981).

107. K. A. Mauritz and R. B. Moore, "State of Understanding of Nafion", *Chem. Rev.*, **104**, 4535 (2004).

108. S. Y. Jeong and O. H. Han, "Influence of Hot Pressing on the Pore Structure of Nafion Electrolyte Membrane Investigated by ^{1}H NMR", *Bull. Korean Chem. Soc.*, **30**, 1559 (2009).

국문초록

본 연구에서는 고분자 전해질막 연료전지의 단위전지 상태에서 막전극 접합체의 전기화학적 분석을 수행하였다. 고분자 전해질막 연료전지 내의 공기극 촉매층과 고분자 전해질막의 전기화학적 특성을 분석하기 위해, 전기화학 임피던스 분석 모델로 사용되는 송전선 모델을 수정하여 이용하였다. 공기극 촉매층 내에 전하전달이 거의 없는 환경을 조성하여 임피던스 측정을 수행하였고, 개선된 송전선 모델을 적용하여 결과를 피팅하였다. 피팅한 결과를 통해 공기극 촉매층의 이온저항과 전기 이중층의 전기용량, 그리고 고분자 전해질막의 이온저항을 추정할 수 있었다. 그리고 이를 이용하여 세 가지 주제의 연구를 수행하였다. (1) 공기극 촉매층의 두께와 백금 담지량 및 담지 밀도에 따른 특성 변화를 분석하였고, (2) CCM 방식으로 제조한 막전극 접합체의 활성화과정 전후의 전기화학적 물성 차이를 측정, 분석하였으며, (3) CCS 방식으로 다양한 계면 특성을 가지는 막전극 접합체를 제조하고 활성화과정 이후의 변화를 측정함으로써, 계면 특성과 활성화과정에 따른 전기화학적 물성 변화를 분석하였다. (1) 공기극 촉매층의 두께에 대한 연구에 있어서 탄소에 담지된 백금 촉매를 사용할 경우, 촉매 사용량이 0.2 mg_{Pt} cm^{-2} 이하로 적을 때는 탄소에 대한 백금의 담지 비율이 낮고 활성표면적이 큰 촉매를 사용할 때 우수한 성능을 나타내었다. 하지만 촉매 사용량이 많은

경우 탄소에 대한 백금의 담지 비율이 크고 두께가 얇은 촉매층을 사용할 경우 우수한 성능을 나타내었다. 이는 촉매층 두께 증가에 따른 이온저항 증가와 물질이동에 대한 영향이 증가하기 때문이다. 또한 구동 중 측정한 임피던스 분석으로 계산된 전기이중층의 전기용량과 함께 비교함으로써, 유효한 촉매층의 두께를 추정하였다. (2) 그리고 활성화 과정에 대한 연구에 있어서, 공기극 촉매층 내의 이오노머 함량을 다르게 하여 실험하였고, 이를 통해 활성화 과정 이후 촉매층의 전기화학적 특성 변화와 이오노머 함량의 관계에 대해 분석하였다. CCM 방식으로 제조한 막전극 접합체의 경우, 활성화과정 이전에는 백금 촉매의 Pt(111) 결정면과 촉매층 내의 이오노머 사이에 상호작용이 강하게 나타났다. 활성화과정 이후 상호작용이 약해지며, 이에 따라 산소환원반응 활성이 향상되는 것을 추정할 수 있었다. 그리고 활성화과정 이후 막전극 접합체 내의 수화도가 향상됨에 따라 고분자 전해질막과 이오노머의 이온저항이 감소하는 것을 알 수 있었다. 이를 통해 활성화과정에 있어서 막전극 접합체의 수화에 의한 영향이 크다는 것을 알 수 있었다. (3) CCS 방식을 이용하여 계면 특성이 다른 막전극 접합체를 제조하여 분석하였다. 고온압착공정을 수행한 경우, 활성화과정 이전에도 백금과 이오노머 사이의 상호작용이 강하지 않았으며, 활성화과정 이전의 성능 또한 상대적으로 크게 나타났다. 고온압착공정 수행을 통해 계면 안정성을 향상시킬 수 있었고, 촉매층 위에 코팅한 이오노머 필름의 양을 늘림에

따라 계면의 면적이 늘어났다. 고온압착공정을 통한 계면 안정성 향상은

임피던스 분석 결과 중 고분자 전해질막 이온저항의 감소로 나타났고,

촉매층 위에 코팅한 이오노머 필름의 양 증가에 따른 계면 면적 증가는

임피던스 분석 결과 중 촉매층 이온저항의 감소로 나타났다.

주요어: 고분자 전해질막 연료전지, 막전극 접합체, 임피던스, 공기극 촉매층,

이오노머

학   번: 2008-30895